Immersed Finite Element Particle-In-Cell Modeling of Surface Charging in Rarefied Plasmas

Pu Wang

Dissertation submitted to the faculty of the
Virginia Polytechnic Institute and State University
in partial fulfillment of the requirements for the degree of

Doctor of Philosophy
In
Aerospace Engineering

Joseph Wang, Chair
Christopher Roy, Co-Chair
Tao Lin
Wayne A. Scales

January 25, 2010
Blacksburg, Virginia

Keywords: Immersed Finite Element, Particle-In-Cell, Charging

Immersed Finite Element Particle-In-Cell Modeling of Surface Charging in Rarefied Plasmas

Pu Wang

(ABSTRACT)

Surface charging is a fundamental interaction process in space plasma engineering. A three-dimensional Immersed Finite Element Particle-In-Cell (IFE-PIC) method is developed to model surface charging involving complex boundary conditions. This method extends the previous IFE-PIC algorithm to explicitly include charge deposition on a dielectric surface for charging calculations. Three simulation studies are carried out using the new algorithm to model current collection and charging in both the orbital motion limited (OML) and space charge limited regime. The first one is a full particle simulation of the charging process of single small sphere and clusters of multiple small spheres in plasma. We find that while single sphere charging agrees well with the predictions of the OML theory, the charging of a sphere in a cluster is significantly, indicating that the often used OML charging model is not an accurate one to model charging in dusty plasma. The second one concerns a secondary electron emission experiment. The simulation includes detailed experimental setup in a vacuum chamber and the results are compared against experimental data. The simulation is used to determine the facility error in experiments. The third one is a full particle simulation of charging on lunar surface. The simulation concerns both flat and non-flat surface, and spacecraft on lunar surface, in the lunar polar region. The surface sees a mesothermal solar wind plasma flow and the emission of photoelectrons and secondary electrons. At a small sun elevation angle, the surface landscape generates a complex plasma flow field and local differential charging on surface. The results will be useful for further study of charging and levitation of lunar dust.

Acknowledgements

First, I would like to thank my advisor Dr. Joseph Wang, for your inspiring guidance in the past four years. Without your support and direction, I could not finish this dissertation. I benefit a lot from your comprehensive knowledge about plasma physics. I would like to thank Dr. Tao Lin for your guidance in mathematics part in my dissertation. Your patient, knowledge and experience provide me a great opportunity to learn. I would like to thank Dr. Wayne A. Scales for your advices in my research and your effort to provide me computing system. I have learned a lot from Dr. Christopher Roy, I am thankful for your effort, support and advices on my dissertation.

I would like to acknowledge Xiaoming He and my colleagues of Dr. Wang's research group: Hyunju Jeong, Ouliang Chang and Ning Ding. It is a great memory to study together with you.

I would like to express special thanks to my parents, grandparents and family. I am grateful to your love and patience. Without your supporting, inspiration, I could not finish this dissertation. I would like to thank Jing Sun. You gave me so much support and I can always get energy from you when I was depressed. I will never forget the happy days with you.

I would like to thank my friends in Tsinghua University and Virginia Tech. Your enthusiasm, spirit gave me energy to pursue my dream.

Contents

List of Figures

List of Tables

Chapter 1

Introduction

1.1 Introduction

This chapter will introduce the content and structure of this dissertation. The background of plasma and complex object surface interactions is given, including the concept of charging, current collection. Surface charging, the major research topic, is addressed in detail. Previous work on object-plasma interaction simulation is reviewed. This chapter also outlines the work presented in this dissertation.

1.2 Background

1.2.1 Charging Problem in Plasma

Plasma is a partially ionized quasi-neutral gas which exhibits collective behaviors. One of the classical topics in the study of plasma is the surface interactions between an object and its surrounding plasma. This dissertation concerns plasma-surface interactions for space applications. For an object immersed in space plasma, one of the fundamental surface interactions is surface charging.

An object immersed in plasma will collect ions and electrons until it reaches the floating potential. The incident electron and ion can also produce secondary electrons. Some absorbed electrons may collide with the atoms in the material and reverse their direction and thus become backscattered electrons. The secondary electron current is a function of the incident particle current and energy, and material. Photoelectrons are emitted if the surface is exposed to the solar flux and a function of the current is the

material, solar flux, solar incident angle and surface potential [2].

The current collection/emission on surface affects the charge accumulation and thus the surface potential. The surface potential in turn affects the electric field surrounding the object which then affects the dynamics of charged particles surrounding the object. Hence, all plasma-surface interactions in space are directly or indirectly related to surface charging.

In a charging process, the potential of surface changes with the charge accumulation. At steady state, the net current on a surface is zero. For conductive object in space plasma, the potential Φ of object is determined by

$$\frac{dQ}{dt} = C\frac{d\Phi}{dt} = I_{from\ surface} - I_{to\ surface} = I_{net}, \tag{1.1}$$

where Q is the charge on object, C is the capacitance and I_{net} is the net current to the surface, the floating potential is determined by I_{net}=0. For dielectric object, the surface potential at each point is determined by local current balance. For a surface element on the charging object, the rate at which the charge on the surface changes as a function of time is given by [2]:

$$\frac{d\sigma}{dt}A = I_{from\ surface} - I_{to\ surface} = I_{net}, \tag{1.2}$$

here σ is the surface charge density and A is the surface element area. If all the current sources are known as a function of the surface potential, then the surface floating potential can be obtained from the following current balance equation

$$\begin{aligned} &I_e(\Phi_s) - [I_i(\Phi_s) + I_{se}(\Phi_s) + I_{si}(\Phi_s) + I_{be}(\Phi_s) + I_{ph}(\Phi_s)] \\ &= I_{net} = I_{from\ surface} - I_{to\ surface} = 0 \end{aligned}, \tag{1.3}$$

where

Φ_s is the surface potential,
I_e is the incident electron current,
I_i is the incident ion current,
I_{se} is the secondary electron current due to I_e,
I_{si} is the secondary electron current due to I_i,
I_{be} is the backscattered electrons due to I_e,
I_{ph} is the photoelectron current.

The charging interaction can occur at different dimension scales ranging from dust to the spacecraft, to planetary surface. The current collection by object may have different characteristics depending on the relative scale of the sheath thickness

compared to the object dimension. If the sheath thickness is much smaller than the object dimension, the sheath is called a "thin sheath". Current collection under the "thin sheath" condition is said to be "space charge limited" and it is limited by the electric field within the sheath. Here, the sheath thickness determines the region over which charge is collected and is important in determining the maximum current that can flow to the surface. On the other hand, if the sheath thickness is much larger than the object dimension, the sheath is "thick sheath". Current collection under the "thick sheath" condition is "orbital motion limited" (OML). The density of the plasma is sufficiently low that whether the attracted particles are collected by the surface is determined by the orbital parameters (energy, angular momentum) of each particle in the far field. A simple measure of the sheath thickness is the Debye length. For most charging problems in space plasma, the plasma surrounding are considered collisionless because the mean free path is typically larger than spacecraft dimension $\lambda_{mfp} >> L$. The transport of charged particles in collisionless plasma requires kinetic treatment of charged particle transport. This dissertation considers charging of an object in a collisionless plasma under thin sheath and thick sheath conditions.

1.2.2 Plasma Governing Equations

The electromagnetic fields are described by the Maxwell's equations

$$\nabla \bullet \mathbf{B} = 0, \tag{1.4}$$

$$\nabla \times \mathbf{B} = \mu_0 \mathbf{j} + \frac{1}{c^2}\frac{\partial \mathbf{E}}{\partial t}, \tag{1.5}$$

$$\nabla \bullet \mathbf{E} = \frac{\rho}{\varepsilon_0}, \tag{1.6}$$

$$\nabla \times \mathbf{E} = \frac{\partial \mathbf{B}}{\partial t}, \tag{1.7}$$

where the speed of light in free space is $c = (\varepsilon_0 \mu_0)^{-1/2}$. If the time rate of change of both the **E** field and **B** field are negligible, the interaction is electrostatic and the Maxwell's equations are simplified to

$$\nabla \bullet \mathbf{B} = 0, \tag{1.8}$$

$$\nabla \times \mathbf{B} = 0, \tag{1.9}$$

$$\nabla \bullet \mathbf{E} = \frac{\rho}{\varepsilon_0}, \tag{1.10}$$

$$\nabla \times \mathbf{E} = 0. \tag{1.11}$$

Then the electrostatic potential Φ can be introduced as

$$\mathbf{E} = -\nabla \Phi. \tag{1.12}$$

The electrostatic field is described by the Poisson's equation

$$\nabla \bullet \mathbf{E} = -\nabla \bullet \nabla \Phi = -\nabla^2 \Phi = \frac{\rho}{\varepsilon_0}. \tag{1.13}$$

For a medium with permittivity ε, it can be written as

$$\nabla \bullet (\varepsilon \mathbf{E}) = -\nabla \bullet \varepsilon \nabla \Phi = \rho. \tag{1.14}$$

In the applications considered in this dissertation, the effects of magnetic field are neglected. For a collisionless plasma with only the electrostatic field, the particle transport can be determined from the Vlasov equation

$$\frac{\partial f}{\partial t} + \mathbf{v} \bullet \nabla f + \frac{q}{m} \mathbf{E} \bullet \frac{\partial f}{\partial \mathbf{v}} = 0. \tag{1.15}$$

It may be solved either directly for the distribution function or by following individual particle trajectories in electric field self-consistently. The force on a particle with charge q in the electrostatic field is given by

$$\mathbf{F} = q\mathbf{E}. \tag{1.16}$$

The motion of the particle in the **E** field is given by Newton's Law

$$m \frac{d\mathbf{v}}{dt} = \mathbf{F}, \tag{1.17}$$

$$\frac{d\mathbf{x}}{dt} = \mathbf{v}. \tag{1.18}$$

A standard algorithm to simulate collisionless plasma is the Particle-In-Cell (PIC) method [7], in which space charge, particle trajectories and electric fields are solved self-consistently. The method used in this dissertation is to combine the PIC algorithm with solve equation (1.14), (1.16), (1.17), (1.18), with charging calculations on surface.

1.3 Literature Review

1.3.1 Analytical Approach

Most analytic studies of the surface charging are based on the probe theory. The fundamental equation of this theory is the current balance equation. In such an approach, one tries to solve for plasma distribution under external electric field, integrate this distribution function to obtain the current collection on object surface as a function of surface potential, and then use the current balance equation to solve potential.

The analytical approach can only be applied for simple situations where the current collection by the object can be obtained without having to solve for the electric field and plasma transport iteratively. Hence, the current collections can be obtained by integrating the distribution function. Such an approach is not a self-consistently one. In order to find a self-consistent solution to plasma dynamics, current collection, charge deposition and surface potential, a numerical approach is needed for most problems.

1.3.2 Numerical Approach

The standard numerical method to simulate collisionless plasma is Particle-In-Cell (PIC) method [7], in which space charge, particle trajectories and electric fields are solved self-consistently. In PIC method, the plasma is modeled by macro-particles. The simulation domain is discretized into Cartesian mesh nodes and the simulation particle charges are deposited on the mesh nodes to get the space charge density. The potential and electric field are solved on the mesh nodes. By interpolating from the mesh nodes to the particle position, the force can be obtained which are then used to push particles [6]. Figure 1.1 shows the typical computational cycle in each time step.

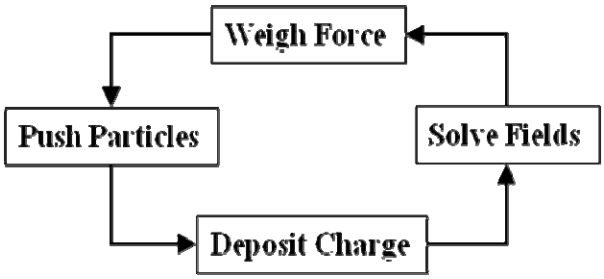

Figure 1.1 PIC computational cycle

The methods to solve the Poisson's equation in PIC simulations of plasma object interactions in general fall into the following categories, finite-difference with Cartesian mesh, finite volume with non-orthogonal grid, finite-element with body-fitting unstructured mesh, immersed boundary (finite difference), particle representation of object on Cartesian mesh, and immersed finite element.

Finite difference method combining with PIC model is used in early plasma-surface interaction simulations. A structured, Cartesian mesh is applied in the finite difference method based PIC model. The curvilinear object boundary is approximated as stair-case. Wang and Hastings [13, 14], Wang and Garrett [15] developed a particle simulation model to study mesothermal plasma flow around a large object. There are also some simulation software using this method such as the multi-utility spacecraft charging analysis tool (MUSCAT) [43, 44] in Japan developed in 2007.

Finite element method based PIC model is the widely used model in most current simulations. Unstructured mesh is used to body fit the object boundary. Using body fitting grid is an effective way to solve the equation with complex boundary and keep certain accurate. The solution of an interface problem has second order accurate approximation when using Galerkin finite element method with the standard linear basis functions if the triangulation is aligned with the interface like body fitting grid [22, 77, 78]. The resulting linear system of equation in finite element formulation is symmetric positive definite and it is also possible to produce second order accurate approximation to the solution of interface problem by applying the appropriate second order accurate finite difference schemes in a body fitting curvilinear grid [79]. Ambrosiano et al. [81, 82] applied finite element method on this unstructured body fitting grid of triangles to electromagnetic particle simulation. This unstructured grid provides enormous geometric flexibility in fitting the computational nodes to particular problems and makes adaptive refinement straightforward. Brandon et al. [83] developed 3D electromagnetic Particle-In-Cell simulation method for geometrically complex domains using non-orthogonal, unstructured mixed polyhedral

mesh. Maxwell's equations are solved using discrete surface integral method which preserved the electromagnetic field divergence constraints and is a direct generalization of the standard staggered grid finite difference method. There are also some software developed applying the finite element method in PIC model such as the Charging Analyzer Program of NASA (NASCAP) [31, 32, 33, 34, 35, 36], Spacecraft Plasma Interaction System (SPIS), Europe [37, 38, 39, 40].

Wang et al. [94] developed the parallel, non-orthogonal-grid, three-dimensional electromagnetic PIC code based on finite volume formulation. It used a logically Cartesian grid of deformable hexahedral cells, a discrete surface integral algorithm to calculate the electromagnetic field, and a hybrid logical-physical space algorithm to push particles. The particle pushing process is a hybrid logical-physical space operation that calculates particle velocity in physical space but performs particle position update and particle-grid interpolations in logical space. The accuracy of its hybrid particle push algorithm is second order in time and space, and is linearly proportional to the grid distortion. However, the non-orthogonal grid code involves significantly more calculations. This will slow down the speed of the calculation.

In real object-plasma interaction problems, there are some challenges require the simulation model is accurate and efficient. The object boundary conditions are complicated which may have complex geometry or material property. The wide dimension scale spectrum may cover from the large curvature and small curvature. These different dimension scales need to be combined in simulations. Some special cases including some charged objects coupling, the boundary conditions are complex and an efficient method is significant so solve this problem. In order to apply the particle simulation method as a research tool, the simulation model should be sophisticated enough so that complex geometric and boundary conditions as well as field effects can be modeled properly. It should also be computational efficient enough so that large-scale particle simulations can be performed routinely with reasonable time.

Current simulation models are most based on finite different or finite element formulation for the field problem and the mesh is generally structured Cartesian mesh or unstructured body fitting mesh. Accuracy and computational speed present conflicting requirements for large-scale PIC simulations involving complex object boundary.

Using body fitting grid is an effective way to solve the equation with complex boundary and keep certain accurate. The solution of an interface problem has second order accurate approximation when using Galerkin finite element method with the standard linear basis functions if the triangulation is aligned with the interface like body fitting grid [22, 77, 78]. The resulting linear system of equation in finite element formulation is symmetric positive definite and it is also possible to produce second order accurate approximation to the solution of interface problem by applying the

appropriate second order accurate finite difference schemes in a body fitting curvilinear grid. However, there are some disadvantages using this body fitting grid method. First, the body fitting grid for an interface problem is generated where the interface separates the solution domain into pieces or problems with complicated geometries. For still object, the mesh is generated at the beginning of the simulation and doesn't need to be generated again in following time loops. The time for generate mesh once is negligible in a large scale simulation. However, for boundaries involving large and small curvatures such as the dust locating on the curvature surface, the cost of body fitting mesh generation is not efficient. For the moving interface, the body fitting grid should be generated again with the motion of interface. It is a difficult and time consuming process. Second, for particle simulation models using body fitting grids, they usually put an annoying computational over-head to search for particles using cumbersome techniques [80]. Such complicated particle searching method slows down the simulation and limits the size of the problems that can be handled. In the PIC code, the particles are located in the whole simulation domain but the field quantities are defined only on the discrete mesh nodes. It is needed to interpolate field from mesh nodes to particle positions to push particle and deposit charge quantities from particle positions to the mesh nodes to solve electric field. A PIC code spends a significant portion of computational cost on these interpolation and deposition steps of the charge quantities and electric field. It's very hard to use a body fitting grid which is unstructured mesh to determine the cell in which particles locate. This requires additional memory and complex scheme which may slow down the computation time. Thus, a structured Cartesian mesh PIC code is needed where the location of memory of quantities defined in neighboring cells can be found trivially via indexing.

A Cartesian grid method has some advantages to solve an interface problem. First, the Cartesian grid generation is trivial and almost costless, and this becomes much more significant for moving boundary and interface problems [23, 24]. Second, many efficient and popular used numerical methods are available for Cartesian grids. It will be relatively easier to incorporate new methods using existing solver based on the grid. Thirdly, physical quantities are much easier to construct using this Cartesian grid. The field interpolation to particle positions and charge quantities deposition to mesh nodes are easier to complete. However, the numerical methods based on Cartesian grid should overcome some difficulties such as the low accuracy in field solve in the vicinity of object boundaries. There are non-smooth solutions on the interface if finite difference method is applied.

Some effort has been made to figure out this problem. Peskin [84, 88] introduced the immersed boundary method which used a regular Eulerian computational grid for the fluid mechanics together with a Lagrangian representation of the immersed boundary. This approach can be applied to problems of interaction between viscous impressible fluid and boundary immersed in the fluid. However it's designed for problems with only a singular source term and continuous coefficients. In 1995, Lapenta et al. [89]

applied the immersed boundary technique [90] of Peskin to the Particle-In-Cell model and the complex geometries can be accounted for easily without the need of complex unstructured grid. Osher and Sethian [85] proposed the level set method which can be successfully treat a number of moving interface problems, especially for those problems with topological changes in three dimensions. It can perform numerical computations involving curves and surfaces on a fixed Cartesian grid without parameterize the objects. Sussman [86] developed the level set method by smoothing out the discontinuous coefficients. The level set expression of interfaces makes the smoothing method easier for two and three dimensional problems. LeVeque and Li [87] introduced the immersed interface method in 1994. This is a second order accurate finite difference scheme which can be applied to one, two, three dimensional problems of elliptic, parabolic, hyperbolic and mixed type equations with discontinuous coefficients or singular sources along a general interface. However, the resulting linear system of equations is not symmetric positive definite, a property that is favorable for the stability of solutions. The stability of the algorithm may depend on the choice of additional grid points to the standard finite difference scheme. Hewett [80] introduced the embedded curved boundary method in 1997. It used piecewise-linear approximation to curved boundary for codes using orthogonal meshes. This method provides a method for problems with space charge emission. However the linear system of equations is still not symmetric positive definite. There are also some finite element discretization based Cartesian grid methods. Sakumar et al. [93] introduced the extended finite element method (X-FEM) in 2000. This method was designed specifically to model cracks in three-dimensions. In this method, a discontinuous function and the two-dimensional asymptotic crack-tip displacement fields are added to the finite element approximation to account for the crack using the notion of partition of unity. The additional functions are used to model the presence of cracks, voids or inhomogeneities, and also to improve the accuracy in problems.

Due to the conflicting requirements from an accurate field solver and a speedy particle pusher, the plasma object surface represents a major challenge in the application of PIC model. The finite element method with unstructured mesh and finite difference method based on Cartesian grids are not sufficient for large scale problems involving complex object boundary in simulation domain. The conventional methods are not enough to handle the three dimensional object plasma interaction problems.

Lin et al. [25] introduced the two-dimensional immersed finite element (IFE) method in 2001. This method constructs rectangular finite element space based on rectangular elements to be used for solution of boundary value problems with discontinuous coefficients. In 2003, Li et al. [23] extended this method to triangular elements and considered both nonconforming and conforming finite element space. A second order accurate was given for corresponding interpolation functions in maximum norm. In 2005, Kafafy et al. [26] extended this IFE method to three dimensional finite element

space based on tetrahedral elements.

This IFE method combines the advantages of Cartesian mesh and finite element method using unstructured mesh. There are some merits of the IFE method: First, structured mesh is used and independent of the interface with discontinuous coefficients. Particle push is easy to be finished using this structured mesh and the computational cost is saved a lot. Second, a second order accurate was given for corresponding interpolation functions in maximum norm. The IFE method can solve the interface problem with discontinuous coefficients accurately. Third, unlike Cartesian grid methods based on finite difference discretization, (Peskin, 1976 [84, 88], Osher, 1988 [85], LeVeque, 1994 [87], Hewett, 1997 [80]) this method provides a symmetric, positive definite system of equations, which is a favorable feature for numerical stability. In addition, resulting algebraic system consists of exactly the same number of unknowns as that based on shape functions defined at the nodes (compared with Sakumar [93], 2000, X-FEM). At last, each unknown in the IFE method has a clear physical meaning which is favorable for PIC simulations.

This IFE method uses a structured mesh independent of the boundary location. This method incorporates the complex geometry shape and the advantage of structured mesh. However, current IFE method assumes that there is a zero flux jump condition on interface which makes the problem a homogeneous interface boundary value problem. The IFE method solving the floating potential in charging problem should consider the accumulated charge on object interface and the non-zero flux jump condition is needed.

For surface charging problem which considers the surface charge, the non-zero flux jump condition is applied. Consider the electrostatic field on both sides of a surface between two different mediums with surface charge at the interface. An infinitesimal Gaussian pillbox straddles the interface between these mediums with different electric permittivity ε_1, ε_2, shown in Figure 1.2. The normal components of electric displacement **D** on each medium are related by [50]

$$(\mathbf{D}_2 - \mathbf{D}_1)\bullet\mathbf{n} = \sigma, \tag{1.19}$$

here **n** is the unit normal vector from medium 1 to medium 2 and σ is the surface charge density. The derivative flux condition becomes [50]

$$\left[\varepsilon\frac{\partial\Phi}{\partial\mathbf{n}}\right]\Bigg|_{\Gamma} = -(\varepsilon_2\mathbf{E}_2 - \varepsilon_1\mathbf{E}_1)\bullet\mathbf{n} = -\sigma. \tag{1.20}$$

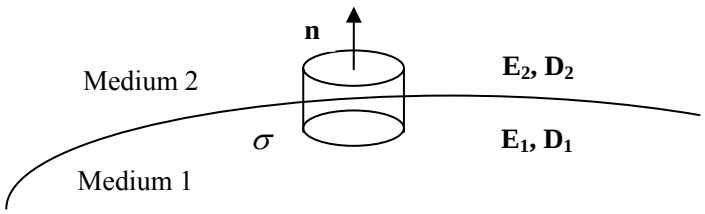

Figure 1.2: Boundary surface between different media

In Particle-In-Cell (PIC) method, the electrostatic field is solved time by time. The three dimensional IFE method developed by Kafafy, Lin, Wang et al. [26] can only be used to solve the homogeneous interface problem with condition

$$\left[\varepsilon \frac{\partial \Phi}{\partial \mathbf{n}}\right]\Big|_{\Gamma} = -(\varepsilon_2 \mathbf{E}_2 - \varepsilon_1 \mathbf{E}_1) \bullet \mathbf{n} = 0 . \tag{1.21}$$

For the interface with deposited charge where the non-zero flux jump condition is applied, the three-dimensional non-homogeneous interface IFE method should be developed including the condition defined by equation (1.20).

In 2009, He et al. [51, 91] developed the non-homogeneous interface IFE method for one-dimensional and two-dimensional space. It is able to solve the two dimensional second order elliptic boundary value problems with discontinuous coefficients and non-homogeneous flux jump condition using IFE method.

1.4 Objectives

In this dissertation, a three-dimensional immersed finite element (IFE) method is developed to solve the non-homogeneous interface problem which is required by solving the surface charging problem. The goal is to calculate the deposited charge on complex interface with high accuracy for discontinuous material property in a PIC simulation.

This numerical approach is motivated by modeling requirement from following three applications. The first is a simulation study of dust charging. A dust is a "small" object as its radius is much less than the Debye length, $r << \lambda_D$. Most analytical approach of dust charging calculations are based on orbital motion limited (OML) model. Lapenta [29] solved single dust charging problems use PIC with particle representation of objects. While the charging of single dust has been resolved, few studies have simulated the dust charging in dusty plasma where multiple charged dusts will interact with each other as well as the ambient plasma, as that shown in Figure 1.3. The problems of interest are those where the inter-duster distance is smaller than the Debye length. Under such a condition, the effect of neighboring dusts on dust charging and the accuracy of OML model are not known.

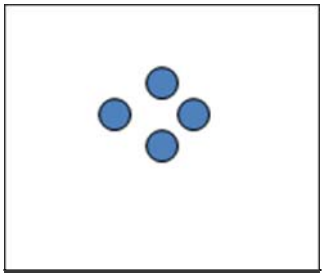

Figure 1.3 Sketch of multiple dusts interaction

The second application is a simulation study of secondary electron emission experiment. Secondary electron is an important charging mechanism in plasma-surface interactions. Existing measurements of secondary electron yield at low energy incident electron energy, which is more relevant to spacecraft charging applications, are very uncertain. The objective of this study is to support experimental studies to measure secondary electron yield, as that shown in Figure 1.4. This problem involves complex geometry shape (chamber geometry) and charging of target plate. In this dissertation, we considered the effects of complex geometry shape and facility potential to the secondary electron emission. The charging of target plate is not included.

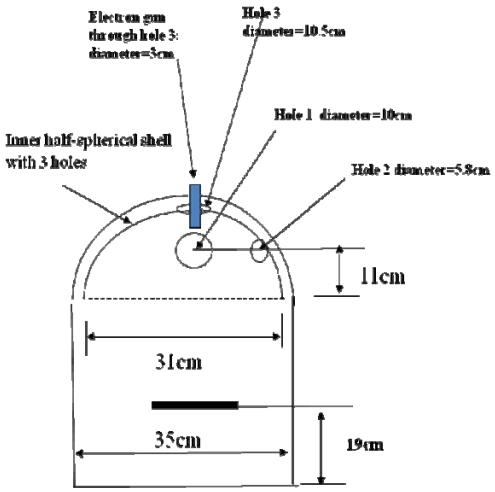

Figure 1.4 Secondary electron emission experiment setup

The third application is intended for a simulation study of the charging of lunar surface and lunar dust. This application is a combination of large object charging and small object charging. The large object (i.e. the lunar surface charging) is at a length scale larger or equal to the Debye length. The small object (i.e. dust) charging is at a scale much less than Debye length. While the Cartesian based finite difference PIC can be used to solve a non-flat surface using a "stair-case" approximation of boundary, such an approximation is limited by curvature at the same scale. The very different dimensional scales between the lunar surface and dust make it impossible to use finite difference with Cartesian mesh to solve this problem. While the IFE-PIC method is developed with the intention to solve charging involving objects of very different sizes. This dissertation only considered the lunar surface charging problem.

1.5 Outline

The rest of this dissertation is organized as follows.

Chapter 2 develops the three-dimensional immersed finite element (IFE) method for solving non-homogeneous interface boundary value problem with the non-zero flux jump boundary condition. Error analysis is given for this method. It's also applied to some physical problems such as the dielectric sphere in external electrostatic field and conductor sphere with uniform surface charge in free space.

Chapter 3 presents an overview of the IFE-PIC code where the developed non-homogeneous IFE method is used to simulate plasma-surface interaction and

surface charging together with PIC model.

Chapter 4 investigates the charging of single and multiple spherical objects in OML regime. Specifically, we consider the charging of a small sphere in both the stationary and flowing plasma and the charging of multiple small spheres with inter-object distance much smaller than the Debye length in a stationary plasma. This study is the initial step in investigating dust charging in dusty plasma.

Chapter 5 models the vacuum chamber experiment. The purpose of this chapter is to investigate the secondary electron emission model, and to assists the experimental measurement and of secondary electron under low energy electron impingement. It also studies facility error in a typical secondary electron measurement.

Chapter 6 simulates the lunar surface. The objective is to quantify the near-surface lunar plasma environment and surface charging for both flat and non-flat surface and spacecraft-on-lunar surface conditions. This study is also the initial step in modeling dust charging on lunar surface.

Last we present the results of the work in this dissertation. Future work is also proposed.

Chapter 2

Three-Dimensional Immersed Finite Element Method for Solving Electric Field

2.1 Introduction

In the three-dimensional immersed finite element (IFE) method [26] using a structured mesh, the plasma particles position can be easily determined. This greatly reduces the computational cost in plasma simulation. However, for surface charging problem with deposited charge on object surface, the non-zero flux jump condition is introduced and cannot be handled by previous IFE method which assumes a zero flux jump condition [26]. This chapter presents an extension of the IFE method for non-homogeneous interface boundary value problem with non-zero flux jump condition. First, this non-homogeneous interface boundary value problem is introduced in this chapter. The difference between this extended IFE method for non-homogeneous interface boundary value problem and the previous IFE method for homogeneous interface problem is described. Second, the three-dimensional IFE functions for non-homogeneous interface problem are developed. Thirdly, we will give the weak formulation of non-homogeneous problem. Then some numerical tests are conducted by making the exact solution as quadratic function. This new developed IFE solver is able to solve the interface boundary problems with zero or non-zero flux jump condition. Last, this IFE solver is used to solve the problems of dielectric spherical object in external electric field and uniformly charged conductive sphere object in free space. The results are compared with analytical solutions.

2.2 The Interface Boundary Value Problem

In electrostatic simulation of plasma-object interaction, the objects' surfaces divide the domain into two or more sub-domains and these surfaces become interfaces. Then the field problem in the domain can be considered as an interface boundary value problem. In a three-dimensional solution domain $\Omega \subset \mathbf{R}^3$, without loss of generality we assume the interface Γ is a surface separating Ω into two sub-domains Ω^+, Ω^- such that $\Omega = \Omega^+ \cup \Omega^- \cup \Gamma$, shown in Figure 2.1. The electric field $\Phi(\mathbf{x})$ is described by following interface problem of the three-dimensional Poisson's equation which is a partial differential equation (PDE) in Ω:

$$-\nabla\bullet(\varepsilon\nabla\Phi) = \rho, \quad \mathbf{x} = (x, y, z) \in \Omega \subset \mathbf{R}^3, \tag{2.1}$$

$$\Phi|_{\partial\Omega} = g. \tag{2.2}$$

Here, $\partial\Omega$ is the boundary where Dirichlet boundary conditions are applied. The electric permittivities of the different mediums cause the discontinuities of the PDE's coefficients ε. Thus, the electric permittivity of medium ε (x, y, z) is a piecewise constant function defined by

$$\varepsilon(x, y, z) = \begin{cases} \varepsilon^-, \mathbf{x} \in \Omega^- \\ \varepsilon^+, \mathbf{x} \in \Omega^+ \end{cases}.$$

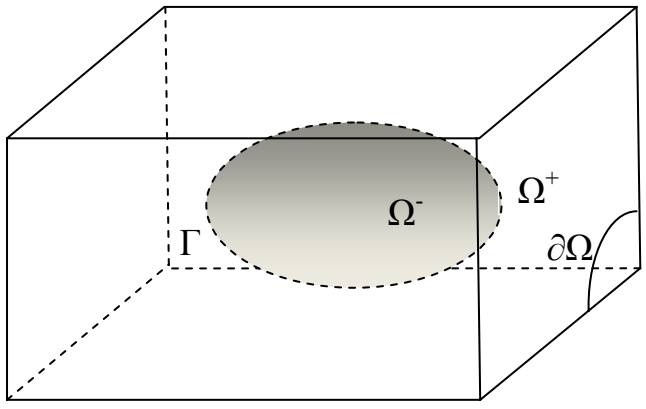

Figure 2.1 Sketch of the domain for the interface problem

Combining with the jump condition on the interface Γ

$$[\Phi]|_{\Gamma} = 0, \tag{2.3}$$

$$\left[\varepsilon \frac{\partial \Phi}{\partial n}\right]\Big|_{\Gamma} = 0, \tag{2.4}$$

we will get the boundary value problem with zero flux jump conditions as equation (2.4). Here, the square bracket denotes the jump of the involved function across the interface Γ. The equation (2.4) only satisfies the boundary value problem with certain conditions. In the application of surface charging problem which considers the deposited surface charge, the flux jump of equation (2.4) is non-zero as stated in section 1.2. Considering the electrostatic field on both sides of a surface between two different mediums with charge at the interface, the flux jump condition becomes [50]

$$\left[\varepsilon \frac{\partial \Phi}{\partial \mathbf{n}}\right]\Big|_{\Gamma} = -(\varepsilon_2 \mathbf{E}_2 - \varepsilon_1 \mathbf{E}_1) \bullet \mathbf{n} = -\sigma . \tag{2.5}$$

Here **n** is the unit normal vector from medium 1 to medium 2 (with different electric permittivity ε_1, ε_2 separately) and σ is the surface charge density. Thus, in our research, the equation (2.4) becomes a non-zero normal derivative jump condition on interface, which can be expressed as

$$\left[\varepsilon \frac{\partial \Phi}{\partial n}\right]\Big|_{\Gamma} = Q . \tag{2.6}$$

This non-zero flux jump makes the problem have non-homogeneous jump condition on interface. In order to apply the IFE method to surface charging problem with charge on interface, we need to develop the IFE method to solve the interface boundary problem with this non-homogeneous flux jump condition.

2.3 The Three-Dimensional IFE Space for Non-homogeneous Interface Problem

Before we develop this three dimensional IFE method for non-homogeneous interface

problems, the IFE method has been introduced for several years and some researchers have made much contribution to it. In 2001, Lin et al. [25] introduced the immersed finite element method which constructs a structured Cartesian mesh based on rectangular elements to be used for solving boundary value problems with discontinuous coefficients in PDE across interface in the domain. They used the basis functions to satisfy the interface jump conditions. In 2003, Li et al. [23] extended this method to triangular elements. The interpolation function of the method was proved to be second order accurate in the maximum norm. In 2005, Kafafy et al. [26] developed the three-dimensional IFE space which can use a structured mesh to solve the homogeneous three-dimensional interface problems. These works are assuming a zero flux jump condition on the interface. However, for surface charging problem considering deposited charge, the IFE method provided in reference [26] doesn't satisfy the non-zero flux jump condition in equation (2.6). We need to develop the IFE solver to handle the non-homogeneous interface condition. In 2009, He et al. [51, 91] developed the non-homogeneous interface IFE solver for one-dimensional and two-dimensional space. It is able to solve the two dimensional second order elliptic boundary value problems with discontinuous coefficients and non-homogeneous jump condition using IFE method. Based on the results in reference [26, 51, 91], we developed the IFE method to solve the three dimensional non-homogeneous interface problems in this dissertation. This three-dimensional IFE method for non-homogeneous interface problem is introduced in this section.

2.3.1 Intersection Topology of Interface Elements

As mentioned in Chapter 1, compared with body fitting grid, one advantage of IFE method in particles simulation is using a structured Cartesian mesh which is independent of the interface. When constructing this structured mesh $\mathcal{T}_h$, the solution domain Ω is first partitioned into uniform cubes whose edges are parallel to the coordinate axes. Then each uniform cube is partitioned into five tetrahedral elements such that the vertices of each tetrahedron are nodes forming the cube. Here, the partition of tetrahedral elements is independent of the interface surface and this mesh is a structured mesh. The interface surface may cross the element or not. Thus, there are two kinds of elements divided by the relation between the tetrahedral elements and interface surface: interface element, those elements intersecting with interface; and non-interface element, those elements having no intersection with interface [6].

Kafafy et al. [6] investigated the possible intersection topologies between a typical interface tetrahedron element and the interface. The intersection topology of interface elements can be stated as [6]:

"It is necessary to consider only two types of interface element, assuming that the

partition size is small enough compared to the interface surface curvature, the rest of interface elements can be effectively considered as non-interface element. These two typical intersection topologies are (shown in Figure 2.2)

1. *Three-edge cut: The interface surface Γ intersects with the edges of T at three distinct points which are not on the same face of T.*
2. *Four-edge cut: The interface surface Γ intersects with the edges of T at four distinct points on four different edges, and each three of these intersection points are not on a line."*

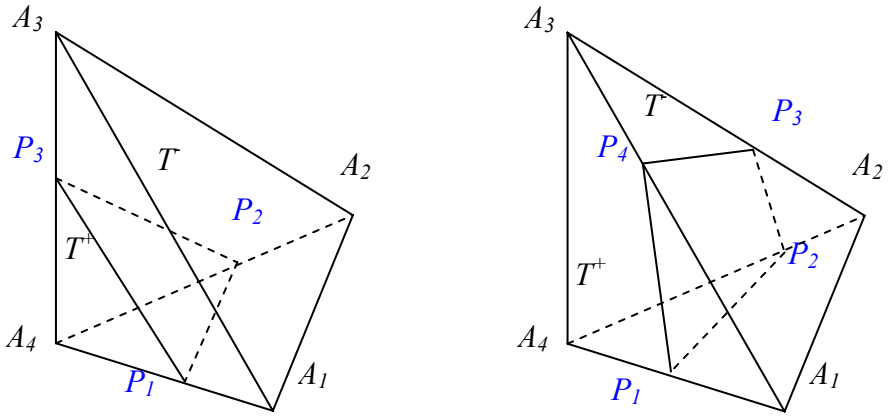

(a) Three-edge-cut (b) Four-edge-cut

Figure 2.2: Intersection topologies of tetrahedral elements

2.3.2 Three-Dimensional IFE Functions

After defining the non-interface and interface elements, we can have two kinds of basis function sets used for non-interface and interface elements, shown in Figure 2.3.

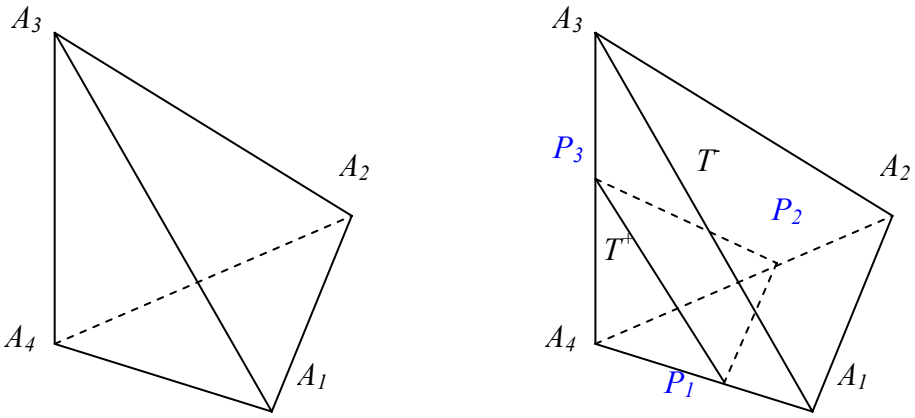

(a) (b)

Figure 2.3 IFE element (a) non-interface element; (b) interface element

Assume that A_1, A_2, A_3, A_4 are the four vertices of any tetrahedral element T. For non-interface elements, we use the linear local nodal finite element basis function

$$\overline{\varphi}_i(\mathbf{x}) = b_1 x + b_2 y + b_3 z + b_4, \quad \mathbf{x} \in T, \quad i = 1, 2, 3, 4, \tag{2.7}$$

satisfying the nodal value constraints:

$$\overline{\varphi}_i(A_j) = \begin{cases} 1, \text{ if } i = j \\ 0, \text{ if } i \neq j \end{cases}.$$

The local finite element space is defined by $S_h(T) = span\{\overline{\varphi}_i(\mathbf{x}), i = 1, 2, 3, 4\}$.

For interface element which is divided by the interface Γ into two subsets T^+ and T^- shown in Figure 2.3, as in the 1-D and 2-D cases [91], we will introduce two groups of IFE piecewise functions formed by linear polynomials which are defined separately in T^+ and T^-. The first group of IFE functions is representing the functions values at vertices of the element and the second group represents the non-zero flux jump on interface.

For the first group IFE functions, for each vertical node A_i, i = 1, 2, 3, 4, the local linear IFE basis functions are constructed as piecewise function [6]:

$$\varphi_i(\mathbf{x}) = \begin{cases} \varphi_i^+(\mathbf{x}) = b_{i,1} x + b_{i,2} y + b_{i,3} z + b_{i,4}, \ \mathbf{x} \in T^+, \\ \varphi_i^-(\mathbf{x}) = b_{i,5} x + b_{i,6} y + b_{i,7} z + b_{i,8}, \ \mathbf{x} \in T^-, \end{cases} \quad i = 1, 2, 3, 4. \tag{2.8}$$

In this piecewise IFE function, each polynomial has four coefficients to be determined. The values of the finite element functions on four vertices of the element provide four restrictions. We can have another three restrictions by requiring the continuity of the finite element function on points P_1, P_2 and P_3 at interface. Here, P_1, P_2 and P_3 are separately the intersection point of interface on A_1A_4, A_2A_4, A_3A_4, shown in Figure 2.3. Another condition can be obtained from the normal derivative jump condition on interface.

The vertex value condition leads to

$$\varphi_i(A_j)=\begin{cases}1, \text{ if } i=j,\\ 0, \text{ if } i\neq j,\end{cases} \qquad i,j=1,\,2,\,3,\,4\,.$$

The continuity condition $[\varphi]|_\Gamma=0$ leads to

$$\varphi_i^+(P_j)=\varphi_i^-(P_j)\,,$$

$$i=1,\,2,\,3,\,4 \text{ and } j=1,\,2,\,3\,.$$

The normal derivative jump condition $\left[\varepsilon\dfrac{\partial\varphi}{\partial n}\right]\Big|_\Gamma=0$ requires

$$\int_{\Gamma_T}\left(\varepsilon^+\frac{\partial\varphi_i^+}{\partial\mathbf{n}}-\varepsilon^-\frac{\partial\varphi_i^-}{\partial\mathbf{n}}\right)ds=0\,, \qquad i=1,\,2,\,3,\,4\,.$$

These constrains provide eight simultaneous linear algebraic equations about the coefficients of each local basis function for each basis function. Kafafy et al. [6] showed that these conditions are enough to precisely determine a local nodal basis function by transferring the interface element T to the reference tetrahedral element $\hat{T}$. These functions defined in (2.8) can satisfy the homogeneous flux jump condition across the interface. The local finite element space for the interface element is defined as $S_h(T)=span\{\varphi_i(\mathbf{x}),\, i=1,\,2,\,3,\,4\}$.

The other group of IFE functions in each interface element is constructed to handle the non-homogeneous flux jump condition. Let this function to be piecewise polynomial in the following form:

$$\varphi_{T,J}(\mathbf{x}) = \begin{cases} \varphi_{T,J}^{+}(\mathbf{x}) = b_1 x + b_2 y + b_3 z + b_4, \ \mathbf{x} \in T^{+} \\ \varphi_{T,J}^{-}(\mathbf{x}) = b_5 x + b_6 y + b_7 z + b_8, \ \mathbf{x} \in T^{-} \end{cases}. \tag{2.9}$$

Each polynomial has four coefficients to be determined. We set the values of the finite element function on four vertices of the element to be zero, and the integral of the derivative jump on interface to be unity. Combining with the continuity condition on the interface, we can have the following constrains:

nodal value specification: $\varphi_{T,J}(A_i) = 0, \qquad i = 1, 2, 3, 4$,

continuity across the interface: $\varphi_{T,J}^{+}(P_j) = \varphi_{T,J}^{-}(P_j), \qquad j = 1, 2, 3$,

derivative continuity across the interface: $\varepsilon^{+} \dfrac{\partial \varphi_{T,J}^{+}}{\partial \mathbf{n}} - \varepsilon^{-} \dfrac{\partial \varphi_{T,J}^{-}}{\partial \mathbf{n}} = 1$.

Similar as the nodal basis functions, these constrains also provide eight simultaneous linear algebraic equations about the coefficients in the derivative jump IFE function. To show how these conditions can be used to determine the IFE function, we transfer the interface element T to the reference tetrahedron $\hat{T}$ with affine transformation

$$\mathbf{x} = A_4 + \mathbf{B} \bullet \mathbf{l}. \tag{2.10}$$

The vertices of the reference tetrahedron $\hat{T}$ are $\hat{A}_1 = (1, 0, 0)^T$, $\hat{A}_2 = (0, 1, 0)^T$, $\hat{A}_3 = (0, 0, 1)^T$, and $\hat{A}_4 = (0, 0, 0)^T$. $\mathbf{x} = [x, y, z]^T$ is the coordinate of a point in interface element T, $\mathbf{l} = [l, m, n]^T$ is the coordinates of the corresponding point in the reference element. The transformation matrix is

$$\mathbf{B} = \begin{pmatrix} x_1 - x_4 & x_2 - x_4 & x_3 - x_4 \\ y_1 - y_4 & y_2 - y_4 & y_3 - y_4 \\ z_1 - z_4 & z_2 - z_4 & z_3 - z_4 \end{pmatrix}.$$

The derivative jump IFE function becomes the following form in the reference tetrahedron elements

$$\hat{\varphi}_{T,J}(\mathbf{l}) = \begin{cases} \hat{\varphi}_{T,J}^{+}(\mathbf{l}) = a_1 l + a_2 m + a_3 n + a_4, \ \mathbf{l} \in T^{+} \\ \hat{\varphi}_{T,J}^{-}(\mathbf{l}) = a_5 l + a_6 m + a_7 n + a_8, \ \mathbf{l} \in T^{-} \end{cases}. \tag{2.11}$$

The three edge cut topology and four edge cut topology are discussed separately to

show that this IFE function is determined by the constraints.

Three-edge cut element

Two typical cases for a three-edge cut interface in reference element are illustrated in Figure 2.4, and they will be considered separately. The interface intersects the interface element T at three points P_1, P_2 and P_3 which are on different edges of the interface element. If the vertex A_4 is on one side of the interface Γ and the other three vertices A_1, A_2, A_3 are on the other side, we call it case 1. If the vertex A_4 and another two vertices are on one side of the interface, and the other vertex is on the other side, we call it case 2. These two cases are plotted in Figure 2.4.

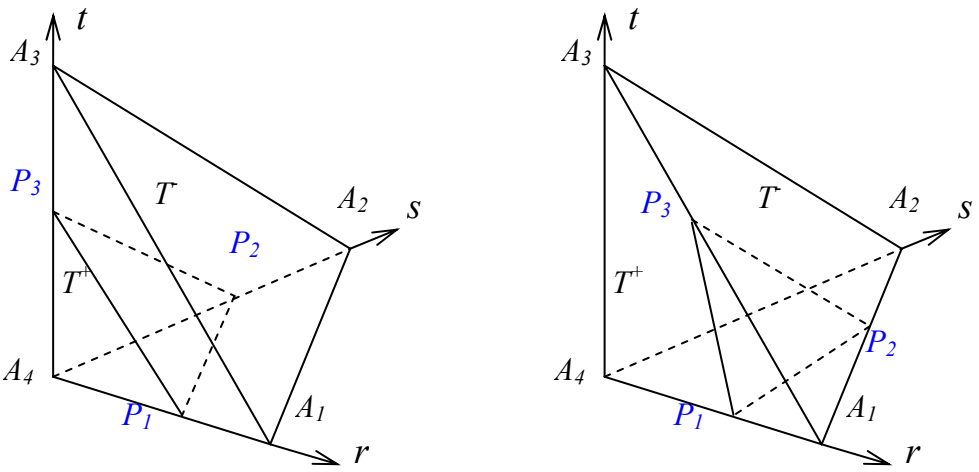

(a) Case 1 (b) Case 2

Figure 2.4 Two cases of three-edge cut in reference element

The mapped cutting points on three edges have the following coordinates:

Case 1:

$$\hat{P}_1=[\xi,0,0]^T,\quad \hat{P}_2=[0,\eta,0]^T,\quad \hat{P}_3=[0,0,\zeta]^T;$$

Case 2:

$$\hat{P}_1=[\xi,0,0]^T,\quad \hat{P}_2=[1-\eta,\eta,0]^T,\quad \hat{P}_3=[1-\zeta,0,\zeta]^T,$$

where $0\le\xi\le 1$, $0\le\eta\le 1$, $0\le\zeta\le 1$.

For case 1, the nodal value specifications lead to the following equations

$$a_4 = \hat{\varphi}_{T,J}(\hat{A}_4) = 0\,, \tag{2.12}$$

$$a_5 + a_8 = \hat{\varphi}_{T,J}(\hat{A}_1) = 0\,, \tag{2.13}$$

$$a_6 + a_8 = \hat{\varphi}_{T,J}(\hat{A}_2) = 0\,, \tag{2.14}$$

$$a_7 + a_8 = \hat{\varphi}_{T,J}(\hat{A}_3) = 0\,. \tag{2.15}$$

The continuity jump condition across the interface leads to

$$\xi a_1 + a_4 = \hat{\varphi}^{+}_{T,J}(\hat{P}_1) = \hat{\varphi}^{-}_{T,J}(\hat{P}_1) = \xi a_5 + a_8\,, \tag{2.16}$$

$$\eta a_2 + a_4 = \hat{\varphi}^{+}_{T,J}(\hat{P}_2) = \hat{\varphi}^{-}_{T,J}(\hat{P}_2) = \eta a_6 + a_8\,, \tag{2.17}$$

$$\zeta a_3 + a_4 = \hat{\varphi}^{+}_{T,J}(\hat{P}_3) = \hat{\varphi}^{-}_{T,J}(\hat{P}_3) = \zeta a_7 + a_8\,. \tag{2.18}$$

The unit normal vector $\mathbf{n} = [n_1,\ n_2,\ n_3]^T$ of the interface defined from T^- to T^+ is mapped to the vector $\hat{\mathbf{n}} = \mathbf{B}^{-1}\mathbf{n} = [\,\hat{n}_1,\ \hat{n}_2,\ \hat{n}_3]^T$ in the reference coordinates. The derivative condition becomes

$$\varepsilon^{+}\frac{\partial \hat{\varphi}^{+}_{T,J}}{\partial \hat{\mathbf{n}}} - \varepsilon^{-}\frac{\partial \hat{\varphi}^{-}_{T,J}}{\partial \hat{\mathbf{n}}} = 1\,.$$

This leads to

$$\varepsilon^{+}(\hat{n}_1 a_1 + \hat{n}_2 a_2 + \hat{n}_3 a_3) - \varepsilon^{-}(\hat{n}_1 a_5 + \hat{n}_2 a_6 + \hat{n}_3 a_7) = 1\,. \tag{2.19}$$

Solving above eight equations from (2.12) to (2.19), we can get the coefficients of $\hat{\varphi}_{T,J}$:

$$a_1 = \frac{1-\xi}{\xi}a_8, \qquad a_2 = \frac{1-\eta}{\eta}a_8,$$

$$a_3 = \frac{1-\zeta}{\zeta}a_8, \qquad a_4 = 0,$$

$$a_5 = -a_8, \qquad a_6 = -a_8,$$

$$a_7 = -a_8, \qquad a_8 = \frac{\lambda_1}{\beta^{+}\lambda_2 + \beta^{-}\lambda_3},$$

where

$$\lambda_1 = \xi\eta\zeta,$$
$$\lambda_2 = \hat{n}_1(1-\xi)\eta\zeta + \hat{n}_2(1-\eta)\xi\zeta + \hat{n}_3(1-\zeta)\xi\eta,.$$
$$\lambda_3 = (\hat{n}_1 + \hat{n}_2 + \hat{n}_3)\xi\eta\zeta.$$

For Case 2, the nodal value specifications lead to the following equations

$$a_4 = \hat{\varphi}_{T,J}(\hat{A}_4) = 0, \tag{2.20}$$

$$a_5 + a_8 = \hat{\varphi}_{T,J}(\hat{A}_1) = 0, \tag{2.21}$$

$$a_6 + a_8 = \hat{\varphi}_{T,J}(\hat{A}_2) = 0, \tag{2.22}$$

$$a_7 + a_8 = \hat{\varphi}_{T,J}(\hat{A}_3) = 0. \tag{2.23}$$

The continuity jump condition across the interface leads to

$$\xi a_1 + a_4 = \hat{\varphi}^+_{T,J}(\hat{P}_1) = \hat{\varphi}^-_{T,J}(\hat{P}_1) = \xi a_5 + a_8, \tag{2.24}$$

$$(1-\eta)a_1 + \eta a_2 + a_4 = \hat{\varphi}^+_{T,J}(\hat{P}_2) = \hat{\varphi}^-_{T,J}(\hat{P}_2) = (1-\eta)a_5 + \eta a_6 + a_8, \tag{2.25}$$

$$(1-\zeta)a_1 + \zeta a_3 + a_4 = \hat{\varphi}^+_{T,J}(\hat{P}_3) = \hat{\varphi}^-_{T,J}(\hat{P}_3) = (1-\zeta)a_5 + \zeta a_7 + a_8. \tag{2.26}$$

The derivative jump condition leads to

$$\varepsilon^+(\hat{n}_1 a_1 + \hat{n}_2 a_2 + \hat{n}_3 a_3) - \varepsilon^-(\hat{n}_1 a_5 + \hat{n}_2 a_6 + \hat{n}_3 a_7) = 1. \tag{2.27}$$

Solving above eight equations from (2.20) to (2.27), we can get the coefficients of $\hat{\varphi}_{T,J}$:

$$a_1 = \frac{1-\xi}{\xi}a_8, \qquad a_2 = -\frac{1-\eta}{\eta}\frac{1-\xi}{\xi}a_8,$$

$$a_3 = -\frac{1-\zeta}{\zeta}\frac{1-\xi}{\xi}a_8, \qquad a_4 = 0,$$

$$a_5 = -a_8, \qquad a_6 = -a_8,$$

$$a_7 = -a_8, \qquad a_8 = \frac{\lambda_1}{\beta^+\lambda_2 + \beta^-\lambda_3}.$$

where

$$\lambda_1 = \xi\eta\zeta,$$
$$\lambda_2 = \hat{n}_1(1-\xi)\eta\zeta - \hat{n}_2(1-\eta)(1-\xi)\zeta - \hat{n}_3(1-\zeta)(1-\xi)\eta,$$
$$\lambda_3 = (\hat{n}_1 + \hat{n}_2 + \hat{n}_3)\xi\eta\zeta.$$

Four-edge cut element

For the four-edge cut elements, there are three possible cases. One of them is plotted in Figure 2.5. The construction procedure for the IFE function and the discussion on their properties can be readily applied to any type of the four–edge cut elements [6], so we only consider the type shown in Figure 2.5.

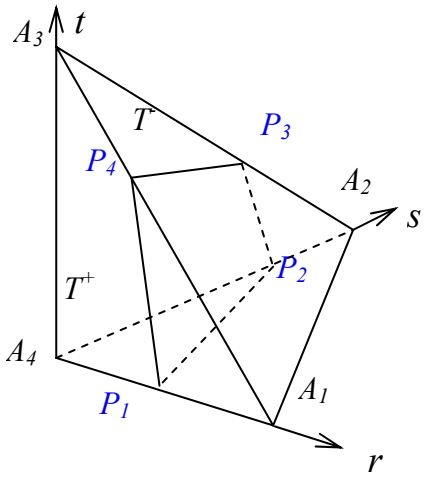

Figure 2.5 One of the three possible four-edge cut elements in the reference element

First, the physical interface surface inside the tetrahedral element should be replaced by a plane that is well approximated because the four intersection points on the edges may not belong to the same plane. Some procedures may be used to choose such an approximating plane [6]. This is done by neglecting the intersection point that has the minimum normal distance from the plane and remains the other three points. Using the transformation like three-edges cut, we can map the tetrahedral element T to the reference tetrahedral element $\hat{T}$. Assume the cutting point A_4 is eliminated, the other three cutting points become

$$\hat{P}_1 = [\xi, 0, 0]^T, \quad \hat{P}_2 = [0, \eta, 0]^T, \quad \hat{P}_3 = [0, 1-\zeta, \zeta]^T.$$

Next, construct the derivative jump basis function in the reference tetrahedron element like

$$\hat{\varphi}_{T,J}(\mathbf{l}) = \begin{cases} \hat{\varphi}^{+}_{T,J}(\mathbf{l}) = a_1 l + a_2 m + a_3 n + a_4, \mathbf{l} \in T^{+} \\ \hat{\varphi}^{-}_{T,J}(\mathbf{l}) = a_5 l + a_6 m + a_7 n + a_8, \mathbf{l} \in T^{-} \end{cases}.$$

Applying the nodal value specifications and the interface jump conditions we can get the nodal value specifications:

$$a_5 + a_8 = \hat{\varphi}_{T,J}(\hat{A}_1) = 0, \tag{2.28}$$

$$a_6 + a_8 = \hat{\varphi}_{T,J}(\hat{A}_2) = 0, \tag{2.29}$$

$$a_3 + a_4 = \hat{\varphi}_{T,J}(\hat{A}_3) = 0, \tag{2.30}$$

$$a_4 = \hat{\varphi}_{T,J}(\hat{A}_4) = 0. \tag{2.31}$$

The continuity jump condition across the interface leads to:

$$\xi a_1 + a_4 = \hat{\varphi}^{+}_{T,J}(\hat{P}_1) = \hat{\varphi}^{-}_{T,J}(\hat{P}_1) = \xi a_5 + a_8, \tag{2.32}$$

$$\eta a_2 + a_4 = \hat{\varphi}^{+}_{T,J}(\hat{P}_2) = \hat{\varphi}^{-}_{T,J}(\hat{P}_2) = \eta a_3 + a_8, \tag{2.33}$$

$$(1-\zeta) a_2 + \zeta a_3 + a_4 = \hat{\varphi}^{+}_{T,J}(\hat{P}_3) = \hat{\varphi}^{-}_{T,J}(\hat{P}_3) = (1-\zeta) a_6 + \zeta a_7 + a_8. \tag{2.34}$$

The derivative jump condition requires:

$$\varepsilon^{+}(\hat{n}_1 a_1 + \hat{n}_2 a_2 + \hat{n}_3 a_3) - \varepsilon^{-}(\hat{n}_1 a_5 + \hat{n}_2 a_6 + \hat{n}_3 a_7) = 1. \tag{2.35}$$

Solving above eight equations from (2.28) to (2.35), we can get the coefficients of $\hat{\varphi}_{T,J}$:

$$a_1 = \frac{1-\xi}{\xi} a_8, \qquad a_2 = \frac{1}{\eta} a_8,$$

$$a_3 = 0, \qquad a_4 = 0,$$

$$a_5 = -a_8, \qquad a_6 = -a_8,$$

$$a_7 = \frac{1-\zeta-\eta\zeta}{\eta\zeta} a_8, \qquad a_8 = \frac{\lambda_1}{\beta^{+}\lambda_2 + \beta^{-}\lambda_3}.$$

where

$$\lambda_1 = \xi\eta\zeta,$$
$$\lambda_2 = \hat{n}_1(1-\xi)\eta\zeta + \hat{n}_2\xi\zeta,$$
$$\lambda_3 = (\hat{n}_1 + \hat{n}_2)\xi\eta\zeta + \hat{n}_3(\eta\zeta + \zeta - 1)\xi.$$

Thus, the IFE function for non-zero flux jump condition can be uniformly determined for both three-edge and four-edge cut interface elements.

2.4 Approximation Capability of the IFE Functions

Based on the IFE functions introduced in the last section, the IFE approximation of continuous functions with non-zero flux jump condition on interface is discussed in this section. Numerical results are given to approximate the capability of these IFE functions. This shows the optimal approximation using these IFE functions to the non-homogeneous problem to solve.

Considering the same domain $\Omega \subset \mathbf{R}^3$ as that in section 2.2, the interface Γ is a surface separating Ω into two sub-domains Ω^+, Ω^- such that $\Omega = \Omega^+ \cup \Omega^- \cup \Gamma$, shown in Figure 2.1. The continuous function Φ is described by following interface problem of the three dimensional equation in Ω:

$$-\nabla\bullet(\varepsilon\nabla\Phi) = \rho, \quad \mathbf{x} = (x, y, z) \in \Omega \subset \mathbf{R}^3, \tag{2.1}$$

and on the interface Γ

$$[\Phi]|_\Gamma = 0, \tag{2.3}$$

$$\left[\varepsilon\frac{\partial\Phi}{\partial n}\right]\Big|_\Gamma = Q, \tag{2.6}$$

here, the square bracket denotes the jump of the involved function across the interface Γ. We can construct the interpolation of this continuous function on each element T in a partition mesh $\mathcal{T}_h$ of the domain.

If this element T is a non-interface element, the interpolation of Φ on T is defined as

$$I_{h,T}\Phi(\mathbf{x})=\sum_{i=1}^{4}\Phi(A_i)\bar{\varphi}_i(\mathbf{x}). \tag{2.36}$$

Here, $\mathbf{x} = (x, y, z)$ is in the element T. $\bar{\varphi}_i$, i =1, 2, 3, 4 are the standard linear local nodal basis functions on T as introduced in section 2.3.2.

For an interface element T, the interpolation of Φ on T is defined as

$$I_{h,T}\Phi(\mathbf{x})=\sum_{i=1}^{4}\Phi(A_i)\varphi_i(\mathbf{x})+q_T\varphi_{T,J}(\mathbf{x}). \tag{2.37}$$

Here, φ_i, i =1, 2, 3, 4 are the linear local nodal basis functions on T and $\varphi_{T,J}$ is the IFE function with unit flux jump. The parameter q_T is defined as

$$q_T=\frac{1}{S_{\Gamma\cap T}}\iint_{\Gamma\cap T}Q dS. \tag{2.38}$$

$\Gamma\cap$T is the interface in element T, $S_{\Gamma\cap T}$ is the area of $\Gamma\cap T$.

Let $I_h\Phi$ be the interpolation of Φ in the domain such that $I_h\Phi|_T = I_{h,T}(\Phi|_T)$ for any T in $\mathcal{T}_h$. A numerical example is provided to demonstrate that this interpolation can approximate Φ with an optimal convergence rate.

Consider a three-dimensional rectangle domain Ω = (-1,1) × (-1,1) × (-1,1). The interface Γ is a sphere locates at original point (0, 0, 0) with radius r_0=0.4051 which separates the domain into two subsets Ω^+, Ω^- with Ω^- = { $(x, y, z)| x^2+y^2+z^2 \le r_0^2$}, shown in Figure 2.6.

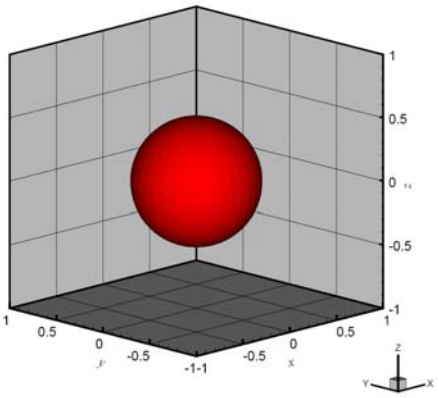

Figure 2.6 Geometry of the spherical interface problem [6]

The interface boundary value problem to be solved is

$$-\nabla \bullet (\varepsilon \nabla \Phi) = \rho(\mathbf{x}), \tag{2.1}$$

where the piecewise coefficients is given by

$$\varepsilon(\mathbf{x}) = \begin{cases} \varepsilon^-, \mathbf{x} \in \Omega^- \\ \varepsilon^+, \mathbf{x} \in \Omega^+ \end{cases}.$$

The function $\rho(\mathbf{x})$ is chosen as

$$\rho(x, y, z) = -12\,\varepsilon(x^2 + y^2 + z^2)^{1/2}. \tag{2.39}$$

Thus, the equation (2.1) has exact solution:

$$\Phi(x, y, z) = (x^2 + y^2 + z^2)^{3/2}. \tag{2.40}$$

The Dirichlet boundary conditions are applied to each domain face which can be written as:

$$\Phi(-1, y, z) = (1 + y^2 + z^2)^{3/2}, \quad \Phi(1, y, z) = (1 + y^2 + z^2)^{3/2},$$

$$\Phi(x, -1, z) = (x^2 + 1 + z^2)^{3/2}, \quad \Phi(x, 1, z) = (x^2 + 1 + z^2)^{3/2},$$

$$\Phi(x, y, -1) = (x^2 + y^2 + 1)^{3/2}, \quad \Phi(x, y, 1) = (x^2 + y^2 + 1)^{3/2}.$$

Because of the different ε value in subsets Ω^+, Ω^-, there will be a flux jump on the interface.

$$\begin{aligned} Q &= \left[\varepsilon \frac{\partial \Phi}{\partial \mathbf{n}} \right]\Big|_\Gamma = \varepsilon^+ \frac{\partial \Phi^+}{\partial \mathbf{n}} - \varepsilon^- \frac{\partial \Phi^-}{\partial \mathbf{n}} \\ &= \varepsilon^+ \left(\frac{\partial \Phi^+}{\partial x} n_1 + \frac{\partial \Phi^+}{\partial y} n_2 + \frac{\partial \Phi^+}{\partial z} n_3 \right) - \varepsilon^- \left(\frac{\partial \Phi^-}{\partial x} n_1 + \frac{\partial \Phi^-}{\partial y} n_2 + \frac{\partial \Phi^-}{\partial z} n_3 \right) \\ &= 3(\varepsilon^+ - \varepsilon^-)(x^2 + y^2 + z^2) \end{aligned}$$

Here **n** is the unit normal vector on the interface with the direction from Ω^- to Ω^+, and

n = $[n_1, n_2, n_3]^T$. The L^2 and H^1 norms of interpolation errors in the domain are defined as

$$I_0(h) = \left\| I_h\Phi - \Phi \right\|_{0,\Omega} = \sqrt{\int_\Omega \left| I_h\Phi - \Phi \right|^2 dx}\,, \tag{2.41}$$

$$\begin{aligned} I_1(h) &= \left| I_h\Phi - \Phi \right|_{1,\Omega} \\ &= \sqrt{\begin{aligned}&\int_\Omega \left| I_h\Phi - \Phi \right|^2 dx + \int_\Omega \left| (I_h\Phi - \Phi)_x \right|^2 dx \\ &+ \int_\Omega \left| (I_h\Phi - \Phi)_y \right|^2 dx + \int_\Omega \left| (I_h\Phi - \Phi)_z \right|^2 dx\end{aligned}}\,. \end{aligned} \tag{2.42}$$

Here, Φ is the exact solution and $I_h\Phi$ is the interpolated solution. $(I_h\Phi - \Phi)_x$, $(I_h\Phi - \Phi)_y$, $(I_h\Phi - \Phi)_z$ are the partial differential to x, y, z. There are three groups decreasing mesh sizes performed. Each group has a constant $\varepsilon^-/\varepsilon^+$ ratio, namely $\varepsilon^-/\varepsilon^+$ is 2, 10 and 1000. In each group, a Cartesian mesh is used to partition the domain into cubic mesh with size $h \times h \times h$. Each cubic mesh is then partitioned into five tetrahedron elements as that stated in section 2.3.1. The results of L^2 and H^1 interpolation errors are shown in Tables 2.1, 2.2 and 2.3. Plots of these interpolation errors are also shown in Figure 2.7.

h	$I_0(h)$	$I_1(h)$
1/20	0.00719936258	0.3061815025
1/25	0.00460761352	0.2449285280
1/32	0.00281226556	0.1913444061
1/40	0.00179986496	0.1530734428
1/50	0.00115190276	0.1224568242
1/64	0.00070306438	0.0956674239
1/80	0.00044996093	0.0765335987
1/100	0.00028797420	0.0612264756

Table 2.1: L^2 and H^1 interpolation errors of IFE functions with decreasing partition size h and $\varepsilon^+=1$, $\varepsilon^-=2$

h	$I_0(h)$	$I_1(h)$
1/20	0.0072011253	0.3064084987
1/25	0.0046087089	0.2450650103
1/32	0.0028127366	0.1914190935
1/40	0.0018002253	0.1531413615
1/50	0.0011520840	0.1225161078
1/64	0.0007031409	0.0956896792
1/80	0.0004500037	0.0765502622
1/100	0.0002879964	0.0612381480

Table 2.2: L^2 and H^1 interpolation errors of IFE functions with decreasing partition size h and $\varepsilon^+ = 1$, $\varepsilon^- = 10$

h	$I_0(h)$	$I_1(h)$
1/20	0.0072079280	0.3086005191
1/25	0.0046117477	0.2457867184
1/32	0.0028136822	0.1916161481
1/40	0.0018015357	0.1536064636
1/50	0.0011525791	0.1227258364
1/64	0.0007033320	0.0957616660
1/80	0.0004501219	0.0766323252
1/100	0.0002880853	0.0613199048

Table 2.3: L^2 and H^1 interpolation errors of IFE functions with decreasing partition size h and $\varepsilon^+ = 1$, $\varepsilon^- = 1000$

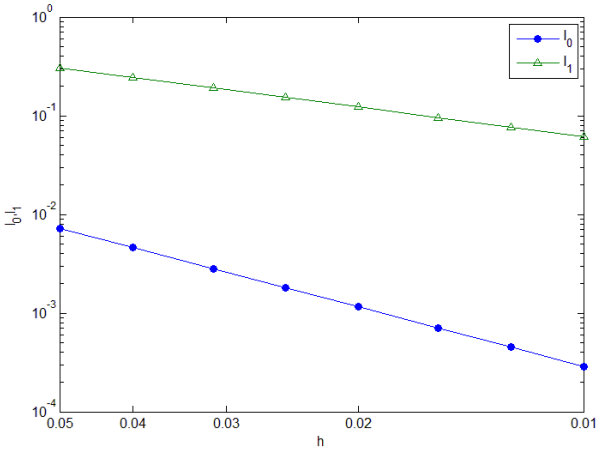

(a) Interpolation errors, $\varepsilon^+ = 1$, $\varepsilon^- = 2$

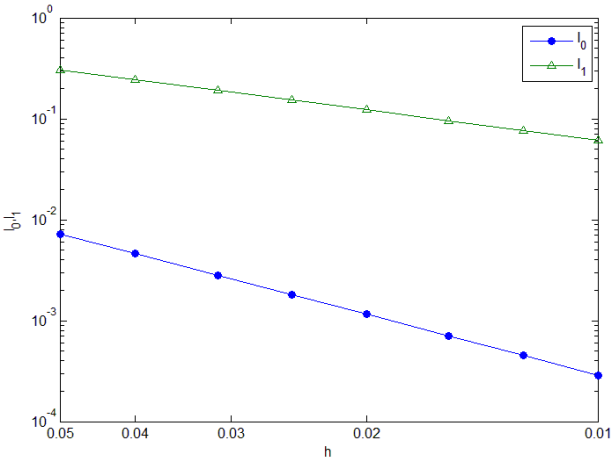

(b) Interpolation errors, $\varepsilon^+ = 1$, $\varepsilon^- = 10$

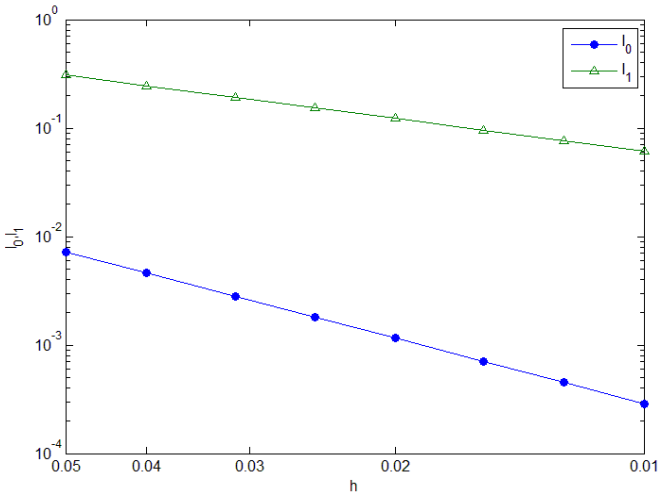

(c) Interpolation errors, $\varepsilon^+ = 1$, $\varepsilon^- = 1000$

Figure 2.7 Interpolation errors of spherical interface problem

For those numerical results with decreasing partition mesh size h listed from Table 2.1 to 2.3, we can get the convergence rates of L^2 and H^1 errors for these two cases. The relation between the errors and partition size h can be put in the regression form

$$Error=ah^b \ . \tag{2.43}$$

Here, a and b are two constants to be determined from the L^2 and H^1 interpolation errors. These parameter values for these ε^-, ε^+ groups are listed in Table 2.4.

	ε^+, ε^-	L^2 error		H^1 error	
		a	*b*	*a*	*b*
Quadratic function	1 , 2	2.880	2.00	6.125	1.00
	1, 10	2.881	2.00	6.134	1.00
	1, 1000	2.887	2.00	6.213	1.00

Table 2.4: Regression constants of interpolation error

The regression of interpolation error exactly shows the second order convergence for L^2 norm and first order convergence for H^1 norm for all the three ε^+, ε^- groups. This indicates the $I_h\Phi$ converge to Φ optimally in L^2 norm and H^1 norm for the linear basis functions we are using.

2.5 The IFE Method for Non-homogeneous Flux Jump Problem

The newly developed IFE functions optimally approximate the piecewise smooth functions with non-zero flux jump condition on the interface. In this section, those IFE functions developed in last section will be applied to solve problems with non-zero interface flux jump conditions. We will also present the numerical test using the developed IFE method to solve the three dimensional non-homogeneous boundary value problems.

The partial differential equation to solve in solution domain $\Omega= \Omega^+ \cap \Omega^- \cap \Gamma$ is

$$-\nabla \cdot (\varepsilon \nabla \Phi) = \rho \,, \tag{2.1}$$

$$\Phi|_{\partial\Omega} = g \,. \tag{2.2}$$

$$\varepsilon(x, y, z) = \begin{cases} \varepsilon^-, \mathbf{x} \in \Omega^- \\ \varepsilon^+, \mathbf{x} \in \Omega^+ \end{cases}.$$

On the interface Γ

$$[\Phi]|_\Gamma = 0 \,, \tag{2.3}$$

$$\left[\varepsilon \frac{\partial \Phi}{\partial n} \right]\Big|_\Gamma = Q \,. \tag{2.6}$$

Let

$$H_0^1(\Omega) = \left\{ \Phi \in H^1(\Omega) : \Phi = 0 \text{ on } \partial\Omega \right\}.$$

Multiply both sides of the PDE by test function w(x) and integrate over the domain Ω^s (s = +, -), we can get

$$-\iiint_{\Omega^s} w \nabla .(\varepsilon^s \nabla \Phi)\, d\Omega = \iiint_{\Omega^s} w \rho \, d\Omega \,, \quad \forall w \in H_0^1(\Omega) \tag{2.44}$$

The application of Green's theorem leads to

$$\iiint_{\Omega^s} \varepsilon^s \nabla w . \nabla \Phi \, d\Omega - \iint_{\partial\Omega^s} \varepsilon^s w \frac{\partial \Phi}{\partial n} d\Gamma = \iiint_{\Omega^s} w \rho \, d\Omega \,, s = +, -, \forall w \in H_0^1(\Omega) \tag{2.45}$$

Summing the Ω^s (s = +, -) together, we can get

$$\iiint_{\Omega} \varepsilon \nabla w . \nabla \Phi \, d\Omega - \iint_{\Gamma} \varepsilon^- w \frac{\partial \Phi^-}{\partial n_\Gamma} dS + \iint_{\Gamma} \varepsilon^+ w \frac{\partial \Phi^+}{\partial n_\Gamma} dS - \iint_{\partial\Omega} \varepsilon w \frac{\partial \Phi}{\partial n} dS = \iiint_{\Omega} w \rho \, d\Omega \,,$$

$$\forall w \in H_0^1(\Omega) \tag{2.46}$$

We are using a test function w and make it to be zero on domain boundary. The weak formulation of the interface problem can be written as

$$\iiint_{\Omega} \varepsilon \nabla w . \nabla \Phi \, d\Omega + \iint_{\Gamma} w \left[\varepsilon^+ \frac{\partial \Phi^+}{\partial n_\Gamma} - \varepsilon^- \frac{\partial \Phi^-}{\partial n_\Gamma} \right] dS = \iiint_{\Omega} w \rho \, d\Omega \,,$$

$$\forall w \in H_0^1(\Omega)\,. \tag{2.47}$$

It becomes

$$\iiint_\Omega \varepsilon\, \nabla w.\nabla \Phi \, d\Omega = \iiint_\Omega w\, \rho \, d\Omega - \iint_\Gamma w Q \, dS \,, \forall w \in H_0^1(\Omega)\,, \tag{2.48}$$

because

$$Q = \varepsilon^+ \frac{\partial \Phi^+}{\partial n_\Gamma} - \varepsilon^- \frac{\partial \Phi^-}{\partial n_\Gamma}\,. \tag{2.6}$$

For each node $\mathbf{x}_i$ in the mesh $\mathcal{T}_h$, we define the global IFE basis function $\phi_i(\mathbf{x})$ as $\phi_i|_T \in S_h(T)$ for any element T and $\phi_i(\mathbf{x}_j) = \delta_{ij}$ for any node $\mathbf{x}_j$ in the mesh $\mathcal{T}_h$. Here, ϕ_i is continuous at every node $\mathbf{x}_j$ in the mesh. Then we can define the IFE space $S_h(\Omega)$ in the whole domain as $S_h(\Omega) = span\{\phi_i(\mathbf{x}),\ \mathbf{x}_i \in \mathcal{T}_h\}$. For each interface element T, its IFE function $\varphi_{T,J}$ handling the flux jump condition is used to define a corresponding global function $\phi_{T,J}$ with zero value outside the interface element T. Considering the non-homogeneous jump condition, the function $\Phi_h(\mathbf{x})$ can be approximated by

$$\Phi_h(\mathbf{x}) = \sum_{j=1}^{NON} \Phi(\mathbf{x}_j)\phi_j(\mathbf{x}) + \sum_{j=1}^{NOB} g(\mathbf{x}_j)\phi_j(\mathbf{x}) + \sum_{k=1}^{NOI} q_{T,k}\phi_{T,J}(\mathbf{x})\,. \tag{2.49}$$

Here *NON* is the number of nodes in Ω, *NOB* is the number of boundary nodes, and *NOI* is the number of interface elements. $g(\mathbf{x})$ is given as the boundary condition. $q_{T,k}$ is the average flux jump in the k^{th} interface element.

From equation (2.48), we can get the IFE method for non-homogeneous interface problem with non-zero flux jump condition on interface: for each node $\mathbf{x}_i$ in Ω,

$$\begin{aligned}
&\sum_{j=1}^{NON}\left(\sum_{T\in\mathcal{T}_h}\iiint_T \varepsilon\,\nabla\phi_i.\nabla\phi_j\,d\Omega\right)\Phi_j \\
&= \iiint_\Omega \phi_i\,\rho\,d\Omega - \iint_\Gamma \phi_i Q\,dS - \sum_{j=1}^{NOB}\left(\sum_{T\in\mathcal{T}_h}\iiint_T \varepsilon\,\nabla\phi_i.\nabla\phi_j\,d\Omega\right)g(\mathbf{x}_j) \\
&-\sum_{k=1}^{NOI} q_{T,k}\left(\iiint_T \varepsilon\,\nabla\phi_i.\nabla\phi_{T,J}\,d\Omega\right)
\end{aligned} \tag{2.50}$$

If the flux jump $Q = 0$, this IFE method becomes the one designed for homogeneous

interface problem with zero jump condition developed in [26, 42].

Consider using the IFE functions on a tetrahedron mesh to solve the numerical test problem mentioned in last section. We investigate the errors of IFE solution with various partition sizes by evaluating the L^2 and H^1 errors. The results are shown in Tables 2.5, 2.6 and 2.7. Plots of these solution errors are also shown in Figure 2.8. Figure 2.9 shows the solution and error of Φ on z=0 plane for the case of ε^+ =1, ε^- =2 and partition size h=1/64. The maximum error is 0.0014033375 which is 2.1% of the exact solution. This small relative error shows a precise enough solution using this IFE method to solve the non-homogeneous interface boundary value problem.

The following definitions are used to get the L^2 and H^1 norms of the solution errors.

$$E_0(h) = \left\|\Phi_h - \Phi\right\|_{0,\Omega} = \sqrt{\int_\Omega \left|\Phi_h - \Phi\right|^2 dx}\,, \tag{2.51}$$

$$\begin{aligned} E_1(h) &= \left|\Phi_h - \Phi\right|_{1,\Omega} \\ &== \sqrt{\begin{array}{l}\int_\Omega \left|\Phi_h - \Phi\right|^2 dx + \int_\Omega \left|(\Phi_h - \Phi)_x\right|^2 dx \\ + \int_\Omega \left|(\Phi_h - \Phi)_y\right|^2 dx + \int_\Omega \left|(\Phi_h - \Phi)_z\right|^2 dx\end{array}}\,. \end{aligned} \tag{2.52}$$

h	$E_0(h)$	$E_1(h)$
1/20	0.0055169524	0.2419986152
1/25	0.0035467267	0.1925017621
1/32	0.0021499146	0.1493660743
1/40	0.0013533077	0.1188110521
1/50	0.0008688439	0.0947487154
1/64	0.0005292758	0.0738441154
1/80	0.0003362958	0.0589198287
1/100	0.0002153340	0.0470062393

Table 2.5: L^2 and H^1 errors of the IFE solutions with decreasing partition size h and ε^+ =1, ε^- =2

h	$E_0(h)$	$E_1(h)$
1/20	0.0054906375	0.2450133031
1/25	0.0035059726	0.1961992883
1/32	0.0021427514	0.1534247800
1/40	0.0014925692	0.1244385765
1/50	0.0009655773	0.0996293564
1/64	0.0005969836	0.0791868937
1/80	0.0004407878	0.0641339116
1/100	0.0002955388	0.0517271333

Table 2.6: L^2 and H^1 errors of the IFE solutions with decreasing partition size h and $\varepsilon^+ = 1$, $\varepsilon^- = 10$

h	$E_0(h)$	$E_1(h)$
1/20	0.1293372247	0.7129055986
1/25	0.0592995813	0.6989732933
1/32	0.0461423831	0.5021845653
1/40	0.0652337199	0.6794934693
1/50	0.0325485501	0.6553542027
1/64	0.0198198803	0.3441612814
1/80	0.0230412992	0.3712168568
1/100	0.0149402932	0.2866987401

Table 2.7: L^2 and H^1 errors of the IFE solutions with decreasing partition size h and $\varepsilon^+ = 1$, $\varepsilon^- = 1000$

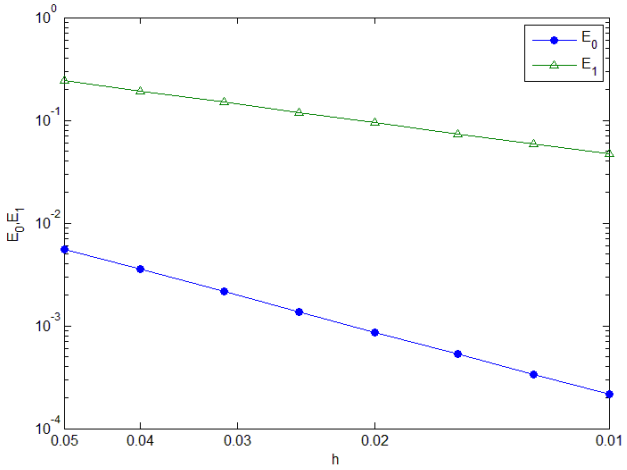

(a) Solution errors, ε^+ =1, ε^- =2

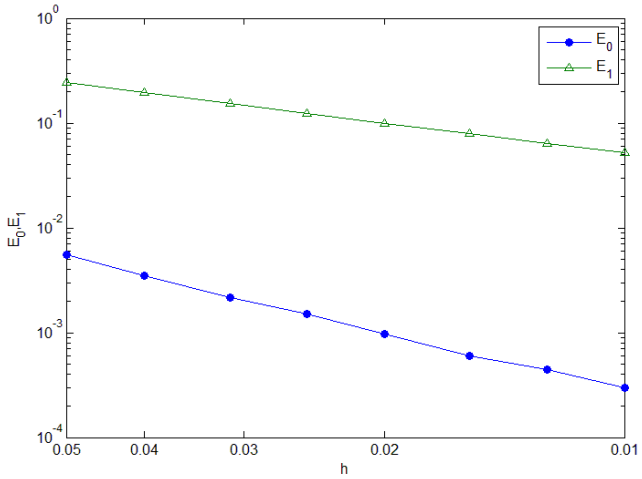

(b) Solution errors, ε^+ =1, ε^- =10

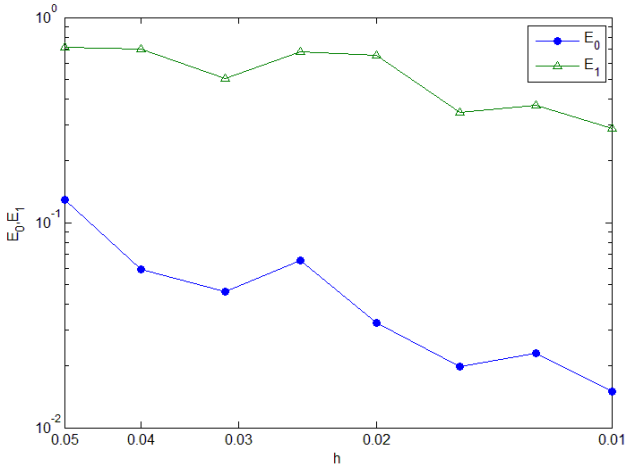

(c) Solution errors, ε^+ =1, ε^- =1000

Figure 2.8 Solution errors of spherical interface problem

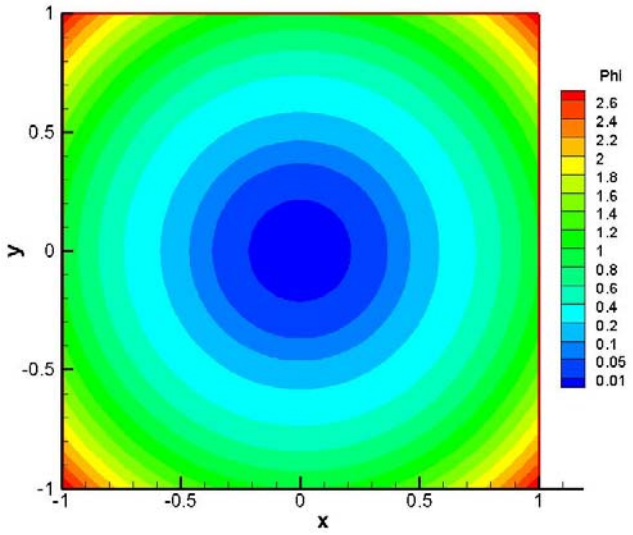

(a) Solution

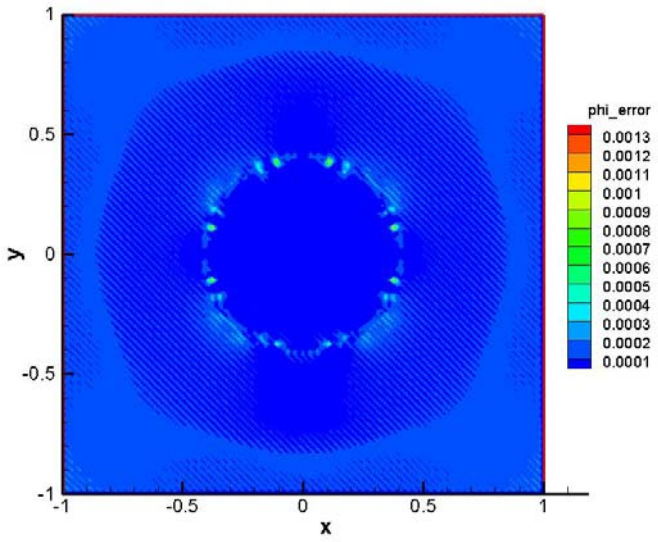

(b) Solution error

Figure 2.9: The solution and error for the case of ε^{+} =1, ε^{-} =2 and h=1/64

	ε^{+}, ε^{-}	L^2 error		H^1 error	
		a	*b*	*a*	*b*
Quadratic function	1 , 2	2.340	2.02	5.091	1.02
	1, 10	1.186	1.81	4.363	0.96
	1, 1000	3.590	1.19	4.144	0.55

Table 2.8: Regression constants of solution error

Unlike the regression of interpolation error which optimally shows the second order convergence for L^2 error and first order convergence for H^1 error for all the three groups of ε^+, ε^-, only small $\varepsilon^-/\varepsilon^+$ groups such as 2 and 10 have the regression of solution error approximately second order convergence for L^2 error and first order convergence for H^1 error. The solution of $\varepsilon^-/\varepsilon^+$ =1000 case doesn't have the expected optimal convergence order.

Considering the observed accuracy order [52] of the solution, for a group of mesh size h_1 (fine mesh), h_2 (medium mesh), h_3 (coarse mesh) with a constant grid refinement factor $r = h_2/h_1 = h_3/h_2$, we define the solution error integral in the domain with mesh size h_i as $\mathrm{DE}_i = \iiint_\Omega (\Phi_{exact} - \Phi_i)\mathrm{dV}$, i = 1, 2, 3, where Φ_{exact} is the exact solution and Φ_i is the solution in domain Ω for h_i. The observed order of accuracy $p_1$and p_2 are given by [52]

$$p_1 = \frac{\ln\left(\frac{\mathrm{DE}_2}{\mathrm{DE}_1}\right)}{\ln(r)}, \tag{2.53}$$

$$p_2 = \frac{\ln\left(\frac{\mathrm{DE}_3}{\mathrm{DE}_2}\right)}{\ln(r)}. \tag{2.54}$$

Table 2.9 to 2.11 list the observed accuracy order using two mesh refinement groups for each $\varepsilon^-/\varepsilon^+$ value.

	Mesh size h_i	Solution error integral DE_i
h_3 Coarse mesh	1/20	-0.008961875485
h_2 Medium mesh	1/40	-0.002165155479
h_1 Fine mesh	1/80	-0.000522683051
Accuracy order p_1	2.0493	
Accuracy order p_2	2.0505	
Average p	2.0499	

Table 2.9 Observed solution accuracy order for r = 2 and ε^+ =1, ε^- =2

	Mesh size h_i	Solution error integral DE_i
h_3 Coarse mesh	1/20	-0.008049401530
h_2 Medium mesh	1/40	-0.001815647055
h_1 Fine mesh	1/80	-0.000414157828
Accuracy order p_1	2.1484	
Accuracy order p_2	2.1322	
Average p	2.1403	

Table 2.10 Observed solution accuracy order for $r = 2$ and $\varepsilon^+ = 1$, $\varepsilon^- = 10$

	Mesh size h_i	Solution error integral DE_i
h_3 Coarse mesh	1/20	-0.076532122558
h_2 Medium mesh	1/40	-0.029247594151
h_1 Fine mesh	1/80	-0.024426054748
Accuracy order p_1	1.3877	
Accuracy order p_2	0.2599	
Average p	0.8238	

Table 2.11 Observed solution accuracy order for $r = 2$ and $\varepsilon^+ = 1$, $\varepsilon^- = 1000$

For the small $\varepsilon^-/\varepsilon^+$ ratio, the solution optimally gives the second order accuracy, however, this is not as expected for large $\varepsilon^-/\varepsilon^+$ ratio. Thus, the current development of the non-homogeneous IFE solver can solve the small $\varepsilon^-/\varepsilon^+$ ratio problems well. The further investigation is needed for large $\varepsilon^-/\varepsilon^+$ ratio problems using this non-homogeneous IFE solver.

2.6 Code Testing

In this section, we will use two simple physics problems to test the field solver with non-homogeneous conditions: dielectric sphere in initially uniform external electrostatic field and conductive sphere with uniform surface charge in free space. The developed IFE method for both homogeneous problem and non-homogeneous problem are applied to solve these physics problems and this developed method is validated in these cases. The homogeneous IFE method is used in dielectric sphere in external electrostatic field problem. Then the problem of conductive sphere with uniform distributed surface charge is solved with the IFE method for

non-homogeneous interface problem.

As stated in Chapter 1, for object-plasma interaction problems, if there is some deposited charge on interface of two medium, the flux jump condition is [50]

$$\left[\varepsilon \frac{\partial \Phi}{\partial \mathbf{n}} \right] \Big|_{\Gamma} = -(\varepsilon_2 \mathbf{E}_2 - \varepsilon_1 \mathbf{E}_1) \bullet \mathbf{n} = -\sigma \,, \tag{2.5}$$

here **n** is the unit normal vector from medium 1 to medium 2 and σ is the macroscopic surface charge density which doesn't include the induced polarization charge of the object. If there is some charge deposited on the surface, σ is non-zero and this becomes the non-homogeneous interface problem. If there is no charge deposition, this σ is zero and homogeneous IFE method is applied.

2.6.1 Dielectric Sphere in External Electric Field

A dielectric sphere of radius r_0 and dielectric constant ε_1 is placed in an initially uniform external electric field. There exists a medium with dielectric constant ε_0 outside the sphere. There is no free charge inside or outside the sphere. Then the problem is governed by the Laplace equation (the right hand side of the Poisson equation equals to zero):

$$-\nabla \cdot (\varepsilon \nabla \Phi) = 0 \,, \tag{2.55}$$

where ε is ε_1 and ε_0 inside and outside the sphere. In this application, the problem is to solve the Φ for both nodes inside and outside sphere with certain boundary conditions at sphere surface. Because of no macroscopic surface charge, this problem is a homogeneous interface problem with zero flux jump condition on interface.

We are using the center of the sphere as the original point. The initially uniform electric field **E** is directed along the x axis and the magnitude is E_0. The analytical solution for this problem is

If $r \le r_0$, $\quad \Phi = -\dfrac{3\varepsilon_0 E_0 x}{\varepsilon_1 + 2\varepsilon_0}$;

If $r > r_0$, $\quad \Phi = -E_0 x + \dfrac{\varepsilon_1 - \varepsilon_0}{\varepsilon_1 + 2\varepsilon_0} \dfrac{r_0^3}{\left(\sqrt{x^2 + y^2 + z^2}\right)^3} E_0 x$.

The flux jump condition on interface is

$$Q=\left[\varepsilon\frac{\partial\Phi}{\partial\mathbf{n}}\right]=\varepsilon_0\left[-\frac{E_0x}{\sqrt{x^2+y^2+z^2}}-\frac{2(\varepsilon_1-\varepsilon_0)}{\varepsilon_1+2\varepsilon_0}\frac{r_0^3E_0x}{\left(x^2+y^2+z^2\right)^2}\right]+\frac{3\varepsilon_0\varepsilon_1E_0}{\varepsilon_1+2\varepsilon_0}\frac{x}{\sqrt{x^2+y^2+z^2}}=0\cdot \qquad (2.56)$$

The homogeneous interface IFE method is applied to this problem. The sphere is placed in a three-dimensional rectangular domain Ω = (-1,1) × (-1,1) × (-1,1). The interface Γ is a sphere located at the origin point (0, 0, 0) with radius r_0=0.4051 which separate the domain into two subsets Ω^+, Ω^- with Ω^- = $\{(x, y, z)|\ x^2+y^2+z^2 \le r_0^2\}$. The Figure 2.10 shows the 2D IFE mesh when partition size h=1/25. The electric permittivity inside and outside the sphere is separately ε_1=4 and ε_0=1. The initial uniform external electric field magnitude is E_0=0.1.

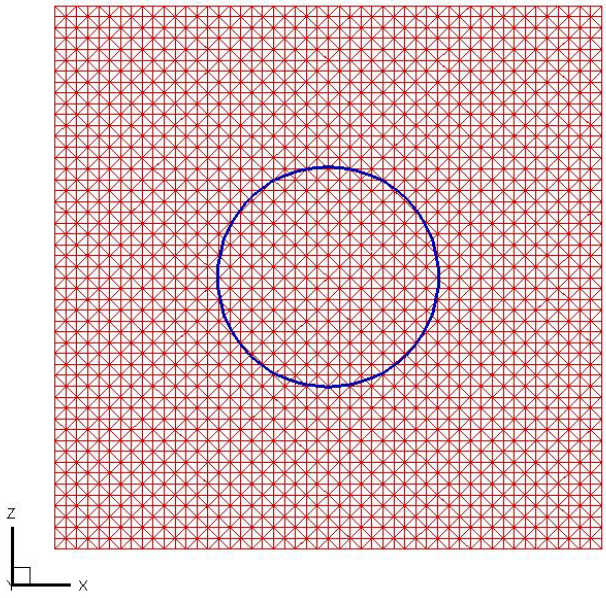

Figure 2.10 IFE mesh of the dielectric sphere in external electrostatic field

We investigate the errors of the solution with decreasing partition sizes by evaluating the L^2 and H^1 errors. We are using following definition to get the L^2 and H^1 norms of the solution errors

$$E_0(h)=\left\|\Phi_h-\Phi\right\|_{0,\Omega}=\sqrt{\int_\Omega\left|\Phi_h-\Phi\right|^2dx}\ , \qquad (2.51)$$

$$E_1(h) = \left|\Phi_h - \Phi\right|_{1,\Omega} = = \sqrt{\begin{array}{l}\int_\Omega \left|\Phi_h - \Phi\right|^2 dx + \int_\Omega \left|(\Phi_h - \Phi)_x\right|^2 dx \\ + \int_\Omega \left|(\Phi_h - \Phi)_y\right|^2 dx + \int_\Omega \left|(\Phi_h - \Phi)_z\right|^2 dx\end{array}}. \quad (2.52)$$

The results are shown in Table 2.12. The relation between the errors and partition size h can be put in the regression form $Error=ah^b$. The constants a, b for L^2 and H^1 norms are listed in Table 2.13. The regression of this error shows the second order convergence for L^2 error and first order convergence for H^1 error. Figure 2.11 shows the solution and error of Φ on z=0 plane for the case of ε_1=4, ε_0=1 and partition size h=1/50. The maximum error is 0.0005319887 which is 2.6% of the exact solution (0.020255). From this application, we can see that the IFE method can accurately solve the homogeneous interface problem with zero flux jump condition.

h	$E_0(h)$	$E_1(h)$
1/16	0.0003341593	0.0089793530
1/20	0.0002635079	0.0058752856
1/25	0.0001714569	0.0058558944
1/32	0.0001144103	0.0043499097
1/40	0.0000486189	0.0033949437
1/50	0.0000358540	0.0030688819
1/64	0.0000230243	0.0021894457

Table 2.12: L^2 and H^1 errors of the potential solutions with decreasing partition size h and ε_1=4, ε_0=1

ε_0, ε_1	L^2 error		H^1 error	
	a	b	a	b
1, 4	0.116	2.05	0.113	0.94

Table 2.13: Regression constants of solution error for dielectric sphere in external electric field

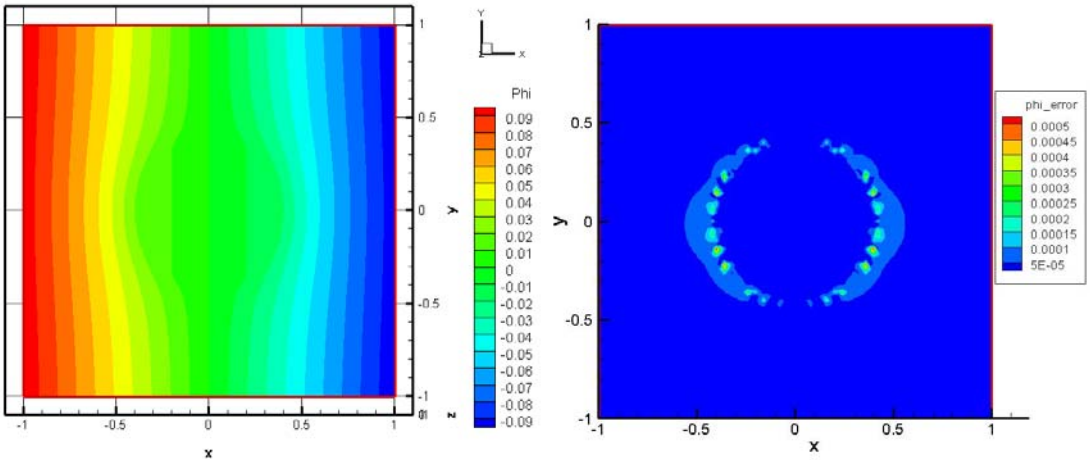

(a) Potential Solution (b) Error

Figure 2.11 Potential solution and error contours on z=0 plane for dielectric sphere in unifrom external electric field

2.6.2 Conductive Sphere with Uniformly Distributed Surface Charge

From the example in last section, the IFE method can solve the homogeneous interface problem well. For those objects with surface charge, the non-zero flux jump condition requires the IFE solver to handle the non-homogeneous interface problem. In this section, we will consider the case of conductive sphere which has uniformly distributed charge on its surface.

The isolated conductive spherical object with radius r_0 in vacuum with uniformly distributed surface charge has equi-potential on the surface of the sphere. There is no free charge inside or outside the sphere. Then the problem is governed by the Laplace equation:

$$-\nabla \cdot (\varepsilon \nabla \Phi) = 0 . \tag{2.55}$$

and the analytical potential in the space is

If $r \le r_0$, $\Phi = \dfrac{q}{4\pi\varepsilon_0 r_0}$;

If $r > r_0$, $\Phi = \dfrac{q}{4\pi\varepsilon_0 r}$.

Here, r is the distance from the sphere center to the space point, q is the sum of the

charge on object surface, ε_0 is the electric permittivity in free space. From this analytical solution, we can see that the flux jump on interface is

$$Q = \left[\varepsilon \frac{\partial \Phi}{\partial \mathbf{n}} \right] = -\frac{q}{4\pi r_0^2}, \tag{2.57}$$

which is the negatives surface charge density on object surface in physical meaning.

We are using the IFE method to solve this non-homogeneous interface problem. Here, the physical meaning of the flux jump on interface element is adopted. The total charge q is represented by some simulation macro particles from the idea of Particle-In-Cell method as mentioned in section 1.2.4. These particles are uniformly distributed on the object surface. The location of each particle is recorded and the number of particle in each interface element is counted. The surface charge density on the interface plane of each interface IFE element is obtained via dividing the charge on this interface by the area of the interface plane in this element. This is used as the flux jump Q in each interface element in the IFE method as that needed in equation (2.57).

Consider this problem in the domain of Ω = (-1, 1) × (-1, 1) × (-1, 1). The interface Γ is a sphere located at the origin point (0, 0, 0) with radius r_0=0.505. The total charge deposited on the object surface is q=-8. The ε_0 is chosen to be 1 and the ε_1 inside the sphere is 1000000. Using the IFE method developed in this chapter, we can solve the Laplace equation and obtain the potential distribution inside and outside the charged sphere. Figure 2.12 shows the 2D IFE mesh when partition size h=1/50. Figure 2.13 shows the solution of potential Φ on z=0 plane at this partition size h=1/50 and the error using IFE method. The maximum error is 0.0154028 which is 1.22% of the exact solution (1.2606332). This IFE method can well solve the physical problem about potential around the object with surface charge.

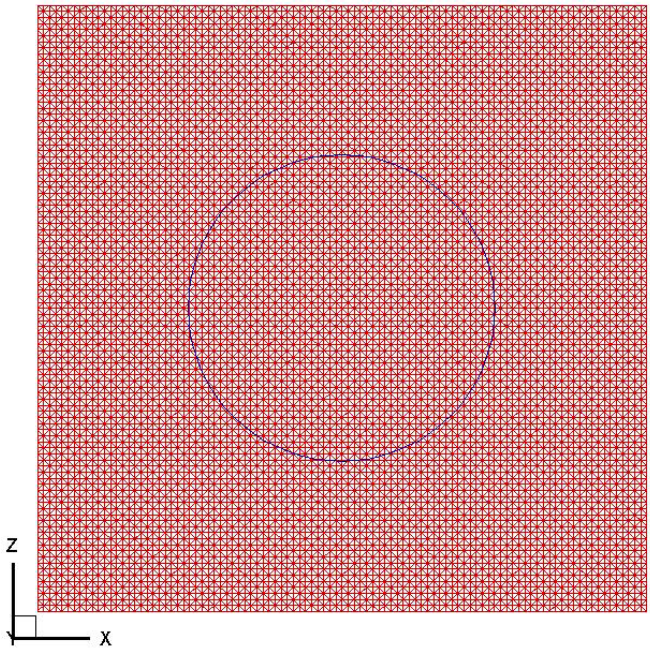

Figure 2.12 IFE mesh used in the simulation
of conductive sphere with uniformly distributed surface charge

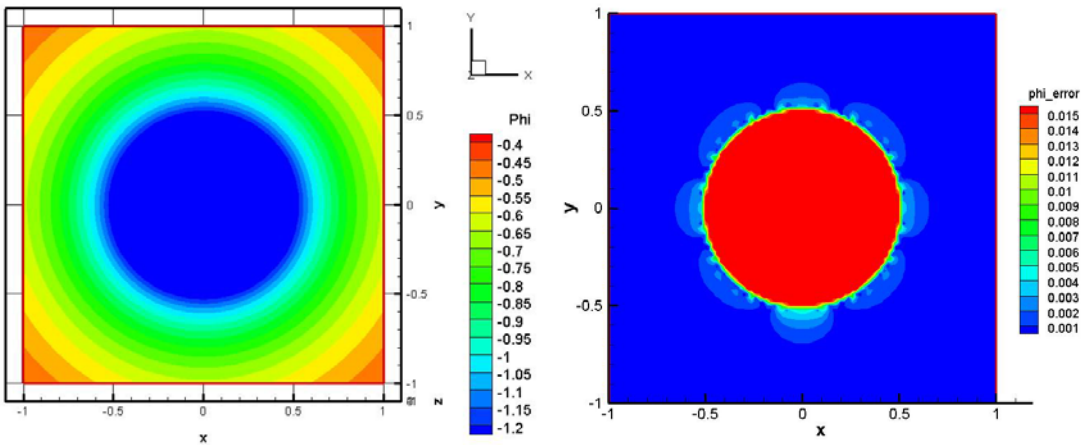

(a) Potential Solution (b) Error

Figure 2.13 Potential solution and error contours on z=0 Plane
for conductive sphere with uniform surface charge

In this problem, we are using the non-homogeneous IFE method to solve for the potential Φ in the domain. The weak formulation equation (2.48) is used.

$$\iiint_{\Omega} \varepsilon \nabla w . \nabla \Phi \, d\Omega = \iiint_{\Omega} w \rho \, d\Omega - \iint_{\Gamma} w Q \, dS \,, \forall w \in H_0^1(\Omega) \,, \tag{2.48}$$

Here, the Q is the negatives surface charge density on object surface in physical meaning. The equation (2.48) can be written as

$$\iiint_{\Omega} \varepsilon \nabla w . \nabla \Phi \, d\Omega = \iiint_{\Omega} w \rho \, d\Omega + \iint_{\Gamma} w \sigma \, dS \,, \forall w \in H_0^1(\Omega) \,, \tag{2.58}$$

here, σ is the surface charge density on interface. The second term on the right hand side of equation (2.58) is used to handle the charge on interface and the charge is not deposited to the mesh nodes for providing the charge density. Thus, the right hand side of Poisson's equation is zero. The Laplace equation (2.55) is used to solve the problem. If we use the homogeneous IFE method in reference [6, 26] in which the weak formulation is

$$\iiint_{\Omega} \varepsilon \nabla w . \nabla \Phi \, d\Omega = \iiint_{\Omega} w \rho \, d\Omega \,, \forall w \in H_0^1(\Omega) \,, \tag{2.59}$$

there is no term to consider the effect of charge on interface when solving the Laplace equation. If the interface charges are deposited to the mesh nodes, the Poisson's equation (2.60) should be solved:

$$-\nabla \bullet (\varepsilon \nabla \Phi) = \rho \,. \tag{2.60}$$

Figure 2.14 shows the error contour of potential Φ on z=0 plane with partition size h=1/50 when solving Poisson's equation using this method. The maximum error in the domain is 0.103053 which is 8.17% of the exact solution (1.2606332). This method has larger error when it is applied to solve for the potential with charges on interface which is in fact a non-homogeneous interface problem. The non-homogeneous IFE method is needed.

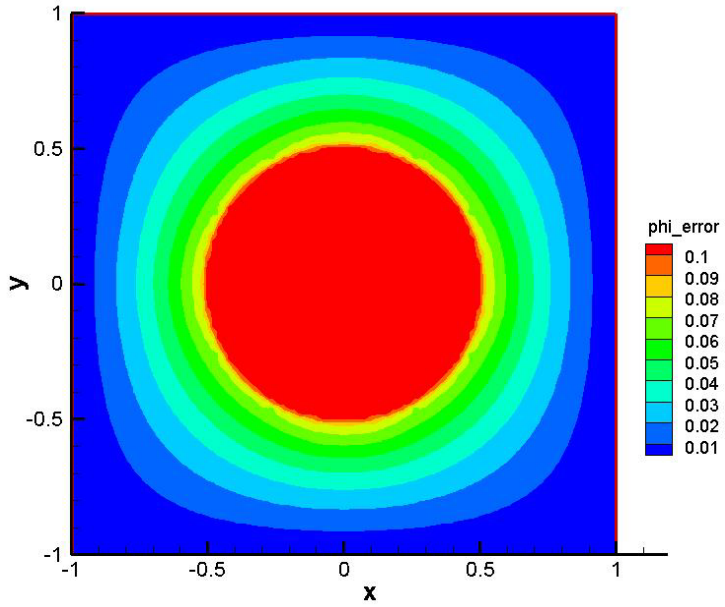

Figure 2.14 Error contour on z=0 plane
for conductive sphere with uniform surface charge
using homogeneous IFE method

2.7 Conclusion

In this chapter, we developed the IFE functions that can be used to solve the interface boundary problems with non-zero flux jump condition. The IFE functions can be used without considering the location of interface. Numerical tests show that the developed Galerkin methods based on these new IFE functions can approximate the functions in solution domain with optimal convergence for small discontinuous coefficient ratios. Some physical applications are presented and show that this IFE method can solve the electric field well.

Chapter 3

Immersed Finite Element and Particle-In-Cell Method

3.1 Introduction

This chapter applies the three-dimensional immersed finite element (IFE) method together with the Particle-In-Cell simulation model to solve the electric field and potential of the objects and space in which the plasma exists. We first present governing equations and normalization of the plasma simulation in this dissertation. Then the IFE-PIC simulation method is introduced incorporating the Particle-In-Cell method and three-dimensional non-homogeneous IFE field solver developed in Chapter 2. This work starts from Kafafy's work about IFE-PIC method in reference [6] to present a brief idea of this model. Some improvements made for IFE-PIC are also included.

3.2 Governing Equations

3.2.1 Dynamics of Plasma

For a collisionless, unmagnetized plasma with only electrostatic field, the trajectory of each particle is determined by Newton's second law:

$$\mathbf{F} = q\mathbf{E} = m\frac{d\mathbf{v}}{dt}, \tag{3.1}$$

$$\mathbf{v} = \frac{d\mathbf{x}}{dt}, \tag{3.2}$$

where **F** is the electrostatic force on electron, **E** is the local electrostatic field, **v** is the electron velocity and **x** is its position.

3.2.2 Electrostatic Field

The electrostatic field in the simulation domain is solved from the Poisson's equation

$$-\nabla \cdot (\varepsilon \nabla \Phi) = \rho, \tag{3.3}$$

$$\mathbf{E} = -\nabla \Phi. \tag{3.4}$$

The space charge density is the sum of the charge carried by plasma species.

3.2.3 Normalizations

The governing equations in plasma simulation are normalized to avoid round-off errors from calculating too large or too small numerical values. Some reference parameters are chosen to make normalization. In a full particle simulation model, normalization is mostly based on electron parameters.

The Debye length is

$$\lambda_D = \sqrt{\frac{\varepsilon_0 k T_e}{n_e e^2}}, \tag{3.5}$$

Here, T_e is the electron temperature; n_e is the electron number density. It can be written as $\lambda_D=7430(T_e/n_e)^{1/2}$ if we use T_e with unit eV and n_e in unit $1/m^3$.

The thermal velocity is given by the electron temperature T_e and the mass m_e

$$v_{th} = \sqrt{\frac{T_e}{m_e}}. \tag{3.6}$$

The electron frequency is

$$\omega_{pe} = \sqrt{\frac{4\pi n_e e^2}{m_e}}. \tag{3.7}$$

The reference variables are chosen as

$$q_{ref} = e,\ \ m_{ref} = m_e,\ \ T_{ref} = T_e,\ \ \varepsilon_{ref} = \varepsilon_0,\ \ n_{ref} = n_e,\ \ v_{ref} = v_{th}$$

The normalized values are

$$\hat{n} = \frac{n}{n_{ref}},\ \ \hat{q} = \frac{q}{q_{ref}},\ \ \hat{\rho} = \frac{\rho}{e n_{ref}},\ \ \hat{m} = \frac{m}{m_{ref}},\ \ \hat{x} = \frac{x}{\lambda_D},$$

$$\hat{v} = \frac{v}{v_{ref}},\ \ \hat{j} = \frac{j}{e n \lambda_D \omega_{pe}},\ \ \hat{\Phi} = \frac{e\Phi}{kT_e},\ \ \hat{t} = t\omega_{pe}$$

After normalization, the governing equations becomes

$$\hat{\mathbf{F}} = \hat{q}\hat{\mathbf{E}} = \hat{m}\frac{d\hat{\mathbf{v}}}{d\hat{t}}, \tag{3.8}$$

$$\hat{\mathbf{v}} = \frac{d\hat{\mathbf{x}}}{d\hat{t}}, \tag{3.9}$$

$$-\nabla\cdot(\hat{\varepsilon}\nabla\hat{\Phi}) = \hat{\rho}, \tag{3.10}$$

$$\hat{\mathbf{E}} = -\nabla\hat{\Phi}. \tag{3.11}$$

A PIC simulation uses macro-particles to represent real particles. If the number of macro-particles in a simulation domain with size $L_x \times L_y \times L_z$ is N_{part} and q_{part} is the charge carried by one macro-particle. The total charge carried by these N_{part} of macro-particles in the domain is $N_{part}q_{part}$. The real physical charge in the simulation domain is $n(L_xL_yL_z)e$, where n is the real particle number density. Each macro-particle carries a charge of

$$q_{part} = \frac{L_x L_y L_z}{N_{part}} ne . \tag{3.12}$$

The charged density contributed by the macro-particles is

$$\rho_{part} = \frac{N_x N_y N_z}{N_{part}} ne , \tag{3.13}$$

here N_x, N_y, N_z are numbers of macro-particle distributed in each dimension. After depositing the particle charge to the mesh nodes, the numerical value at each mesh point is in the unit of ρ_{part}.

3.3 The IFE-PIC Model

The steps of particle motion simulation using PIC model for each time step are [6]:

1. *Particle Push*: integration of the motion equation which is given by Newton's second law in each time step. The particle velocity and position are updated.
2. *Charge Deposit*: the charge of simulation particles are interpolated into the surrounding eight vertices of the cell in which this particle locates. This step provides the space charge density at the discrete field mesh points.
3. *Field Solve*: the electric field is solved by using the Poisson's equation and the charge density obtained in step 2, as well as the imposed boundary conditions.
4. *Force Weighting*: the electric field solved on each mesh nodes is interpolated to the particle positions and the electric force on the simulation particle is calculated to push the particle.

These steps of PIC simulation are shown in Figure 1.2.

The immersed finite element (IFE) method uses a structured Cartesian mesh to solve the electric field in step 3. The space charge density is known on each mesh node by depositing simulation particle charge. The mesh nodes of the PIC code and the IFE solver are collocated to make the charge density on PIC mesh nodes copied onto IFE mesh nodes. There is another PIC and IFE mesh coupling method called "hybrid-grid" which allows the IFE and PIC mesh nodes to be displaced from each other instead of being collocated according to the physical and computational needs of the problem.

By determining the location of each particle with respect to the PIC mesh, we can deposit the particle quantities to the PIC mesh nodes using a typical linear weighting function of a standard PIC code. These quantities can then be interpolated to the IFE mesh through linear interpolation. After solving Poisson's equation, the physical quantities obtained on the IFE mesh can then be interpolated into the PIC mesh through the finite element basis functions constructed on the IFE mesh.

3.4 Three-dimensional Immersed Finite Element Solver

In this section, we will discuss the computational aspect of the three-dimensional IFE method in solving electrostatic field problem. The mesh generation and object-mesh intersection scheme is introduced and then the detail of constructing the IFE system is given.

3.4.1 Mesh Generation

As mentioned in last chapter, IFE solver chooses a Cartesian-based tetrahedral mesh because of the simplicity in classifying the intersection types of object surface and mesh element, as well as the efficiency in determining the location of particles in the plasma simulation. This tetrahedral mesh is constructed by first generating the base Cartesian mesh. Then, each cell in this Cartesian mesh is further partitioned into five tetrahedra, shown in Figure 3.1. This makes the mesh generation trivial and fast [6].

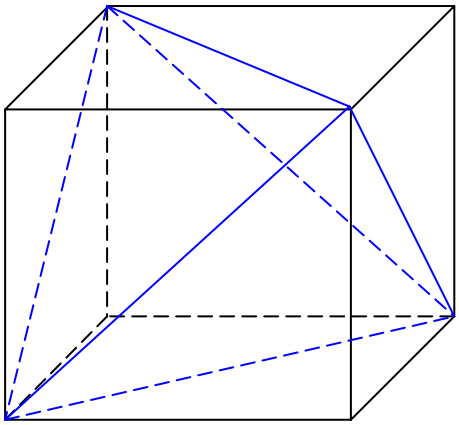

Figure 3.1 Five tetrahedral elements comprising the Cartesian cell

Typically an object surface will intersect with an interface tetrahedron in either three or four distinct points. This gives the type of the interface element as three-edge cut or four-edge cut. These intersection points are normally not on the same face or edge of the tetrahedron for a sufficiently fine mesh. The interface tetrahedra are classified according to intersection points. Using an index to classify the intersection topology, let *eind* be an edge intersection index which is defined as [6]

$$eind = \begin{cases} 1, & \text{if the intersection point lies between the edge ends} \\ -1, & \text{if the intersection point lies at one of the ends} \end{cases}.$$

The conditions in this definition are satisfied within a preset geometric tolerance and only one intersection point is considered on each edge. A tetrahedron intersection index on all six edges is defined as

$$tind = \sum_{j=1}^{6} eind_j \,. \tag{3.14}$$

Using this index *tind*, the special intersection situations are classified as the Figure 3.2 shows according to the Table 3.1

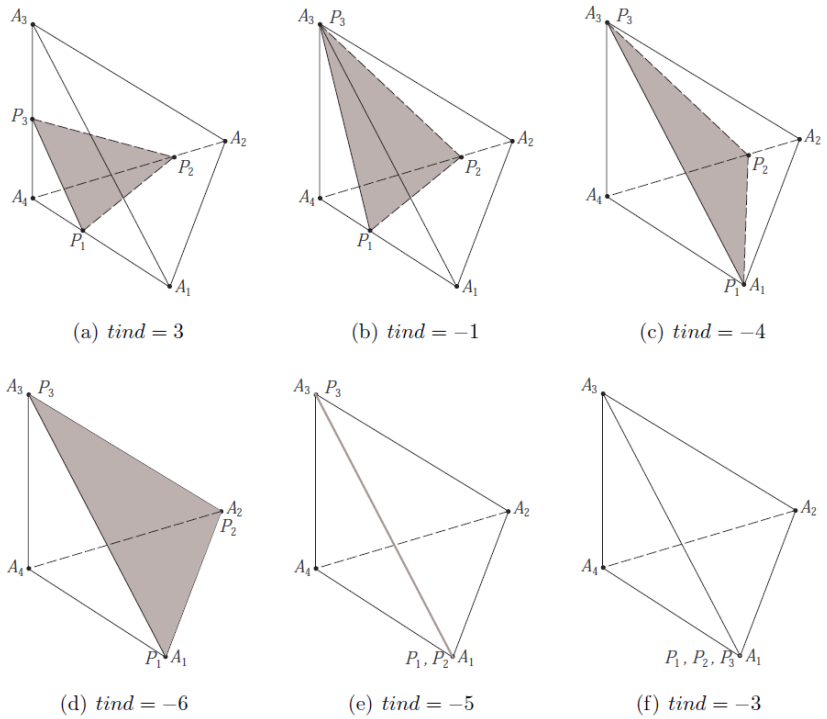

Figure 3.2 Special situations of three-edge cut tetrahedron [6]

Table 3.1 Rules for classification of intersection topologies [6]

tind	Classification of intersection topology
4	four-edge cut
3	three-edge cut
-1	three-edge cut
-4	three-edge cut
-6	non-interface
-5	non-interface
-3	non-interface

3.4.2 Assembly of the IFE System

The IFE functions developed in chapter 2 are used in the IFE method with non-homogeneous interface problem with non-zero flux jump condition. Inside the IFE solver, the stiffness matrix, K, and the right hand side (RHS) vector, F, are assembled. The stiffness matrix needs to be assembled only once and the RHS vector

matrix need to be assembled in each time step inside the field solution loop.

The finite element stiffness matrix and the RHS vector are all first assembled on each finite element. For the homogeneous interface problem, the local FE stiffness matrix is given by [6]

$$K_{ij}^{e} = \iiint_{\Omega_e} \varepsilon \nabla \varphi_i \cdot \nabla \varphi_j \, d\Omega, \tag{3.15}$$

where Ω_e is in the local element T and the local right hand side vector is given by [6]

$$F_i^e = \iiint_{\Omega_e} \varphi_i \, \rho \, d\Omega. \tag{3.16}$$

For the non-homogeneous IFE solver, we developed the local right hand side vector for interface elements and non-interface elements separately. For non-interface elements, this vector is the same as that in the homogeneous interface problem which is shown in equation (3.16). For non-interface elements,

$$F_i^e = \iiint_{\Omega_e} \varphi_i \, \rho \, d\Omega - \iint_{\Gamma_e} \varphi_i \, Q \, dS - q_T \left(\iiint_{\Omega_e} \varepsilon \nabla \varphi_i \cdot \nabla \varphi_{T,J} \, d\Omega \right), \tag{3.17}$$

where Γ_e is the interface in the local element T, Q is the derivative jump on Γ_e . q_T is the average value of flux jump as defined in equation (2.38). $\varphi_{T,J}$ is the IFE function with unit flux jump in local element T.

Assembling the local matrices and vectors of every element to their corresponding positions in the global stiffness matrix and the right hand side vector, we can get the global matrices and vectors. The global stiffness matrix is

$$K_{ij} = \sum_{e=1}^{NOE} K_{ij}^{e} \, . \tag{3.18}$$

NOE is the number of finite elements. The global right hand side vector is

$$F_i = \sum_{e=1}^{NOE} F_i^e \, . \tag{3.19}$$

Using the definition of the global linear basis functions for both interface and non-interface elements, the potential function can be approximated in the domain Ω by

$$\Phi(\mathbf{x})=\sum_{j=1}^{NON}\Phi(\mathbf{x}_j)\phi_j(\mathbf{x})+\sum_{j=1}^{NOB}g(\mathbf{x}_j)\phi_j(\mathbf{x})+\sum_{k=1}^{NOI}q_{T,k}\phi_{T,J}(\mathbf{x})\,. \tag{2.49}$$

Here *NON* is the number of nodes in Ω. $\Phi(\mathbf{x}_j)$ is the value of the potential at node $\mathbf{x}_j$. *NOB* is the number of boundary nodes. $g(\mathbf{x})$ is given as boundary condition. *NOI* is the number of interface elements and $q_{T,k}$ is the average flux jump in the k^{th} interface element.

We can get the system of algebraic equations

$$K_{ij}\Phi_j = F_i\,, \tag{3.20}$$

where

$$K_{ij} = \sum_{T\in\mathcal{T}_h}\iiint_T \varepsilon\nabla\phi_i.\nabla\phi_j\,d\Omega\,, \tag{3.21}$$

$$\begin{aligned} F_i = {} & \iiint_\Omega \phi_i\,\rho\,d\Omega - \iint_\Gamma \phi_i Q\,dS - \sum_{j=1}^{NOB}\left(\sum_{T\in\mathcal{T}_h}\iiint_T \varepsilon\nabla\phi_i.\nabla\phi_j\,d\Omega\right)g(\mathbf{x}_j) \\ & -\sum_{k=1}^{NOI} q_{T,k}\left(\iiint_T \varepsilon\nabla\phi_i.\nabla\phi_{T,J}\,d\Omega\right) \end{aligned}\,. \tag{3.22}$$

$$i = 1, 2, \ldots, NON$$

3.5 The Particle-In-Cell Model

In this section, we will present the methods used for particle push, charge deposit and force weighting in the PIC code used in this dissertation.

3.5.1 Particle Push

In a standard, Cartesian mesh based PIC code, the particle trajectories are integrated from equation (3.1) and (3.2) using the leap-frog scheme

$$m\frac{\mathbf{v}^{n+1/2}-\mathbf{v}^{n-1/2}}{\Delta t}=\mathbf{F}^{n}, \tag{3.23}$$

$$\frac{\mathbf{x}^{n+1}-\mathbf{x}^{n}}{\Delta t}=\mathbf{v}^{n+1/2}. \tag{3.24}$$

This scheme has a second order accurate and has a numerical error vanishes as $\Delta t \to 0$ [73]. After this "Particle Push" process, the velocity and position of each particle are updated. In this dissertation, this standard leap frog scheme is used to push particles.

3.5.2 Charge Deposit

The space charge carried by the particles need to be deposited to the mesh points for field solve. In a Cartesian mesh based PIC code, each particle has a rectangular parallelepiped shape with the same dimensions and orientation as a PIC mesh cell. As the particle moves inside a PIC cell, its total charge is assigned to the eight surrounding vertices of that cell. The portion of the total particle charge which is assigned to a certain cell vertex is proportional to the volume of the rectangular parallelepiped included between the opposite cell vertex and the particle position [6]. This is illustrated in Figure 3.3. In a three-dimensional domain, the contribution of the particle p, which is located at position $\mathbf{x}_p$, for instance, to the charge density at the node (i, j, k) is calculated from [6]

$$q_{i,j,k}=q_p\frac{V(\mathbf{x}_{i+1,j+1,k+1},\mathbf{x}_p)}{V(\mathbf{x}_{i,j,k},\mathbf{x}_{i+1,j+1,k+1})}. \tag{3.25}$$

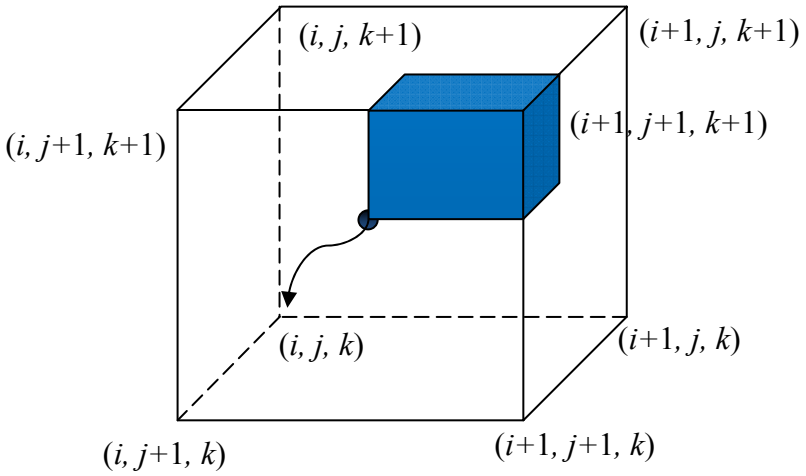

Figure 3.3 Deposition of particle charge in a three-dimensional simulation domain

This is the charge deposition method used in this dissertation. For those particles in interface cells, their charges are deposited on the nodes of the cell including those on the two sides of the interface. Therefore, the above charge deposition is no longer correct for charge deposit in interface cells. In this case one needs to consider the charge as having the shape as the tetrahedral element and use the IFE basis function in deposition. This dissertation still uses equation (3.25) even at interface cell, which may cause some error in the simulation.

3.5.3 Force Weighting

In a PIC model, the electrostatic forces are weighted from the calculated field values at mesh nodes to the arbitrary particles positions. The same weighting method as in the charged deposit step is adopted. This weighting method can greatly reduce the numerical noise associated [73].

The reference [6] used this weighting method for all the space charge including those particles in the cell which is partitioned by the object surface, as the three-dimensional situation that shown in Figure 3.3. In a three-dimensional domain, the contribution of $\mathbf{E}_{i,\,j,\,k}$ at node $(i,\,j,\,k)$ to electric field $\mathbf{E}_p$ of $\mathbf{x}_p$, where the particle p is located, is calculated from

$$\mathbf{E}_{p,i,j,k} = \mathbf{E}_{i,j,k} \frac{V(\mathbf{x}_{i+1,j+1,k+1}, \mathbf{x}_p)}{V(\mathbf{x}_{i,j,k}, \mathbf{x}_{i+1,j+1,k+1})}. \tag{3.26}$$

The total electric field $\mathbf{E}_p$ at $\mathbf{x}_p$ is given by

$$\mathbf{E}_p = \sum_{l=k}^{k+1} (\mathbf{E}_{p,i,j,l} + \mathbf{E}_{p,i+1,j,l} + \mathbf{E}_{p,i,j+1,l} + \mathbf{E}_{p,i+1,j+1,l}) . \tag{3.27}$$

Those components of electric field $\mathbf{E}_{i,j,k}$ at node (i, j, k) is given by the potential solution Φ on the neighboring PIC mesh nodes:

$$\mathbf{E}_{\mathrm{x},i,j,k} = \frac{\Phi_{i-1,j,k} - \Phi_{i+1,j,k}}{2h_x}, \tag{3.28}$$

$$\mathbf{E}_{\mathrm{y},i,j,k} = \frac{\Phi_{i,j-1,k} - \Phi_{i,j+1,k}}{2h_y}, \tag{3.29}$$

$$\mathbf{E}_{z,i,j,k} = \frac{\Phi_{i,j,k-1} - \Phi_{i,j,k+1}}{2h_z}, \tag{3.30}$$

where h_x, h_y, h_z are the PIC mesh size in x, y, z directions. However, for those PIC cells partitioned by object interface, the different properties of the parts on each side of interface affect the electric field in the cell. It is not precise enough to use equations (3.28) to (3.30) for getting the electric field components.

Considering the finite element solution gives the solution of potential and its derivative as a function in the space, the fields at particle positions can be given directly by the finite element solutions using interpolation functions. This dissertation developed the method to obtain the electric field on nodes of interface cells. The electric field on the nodes of the PIC cell partitioned by object interface or the nodes of the cells neighboring to the interface cell is given directly from the solution of electric field in IFE solver. For interface element, the **E** field is not obtained from the finite difference of the potential. Rather, we use directly the **E** field obtained for the tetrahedral element. For a particle in a tetrahedral interface element locating at position $\mathbf{x}_p$, the contribution of the charge deposited to the n^{th} vertex of the tetrahedral element is determined by

$$\mathbf{E}_p = -\sum_{i=1}^{4} \Phi(A_i) \frac{\partial \varphi_i(\mathbf{x}_p)}{\partial \mathbf{x}} .$$

where φ_i , i = 1, 2, 3, 4 are basis functions in the element and $\Phi(A_i)$, i = 1, 2, 3, 4 are potential on the tetrahedral element vertex A_i.

3.5.4 Field Solve

With the charge density on mesh nodes, we can solve the Poisson's equation (1.13) for the electric potential which may be numerically differentiated to obtain the electric field. The Poisson's equation is a partial differential equation and requires boundary condition information about the potential or potential gradient (negative electric field) over all domain boundaries. Many numerical techniques may be applied to solve this equation including finite difference and finite element method. The immersed finite element method is selected to solve the Poisson's equation in this dissertation so that the high accuracy and an affordable additional computational cost are presented when arbitrary shaped objects are immersed in a Cartesian mesh. The geometrical and physical nature of the simulation problem requires a three dimensional analysis of the problem. The Poisson's equation is solved using the IFE method described in Chapter 2.

3.5.5 Boundary Conditions at Interface

The particles boundary conditions at interface are especially important because the charge deposited is used to solve the surface potential. Those particles hitting the object surface are removed. These removed particles are no longer deposited to the PIC mesh nodes. However, for non-homogeneous interface IFE solver which considers the surface charge deposition, the index of the interface element to which the particle absorption position belongs is recorded. The surface charge density accumulated in this interface element provides the flux jump condition to the non-homogeneous IFE solver. The method to record the absorbed charge by interface is given by:

assume n is the total number of particles, *NOI* is the interface element number
initialized the absorbed charge on all interface elements
el_charge =0
for time step=1,2,….
  for i=1,2,…, n
    if the i^{th} particle is absorbed by object
      for e =1,2,…, *NOI*
        if the absorbed position belongs to the e^{th} interface element
          el_charge (e) = *el_charge* (e)+q_p
        end if
      end
    end if
    the i^{th} particle is removed
    $n = n$ - 1
  end
  get space charge deposited on PIC mesh nodes *rho_space*
end

In Chapter 2, we described the non-zero flux jump condition on interface. Here, the potential jump is zero on the object surface and the flux jump is a non-zero value which is determined by the surface charge density.

$$\left[\varepsilon \frac{\partial \Phi}{\partial \mathbf{n}} \right]\Big|_{\Gamma} = -(\varepsilon_2 \mathbf{E}_2 - \varepsilon_1 \mathbf{E}_1) \bullet \mathbf{n} = -\sigma . \tag{1.20}$$

This provides the jump condition for IFE solver which is used to solve the potential of non-homogeneous interface problem.

3.5.6 Boundary Conditions at Domain Surfaces

There are four kinds of boundary conditions for the particles on domain surface: absorption, reflection, periodic and emission. A particle hitting the outside domain boundary is absorbed. A particle hitting the symmetrical boundary surface is reflected back to the domain. For the boundary surface with emission condition, the particles are emitted from the domain boundary according to ambient distribution. For Maxwellian's distribution, the particles distribution function is expressed as

$$f(v)=\left(\frac{m}{2\pi kT}\right)^{3/2}\exp\left(-\frac{m(v-v_d)^2}{2kT}\right), \tag{3.31}$$

here, v_d is the drifting velocity of the plasma. If we use $v_{th}=(kT/m)^{1/2}$ and $v_r=v_d/v_{th}$, the plasma flux entering into the domain are given by

$$j=en\int_{-\infty}^{\infty}\int_{-\infty}^{\infty}\int_{0}^{\infty} v\,f(v)\,dv_z dv_y dv_x=\frac{1}{\sqrt{2}}envth\left(\frac{\exp\left(-v_r^2/2\right)}{\sqrt{\pi}}+\frac{v_r}{\sqrt{2}}\left(1+erf\left(v_r/\sqrt{2}\right)\right)\right).$$

There are two conditions of potential on the domain boundary: Dirichlet and Neumann boundary conditions. For an open surface which is out of the plasma sheath, we use the Dirichlet boundary condition where the boundary potential is fixed. For symmetric surfaces, the Neumann boundary condition is applied to make the derivative of potential to be zero.

3.6 Conclusion

In this chapter, we developed the three-dimensional IFE-PIC model to solve the potential and electrostatic field of objects and space in plasma environment. The governing equations are solved using normalized parameters in PIC simulation. The continuous real physical space is dispersed on the mesh nodes to be solved using computational methods. In a typical PIC simulation process, there are four steps in a cycle of each time loop. The treatments of standard PIC method based on finite difference method, the one based on finite element method and that used in this dissertation are compared for each step in one typical loop. The particle and field boundary conditions are separately introduced on the object surface and domain surfaces.

Chapter 4

Modeling Charging of Spherical Objects in OML Regime

4.1 Introduction

In this chapter, we apply the IFE-PIC method on solving charging problems of object in plasma. First, we studied the charging process of single spherical object with conductive and dielectric material in stationary and flowing plasma. The conductive object is simulated with fixed potential and the homogeneous IFE method is used. For the dielectric object, the surface charge deposition is considered and the non-homogeneous IFE method is used to handle the non-zero flux jump condition caused by the surface charge. The simulation results are compared with the analytical solution using orbital motion limited (OML) theory. For multiple dusts coupled together in dusty plasma, the effect of neighboring dusts is significant for dust charging. The IFE-PIC method is used to solve the problem of four and five spheres cluster in stationary plasma. The simulation results are compared with the single sphere charging.

4.2 Simulation of Single Spherical Object in Plasma

In this section, we apply the IFE-PIC model to simulate the single spherical object in stationary and flowing plasma. In an object-plasma interaction problem, there are two features present. First, based on the boundary condition on the interface, the conductive object achieves an equipotential on the object and the dielectric object may have non-uniform potential. Second, the plasma particles hitting the object are removed and redistributed on the object surface. For a perfectly conductive spherical object, the object surface has equipotential and the deposited charges are distributed on the object surface such that the surface potential is a constant. For a dielectric object, the particles are captured on the position where they hit the object surface. The distribution of the deposited charge is determined by the geometry and plasma conditions, and the charge may be non-uniformly distributed. The simulation of object-plasma interaction needs to couple these features together self-consistently. In the simulations of this section, the conductive object has fixed potential which represents the equipotential and particles absorbed by it are simply removed. In this condition, there is no deposited charge on sphere surface and the flux jump is zero. The homogeneous IFE solver is applied. For dielectric material objects, the absorbed particles are deposited on the object surface at the location where they hit the object. A non-zero flux jump condition for non-homogeneous IFE solver is applied in this case. We are considering four cases including single conductive and dielectric spherical object in stationary or flowing plasma. The cases of the object and plasma conditions are listed in Table 4.1. In these simulations, the object radius is much smaller than the Debye length, $a \ll \lambda_D$, so that the orbital motion limited (OML) theory is used to compare with the simulation results.

Table 4.1 Simulation conditions for single spherical object

Cases	Object Material	Plasma Drifting Condition
1	Conductive	Stationary
2	Conductive	Flowing
3	Dielectric	Stationary
4	Dielectric	Flowing

4.3 Modeling OML Current Collection by a Conductive Sphere

4.3.1 Conductive Spherical Object in Stationary Plasma

Consider a spherical object in a thick sheath plasma which satisfies the condition that the object radius a is much smaller than the Debye length of the plasma $\lambda_D \gg a$. In this special and simple case, the object potential is low and an analytical solution is trivial. This case is chosen to compare with the analytical solution under orbital motion limited (OML) theory.

The species reaching the spherical object surface are attracted or repelled based on the charge of the species and the object potential. With the OML theory, the current densities of the attracted and repelled species, $j_{attracted}$ and $j_{repelled}$ are given by

$$j_{attracted} = j_{0attracted}(1+Q), \tag{4.1}$$

$$j_{repelled} = j_{0repelled}\exp(Q), \tag{4.2}$$

where $Q = -q\Phi_s/kT$, and Φ_s is the potential of charging object. These current densities are approximated under the condition that Q is not large. Those particles whose charge has the same sign as potential will be repelled and those with opposite charge are attracted. The parameter Q satisfies $Q > 0$ for the attracted species and $Q < 0$ for the repelled species. j_0 is the ambient current density outside the sheath given by $j_0 = en\langle v\rangle/4$. Here, $\langle v\rangle$ is the mean velocity of each species as $\langle v\rangle = (8kT/\pi m)^{1/2}$. Thus, the attracted and repelled current becomes

$$j_{attracted} = \frac{n_a q}{4}\sqrt{\frac{8kT_a}{\pi m_a}}\left(1-\frac{q\Phi_s}{kT_a}\right), \tag{4.3}$$

$$j_{repelled} = \frac{n_r q}{4}\sqrt{\frac{8kT_r}{\pi m_r}}\exp\left(-\frac{q\Phi_s}{kT_r}\right). \tag{4.4}$$

The above equation for the attracted species is valid only for low surface potential $q\Phi_s/kT_a \leq 1$. For an object immersed in plasma with the electrons and ions having thermal velocity $v_{th,e}$ and $v_{th,i}$, if the object potential is positive, the electrons and ions

are separately attracted and repelled. Then the current density for electron and ions, j_e, j_i satisfies

$$j_e = j_{0e}\left(1+\left|\frac{e\Phi_s}{kT_e}\right|\right),\quad j_i = j_{0i}\exp\left(-\left|\frac{q\Phi_s}{kT_i}\right|\right). \tag{4.5}$$

The total current density reaching the object surface is

$$j = j_{0i}\exp\left(-\left|\frac{q\Phi_s}{kT_i}\right|\right) - j_{0e}\left(1+\left|\frac{e\Phi_s}{kT_e}\right|\right), \tag{4.6}$$

where, $j_{0i} = qn_i\sqrt{\frac{kT_i}{2\pi m_i}}$, $j_{0e} = en_e\sqrt{\frac{kT_e}{2\pi m_e}}$.

If the object potential is negative, the electrons become the repelled species and ions are attracted. The current density of electrons and ions are

$$j_e = j_{0e}\exp\left(-\left|\frac{e\Phi_s}{kT_e}\right|\right),\quad j_i = j_{0i}\left(1+\left|\frac{q\Phi_s}{kT_i}\right|\right). \tag{4.7}$$

The total current density is

$$j = j_{0i}\left(1+\left|\frac{q\Phi_s}{kT_i}\right|\right) - j_{0e}\exp\left(-\left|\frac{e\Phi_s}{kT_e}\right|\right). \tag{4.8}$$

With the definition of $v_{th,e} = (kT_e/m_e)^{1/2}$ and $v_{th,i} = (kT_i/m_i)^{1/2}$, these current densities after normalization are listed in Table 4.2.

Table 4.2 Current density of conductive spherical object in stationary plasma under OML Theory

Conditions	$\hat{\Phi}_s > 0$	$\hat{\Phi}_s < 0$
Ion current Density $\hat{j}_i$	$\frac{1}{\sqrt{2\pi}}\hat{q}_i\hat{n}_i\hat{v}_{th,i}\exp\left(-\hat{\Phi}_s\right)$	$\frac{1}{\sqrt{2\pi}}\hat{q}_i\hat{n}_i\hat{v}_{th,i}\left(1-\hat{\Phi}_s\right)$
Electron current Density $\hat{j}_e$	$-\frac{1}{\sqrt{2\pi}}\hat{q}_e\hat{n}_e\hat{v}_{th,e}\left(1+\hat{\Phi}_s\right)$	$-\frac{1}{\sqrt{2\pi}}\hat{q}_e\hat{n}_e\hat{v}_{th,e}\exp\left(\hat{\Phi}_s\right)$
Total current Density $\hat{j}_i+\hat{j}_e$	$\frac{1}{\sqrt{2\pi}}\hat{q}_i\hat{n}_i\hat{v}_{th,i}\exp\left(-\hat{\Phi}_s\right)$ $-\frac{1}{\sqrt{2\pi}}\hat{q}_e\hat{n}_e\hat{v}_{th,e}\left(1+\hat{\Phi}_s\right)$	$\frac{1}{\sqrt{2\pi}}\hat{q}_i\hat{n}_i\hat{v}_{th,i}\left(1-\hat{\Phi}_s\right)$ $-\frac{1}{\sqrt{2\pi}}\hat{q}_e\hat{n}_e\hat{v}_{th,e}\exp\left(\hat{\Phi}_s\right)$

We apply the IFE-PIC model developed previously to simulate the conductive spherical object in a stationary plasma with different fixed potential. The current densities for both species are compared with the analytical solution. In this case, the object potential is fixed so that the effect on the potential made by the deposited surface charged is not considered.

We use dimensionless parameters after normalization in the simulation. The spherical object with radius a/λ_D=0.018 is located in the center of the domain. The simulation domain is (0.6 λ_D×0.6 λ_D×0.6 λ_D). We find this domain is sufficiently large for this problem as the plasma amount is stable in the system. A uniform mesh is used with mesh cell size h/λ_D=0.005, as that shown in Figure 4.1. Thus, the domain boundary can be considered far enough from the object and has potential equal to zero. Dirichlet boundary conditions (Φ=0) are applied for all domain faces. Plasma consisting of electrons and ions is distributed in the domain and in each following time step neutral plasma is emitted from the domain boundary faces with initially stationary Maxwellian distribution. The dimensionless plasma conditions for both electrons and ions are listed in Table 4.3.

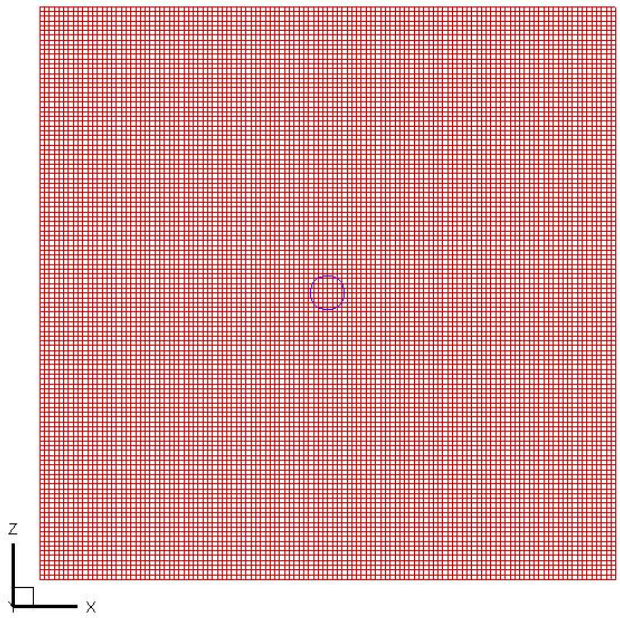

Figure 4.1 Mesh used in the simulation
of conductive sphere in stationary plasma

Table 4.3 Conditions of conductive spherical object in stationary plasma
(after normalization)

Species	Number density $\hat{n}$	Temperature $\hat{T}$	Mass $\hat{m}$	Thermal velocity $\hat{v}_{th}$	Flowing velocity $\hat{v}_d$
Electrons	1	1	1	1	0
Ions	1	1	1836	0.0233	0

The simulation particles are used to replace the electrons and ions with certain numbers in each cell which makes sure the noise is small enough to simulate the ambient plasma. The simulation time step is also small enough to make the particles motion distance less than half of the cell size. Those particles hitting the domain boundaries are removed from the simulation system. The particle number for both species collected by the spherical object is count at steady state to get the current density.

By fixing the object potential to be -2, we can get the potential and charge density in the domain. Figure 4.2 shows the profiles of potential, total charge density and the density for each species at steady state on the slice across the center of sphere. The electron and ion current densities are separately -0.0208 and 0.0215 at steady state and total current density is 0.0007. For different fixed object potential, current densities of both species are related to the object potential according to equations in Table 4.2. The analytical and simulation current densities for a series of object

potential are shown in Figure 4.3. The analytical and numerical solution curves are in good agreement, especially for the attracted species, the positive phi segment in Figure 4.3(a) and negative phi segment in Figure 4.3(b). The IFE-PIC model can simulate the conductive object with fixed potential immersed in stationary plasma with reasonable accuracy. The simulation error of charging current is listed in Table 4.4. The error is smaller if the potential is not large.

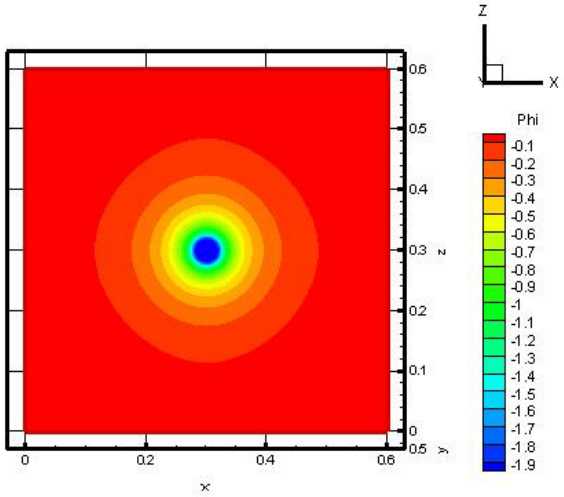

(a)

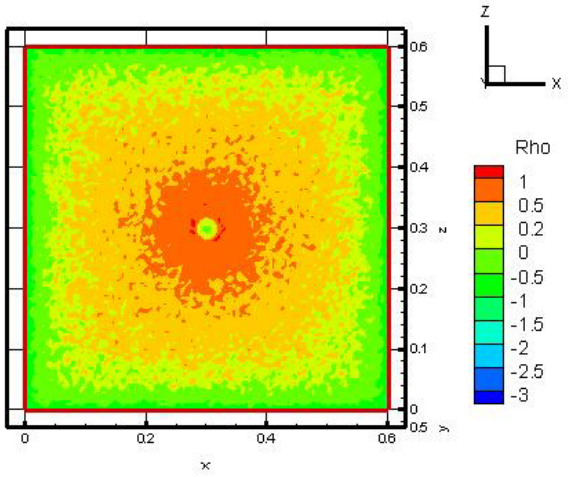

(b)

Figure 4.2 Potential and charge density profile
on the slice across the sphere center (y=0.3)
(a) Potential; (b) Total charge density

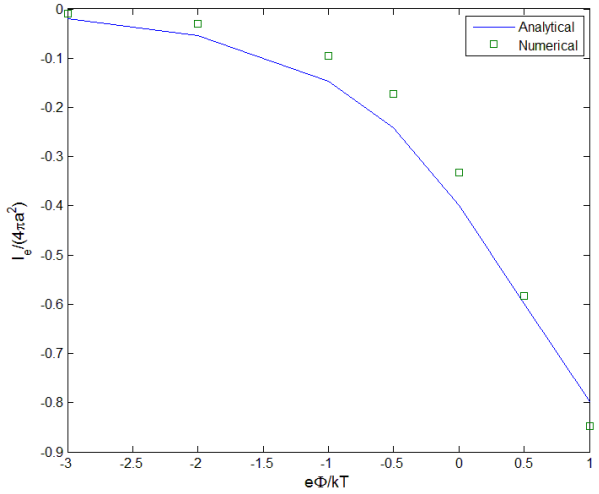

(a)

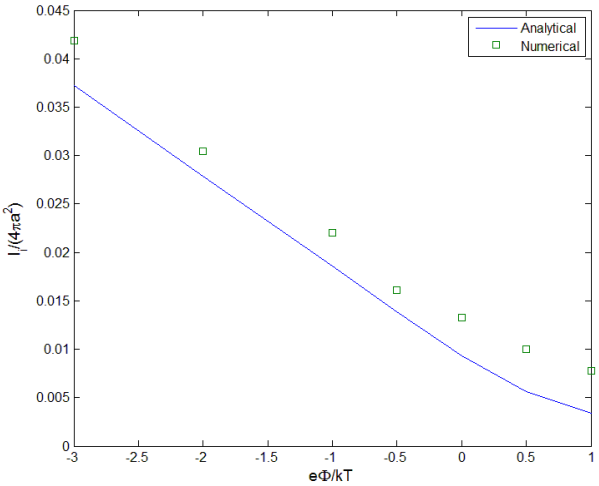

(b)

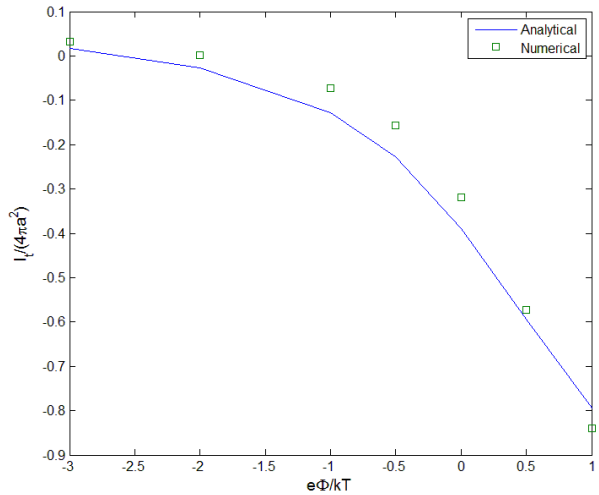

(c)

Figure 4.3 Current density of analytical and numerical solutions
for conductive spherical object in stationary plasma
(a) Electron current density; (b) Ion current density; (c) Total current density

Table 4.4 Simulation error of charging current
for conductive sphere in stationary plasma

Sphere Potential	Electron Current Error	Ion Current Error	Total Current Error
-3	52.26%	1.61%	63.58%
-2	45.19%	1.08%	92.34%
-1	35.15%	18.82%	42.98%
-0.5	28.06%	15.83%	30.73%
0	16.47%	43.01%	17.89%
0.5	2.12%	80.36%	2.90%
1	6.64%	126.47%	6.13%

4.3.2 Conductive Spherical Object in Flowing Plasma

In this section, we will consider the general condition in which the plasma has finite flowing velocity. For mesothermal plasma, the flowing velocity u is much larger than the ions' thermal velocity and smaller than the electrons' thermal velocity, $v_{th,e} \gg u \gg v_{th,i}$. The ion current to a spherical object which has radius much smaller than the Debye length can be approximately described by (Whipple 1981, [4])

$$I_i = \pi a^2 n_i q u_i f(u_i), \tag{4.9}$$

where a is the radius of the spherical object and $f(u_i)$ is a complicated function of ion flowing velocity. This is an approximate expression which assumes the current collection is only by the cross sectional area of the sphere. For $v_{th,i} \gg u$, it can be reduced to [45]

$$I_i = \pi a^2 n_i q u_i \left(1 - \frac{2e\Phi_s}{m_i u_i^2}\right). \tag{4.10}$$

Thus, for a negatively charged sphere, the current density of ion current is

$$j_i = \frac{n_i q u_i}{4} \left(1 - \frac{2e\Phi_s}{m_i u_i^2}\right). \tag{4.11}$$

The current density of electrons without flowing velocity is

$$j_e = en_e\sqrt{\frac{kT_e}{2\pi m_e}}\exp\left(-\left|\frac{e\Phi_s}{kT_e}\right|\right). \tag{4.12}$$

The total current density is

$$j = \frac{n_i q u_i}{4}\left(1-\frac{2e\Phi_s}{m_i u_i^2}\right) - en_e\sqrt{\frac{kT_e}{2\pi m_e}}\exp\left(\frac{e\Phi_s}{kT_e}\right). \tag{4.13}$$

With the definition of $v_{th,e}=(kT_e/m_e)^{1/2}$ and $v_{th,i}=(kT_i/m_i)^{1/2}$, these current densities after normalization are listed in Table 4.5.

Table 4.5 Current density of conductive spherical object in flowing plasma under OML theory

Conditions	$\hat{\Phi}_s < 0$
Ion current Density $\hat{j}_i$	$\frac{\hat{q}_i\hat{n}_i\hat{u}}{4}\left(1-\frac{2\hat{\Phi}_s}{\hat{m}_i\hat{u}^2}\right)$
Electron current Density $\hat{j}_e$	$-\frac{1}{\sqrt{2\pi}}\hat{q}_e\hat{n}_e\hat{v}_{th,e}\exp\left(\hat{\Phi}_s\right)$
Total current Density $\hat{j}_i+\hat{j}_e$	$\frac{\hat{q}_i\hat{n}_i\hat{u}}{4}\left(1-\frac{2\hat{\Phi}_s}{\hat{m}_i\hat{u}^2}\right)-\frac{1}{\sqrt{2\pi}}\hat{q}_e\hat{n}_e\hat{v}_{th,e}\exp\left(\hat{\Phi}_s\right)$

Using the IFE-PIC model to simulate the spherical object with fixed potential in flowing plasma, we assume the sphere radius is a/λ_D=0.018 and the domain size is (0.45 λ_D×0.45 λ_D×0.8 λ_D) with uniform mesh h/λ_D=0.005, as that shown in Figure 4.4. The center of sphere locates at the point with coordinates (0.225 λ_D, 0.225 λ_D, 0.5 λ_D). The electrons and ions have number density and temperature as that in last section. However, there is a flowing velocity for both species. The dimensionless plasma conditions for both electrons and ions are listed in Table 4.6.

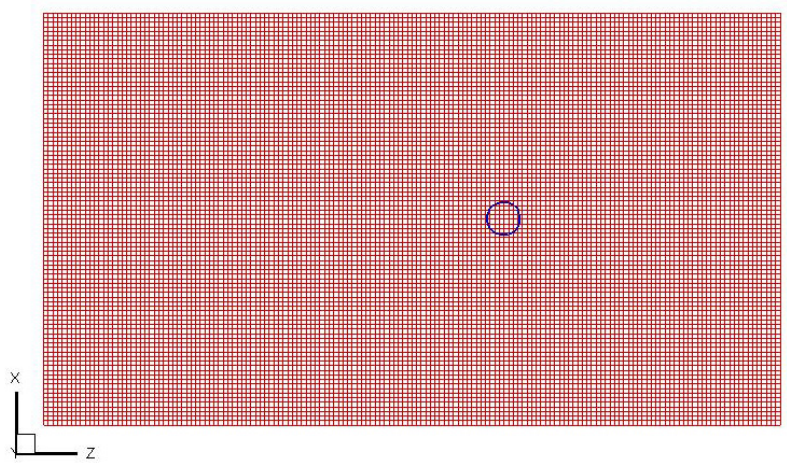

Figure 4.4 Mesh used in the simulation
of conductive sphere in flowing plasma

Table 4.6 Conditions of conductive spherical object in flowing plasma
(after normalization)

Species	Number density $\hat{n}$	Temperature $\hat{T}$	Mass $\hat{m}$	Thermal velocity $\hat{v}_{th}$	Flowing velocity $\hat{u}$
Electrons	1	1	1	1	0.3
Ions	1	1	1836	0.0233	0.3

Figure 4.5 shows the potential, charge density profile of the simulation results at steady state. There is a wake region behind the object where the ions are focusing. Analytical and simulation current densities for spherical object with a series of negative potential in flowing plasma are shown in Figure 4.6. The current density curves of simulation and analytical solution are closed to each other.

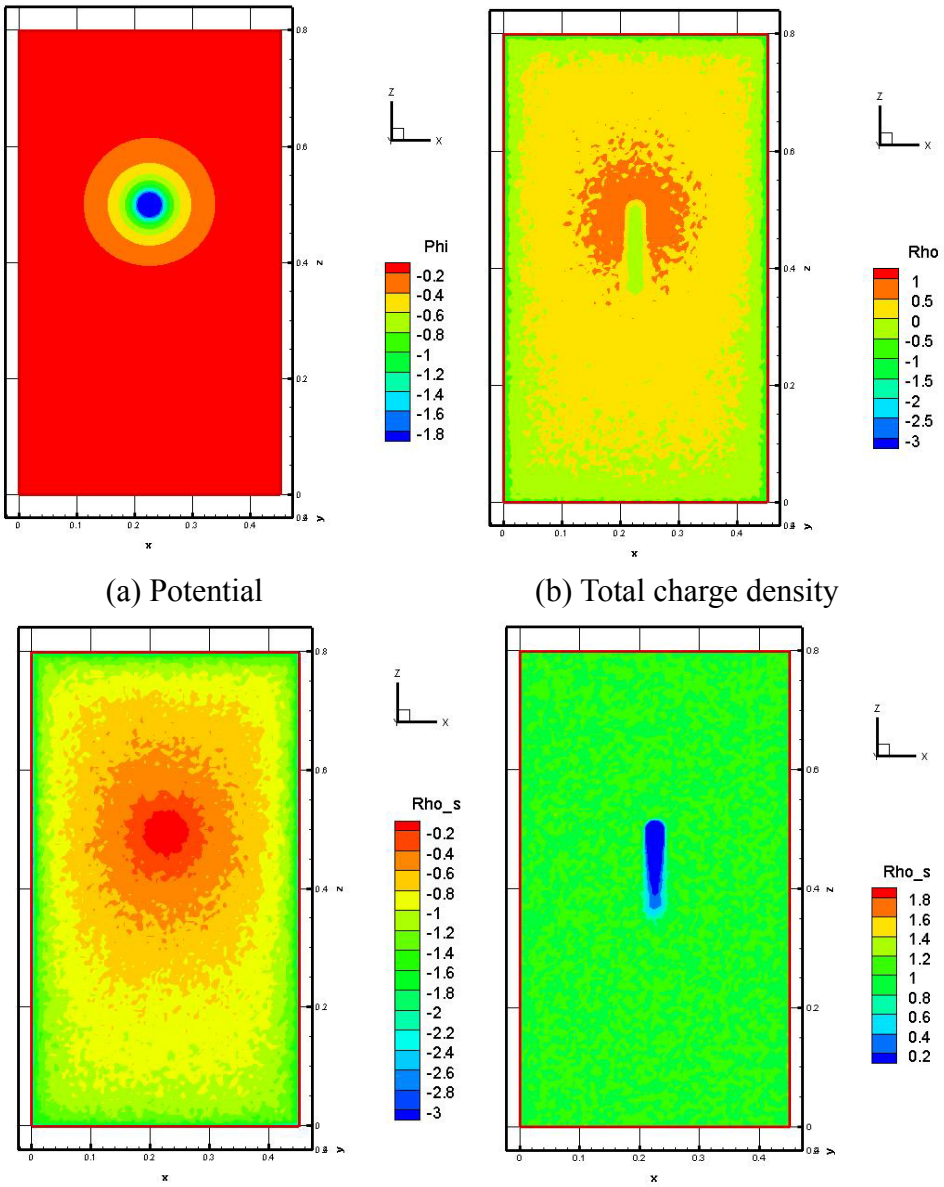

(a) Potential (b) Total charge density

(c) Electron charge density (d) Ion charge density

Figure 4.5 Potential and charge density profile of conductive sphere in flowing plasma (on the slice of y=0.225)

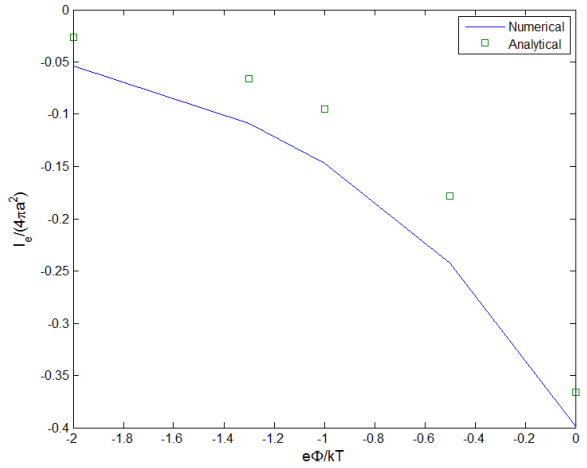

(a)

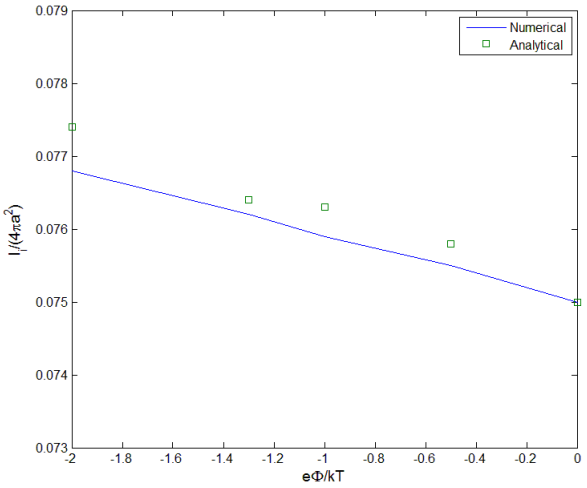

(b)

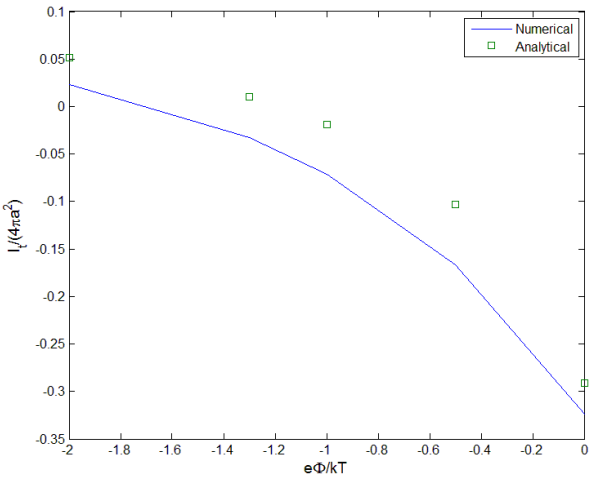

(c)

Figure 4.6 Current density of analytical and numerical solutions
for conductive spherical object in flowing plasma
(a) Electron current density; (b) Ion current density; (c) Total current density

4.4 Modeling Charging of Dielectric Sphere

4.4.1 Dielectric Spherical Object in Stationary Plasma

The cases in last sections consider the object with fixed potential and the particles absorbed by object are removed without deposition. Thus the homogeneous interface IFE solver is applied. For dielectric object, the charges are captured on the location where it is absorbed. The deposited charge on the interface requires proper boundary conditions applied to solve for electric field. This is the derivative flux jump condition introduced in Chapter 1 which can be expressed as

$$\left[\varepsilon\frac{\partial\Phi}{\partial\mathbf{n}}\right]\Big|_{\Gamma} = -(\varepsilon_2\mathbf{E}_2 - \varepsilon_1\mathbf{E}_1)\bullet\mathbf{n} = -\sigma\,. \tag{1.20}$$

Here, ε_1, ε_2 are separately the electric permittivity of object and vacuum, $\mathbf{n}$ is the unit normal vector from object to vacuum and σ is the surface charge density. This provides the non-zero derivative jump condition in non-homogeneous interface IFE solver.

In the simulation of dielectric spherical object in stationary plasma. The dimensionless plasma conditions for both electrons and ions are listed in Table 4.7. We consider the radius of object as $a/\lambda_D = 0.44$, where λ_D is the Debye length of the plasma. The electric permittivity of the sphere is $\varepsilon/\varepsilon_0=2$. The simulation is applied in the domain of $7\lambda_D \times 7\lambda_D \times 7\lambda_D$ which is large enough to make sure that the sheath of sphere is in the domain boundary and the particle amount in the system is stable. A uniform mesh is used with mesh size $h/\lambda_D = 0.2$. The spherical object locates at the origin point (0, 0, 0) which is one corner of the domain. In order to save the cost of computation, the PIC simulation is carried out with the one eighth sphere using the reflection boundary conditions for particles on x=0, y=0 and z=0 faces. Those particles hitting these faces are reflected back to the domain with reflection of the velocity on the surface. Figure 4.7 shows the mesh used in this simulation. There is no initial charge on the object and the potential of the object varies with the charge accumulation on object surface during charging process. The magnitude of initial electrons current density j_e is larger than that of the ions current density j_i, thus the object is negatively charged with negative potential. With the decreasing of the object potential, the magnitude of j_e decreases and the j_i increases, however, the total current density $j_i + j_e$ is still negative. At the steady state, the currents are balanced with $j_i + j_e = 0$ and the object is negatively charged.

Table 4.7 Conditions of dielectric spherical object in stationary plasma (after normalization)

Species	Number density $\hat{n}$	Temperature $\hat{T}$	Mass $\hat{m}$	Thermal velocity $\hat{v}_{th}$	Flowing velocity $\hat{u}$
Electrons	1	1	1	1	0
Ions	1	1	100	0.1	0

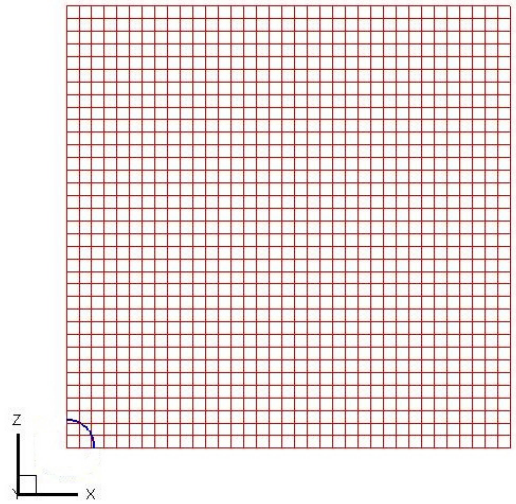

(a) PIC mesh

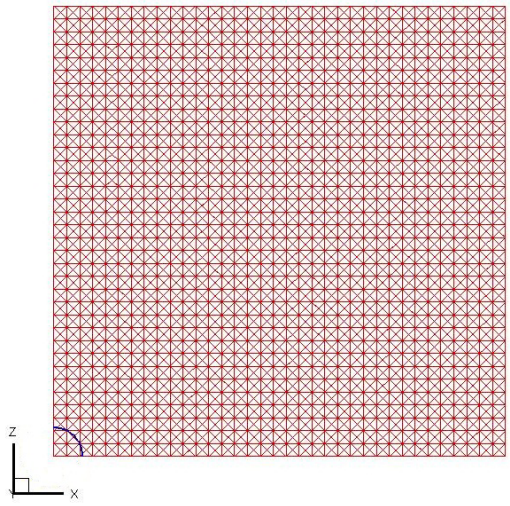

(b) IFE mesh

Figure 4.7 Mesh used in the simulation of dielectric sphere in stationary plasma

Figure 4.8 shows the potential, accumulated charges, charging current densities changing with time. The steady state is from about $t\omega_{pe}$=200 and the floating potential

at steady state is about $e\Phi/kT_e$= -1.2. The charge collected by sphere is -10.917 at steady state. Here we are using the electric permittivity of the sphere $\varepsilon/\varepsilon_0$=2. For $\varepsilon/\varepsilon_0$=4, the charge at steady state is -10.559 which is slightly smaller than the case with $\varepsilon/\varepsilon_0$=2. The accumulated charge on sphere changing with time is shown in Figure 4.9 for these two cases.

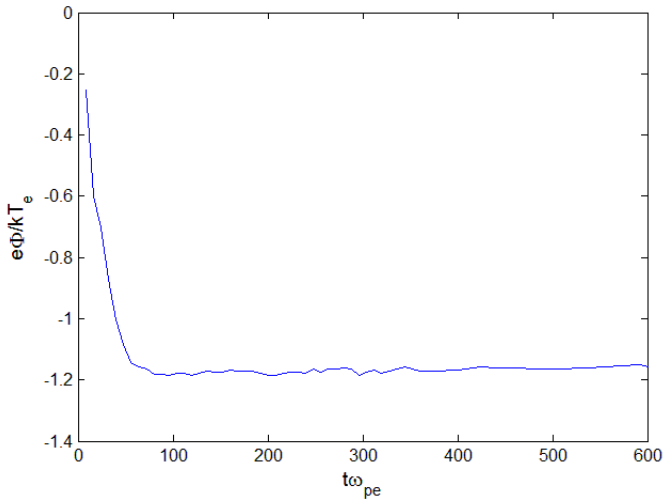

(a) Potential history

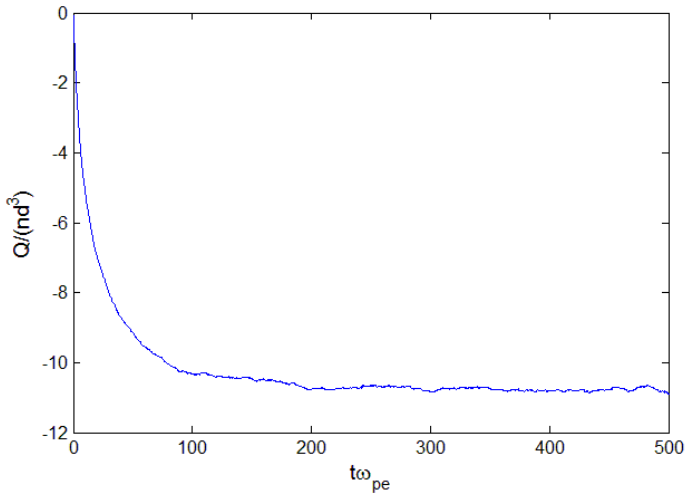

(b) Charge history

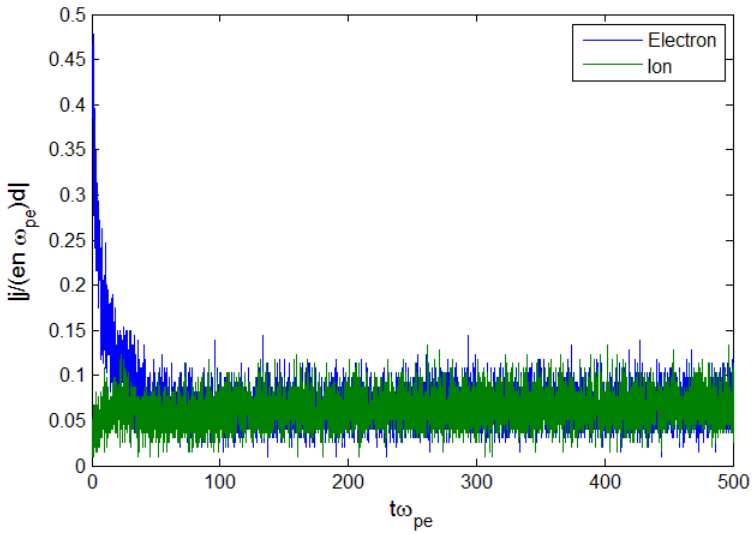

(c) Charging current density history

Figure 4.8 Potential, charges, current densities in charging process for dielectric sphere in stationary plasma (d is Debye length)

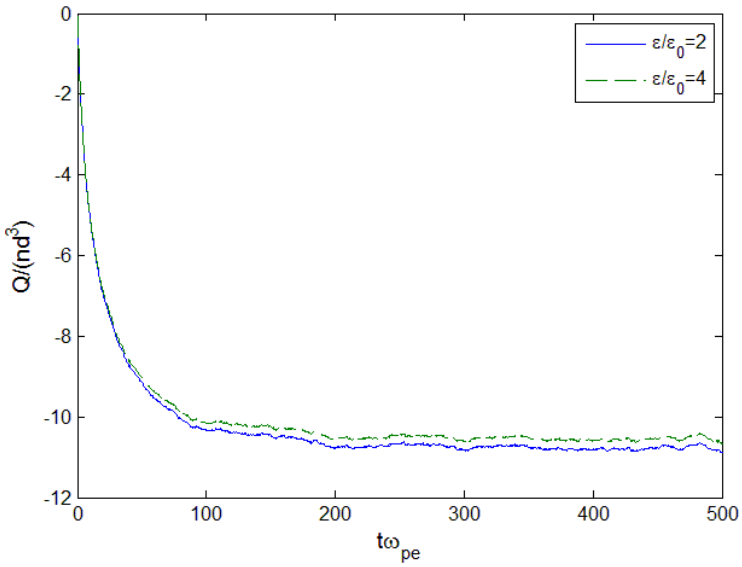

Figure 4.9 Accumulated charges history for dielectric sphere in stationary plasma for different electric permittivity (d is Debye length)

Figure 4.10 shows the potential contour at steady state, the potential is almost uniform in the object because of the uniform deposited surface charge and the symmetric geometry of object. The balanced potential is about -1.2. Using orbital motion limited theory (OML); the analytical solution of the current density can be obtained using equations in Table 4.2. The density of electron, ion and total current with potential during the charging process are shown in Figure 4.11. In these plots, the potential is instantaneously potential $\Phi(t)$. They are plotted here to show the relation between current density and potential. In the charging process at different time, the current density is changing with the potential. At steady state where potential is around -1.2,

there is a point cluster representing the current density at different time at steady state in the simulation curve. The charging current densities for single spherical object in stationary plasma obey the OML theory.

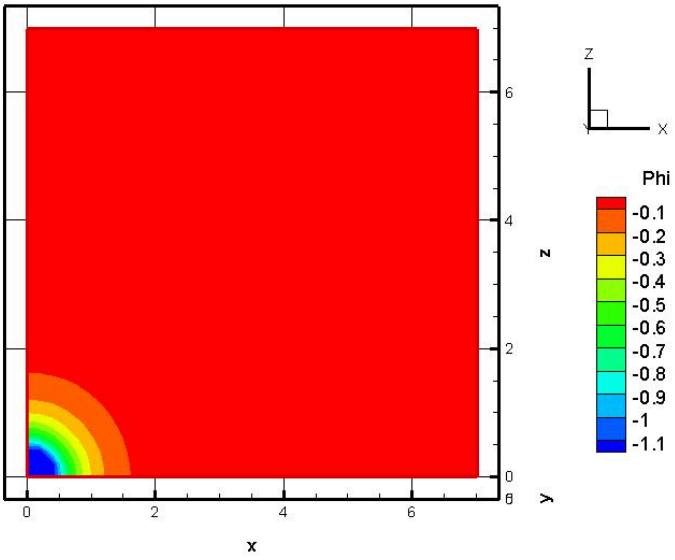

(a)

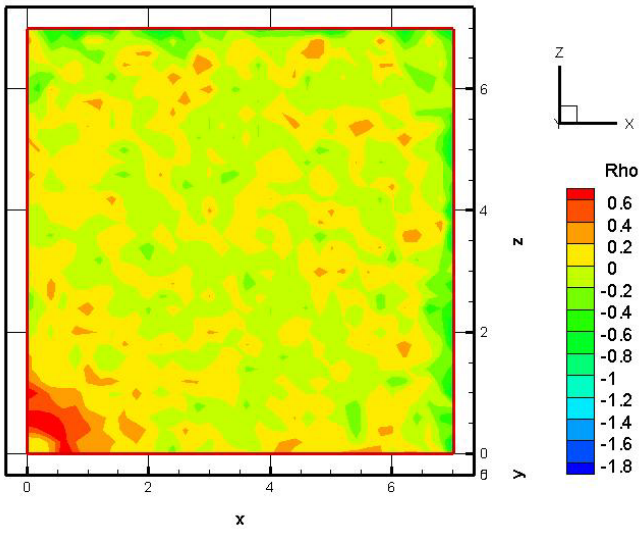

(b)

Figure 4.10 (a) Potential and (b) charge density contour of dielectric sphere in stationary plasma

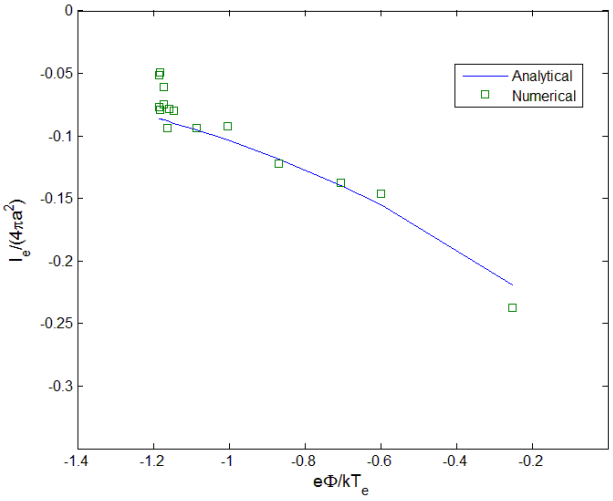

(a)

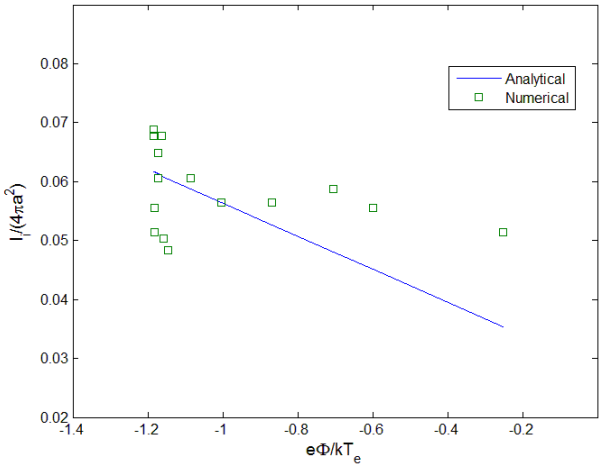

(b)

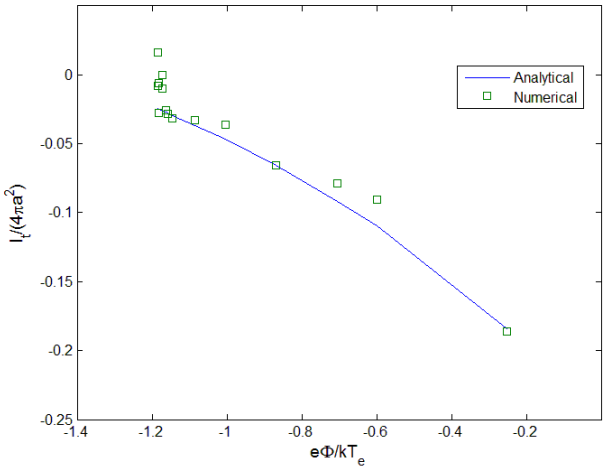

(c)

Figure 4.11 Charging current density of floating potential
(a) electron current density; (b) ion current density; (c) total current density
(Here, the Φ is the transient Φ (t) shown in Fig. 4.8.
The previous Φ vs. t and I vs. t plots are calculated to get I vs. Φ relation.)

For isolated sphere object whose radius is at the level of Debye length, a common procedure to calculate the object charge is to use the free space capacitance $C_0=4\pi\varepsilon_0 a$ multiplied by a factor based on the Debye-Hückel approximation [92]

$$C = 4\pi\varepsilon_0 a(1 + a / \lambda_D) . \tag{4.14}$$

For floating potential Φ_s, the charge on isolated sphere is

$$Q = 4\pi\varepsilon_0 a\Phi_s(1 + a / \lambda_D) . \tag{4.15}$$

In Figure 4.12, the accumulated charge on object surface as a function of floating potential is compared with the Debye-Hückel approximation and the charge in free space. For the spherical object with radius $a/\lambda_D = 0.44$. The accumulated charge on object surface is more closed to Debye-Hückel approximation. It can be seen from equation (4.15) that the difference of charge on isolated object using these two models vanishes as $a \to 0$.

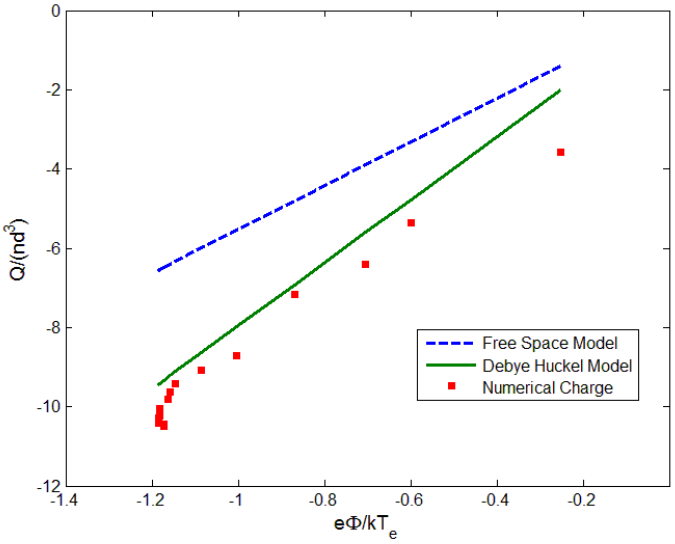

Figure 4.12 Deposited charge changing with potential on dielectric sphere in flowing plasma

4.4.2 Dielectric Spherical Object in Flowing Plasma

In this section, we are presenting the dielectric spherical object in flowing plasma. In this case, the plasma species have initially Maxwellian's distribution. The electrons have no flowing velocity, but the ions have flowing velocity u_i described by Mach number $M = u_i / u_B$, where u_B is the Bohm velocity defined by

$$u_B = \sqrt{\frac{kT_e}{m_i}}$$

The normalized value of u_B is 0.1. The dimensionless plasma conditions for both electrons and ions are listed in Table 4.8. Consider a dielectric spherical object with radius $a/\lambda_D = 0.1$ in this plasma. The object is initially uncharged and accumulates ions and electrons from the plasma.

Table 4.8 Conditions of dielectric spherical object in flowing plasma (after normalization)

Species	Number density $\hat{n}$	Temperature $\hat{T}$	Mass $\hat{m}$	Thermal velocity $\hat{v}_{th}$	Flowing velocity $\hat{u}$
Electrons	1	1	1	1	0
Ions	1	1	100	0.1	$0.1M$

Lapenta [29] investigated the charged dielectric sphere in this plasma condition with different Mach number of ions flow. Compared with the conductor object which has equipotential, the potential on dielectric objects are usually not uniform. On the side facing the ion flow, the potential is positive because of the accumulated positive charge. On the other side of the object, the potential is negative and this negative side is predominant in the whole object. In the downstream area, there is a wake field due to ion focusing.

This case is also simulated using the IFE-PIC model. The simulation is finished with one quarter spherical object in the domain whose size is $\lambda_D \times \lambda_D \times 4\lambda_D$ with uniform mesh size $h/\lambda_D=0.04$. Reflection boundary conditions are applied to the face of x=0 and y=0. The ions flows with Mach number M=3 in negative direction of z axis. The sphere center locates at the position of x=0, y=0 and z=$3\lambda_D$. Figure 4.13 shows the mesh used in this simulation. Figure 4.14 shown the potential and charge density contours on y=0 plane. The same potential profile is obtained compared with the

results in reference [29]. In Figure 4.14 (c), there is a wake where ions are focused behind the object. The positive potential region of object facing ion flow and the negative potential region on the other side are shown in Figure 4.14 (a). This is also shown in Figure 4.15 (a) which is the potential around the dielectric object using the IFE-PIC model. It has similar result compared with the plot in Lapenta's results [29] shown in Figure 4.15 (b).

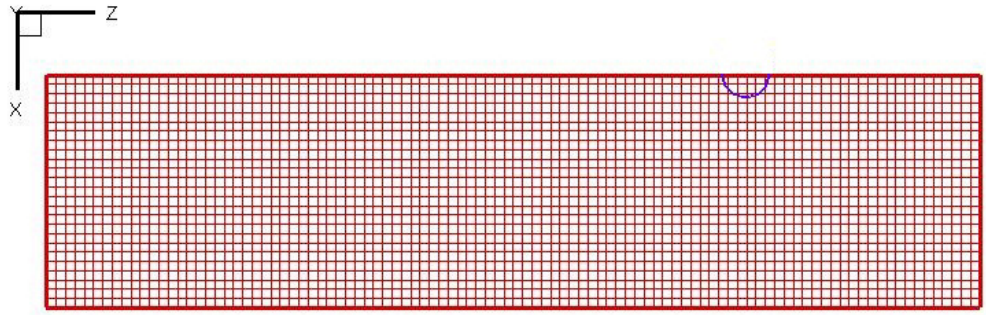

(a) PIC mesh

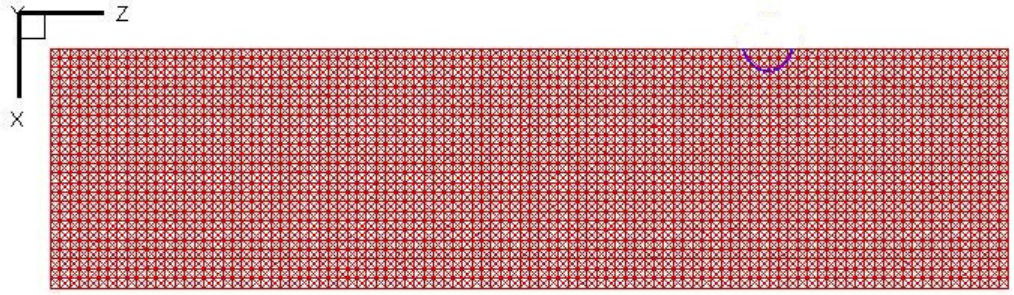

(b) IFE mesh

Figure 4.13 Mesh used in the simulation of dielectric sphere in flowing plasma

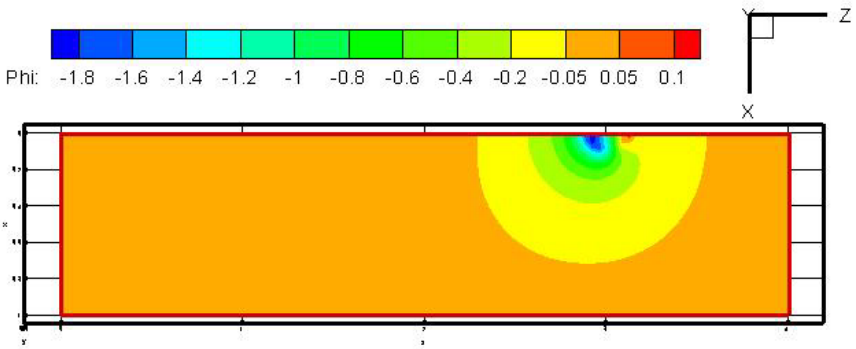

(a)

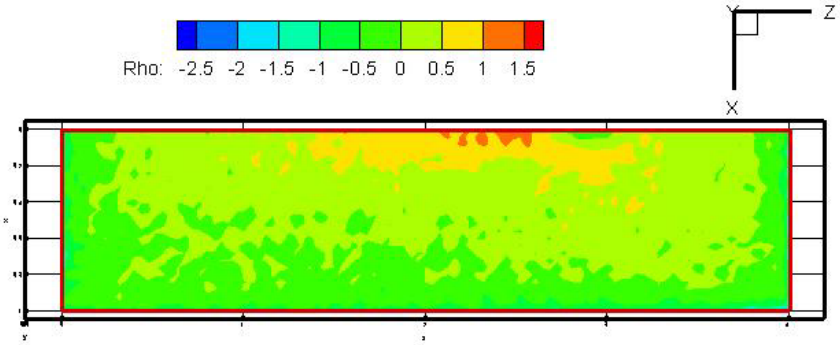

(b)

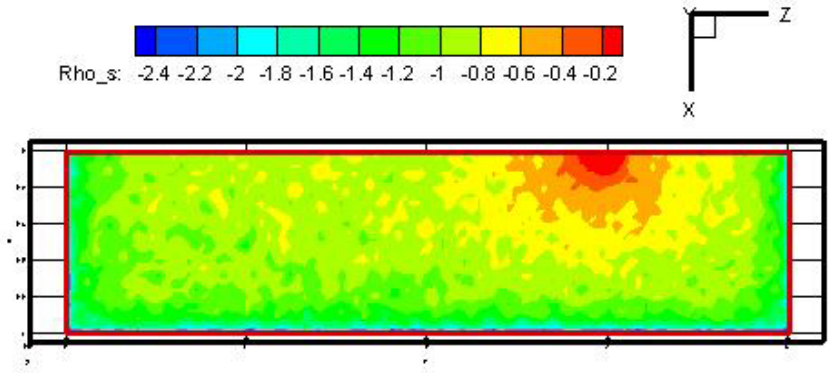

(c)

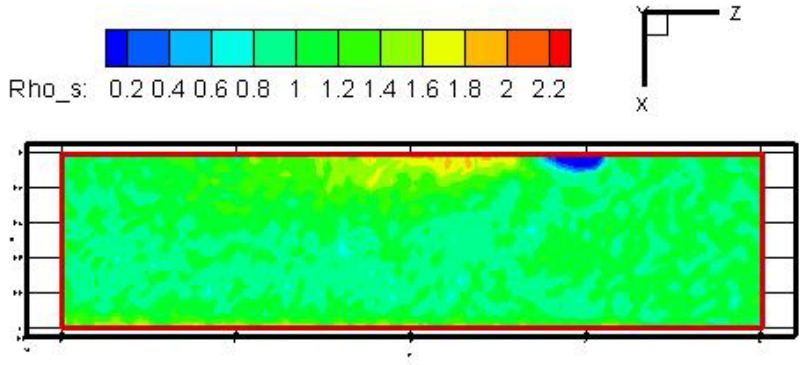

(d)

Figure 4.14 (a) Potential; (b) Charge density
(c) Electron density and (d) Ion density contours
of dielectric spherical object in flowing plasma

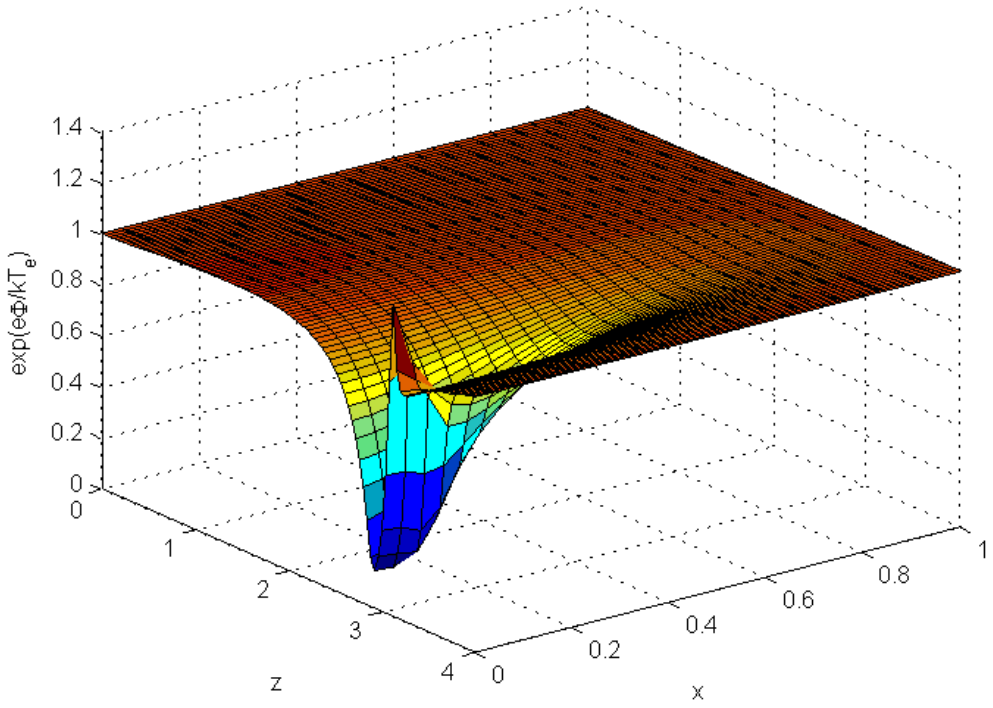

(a)

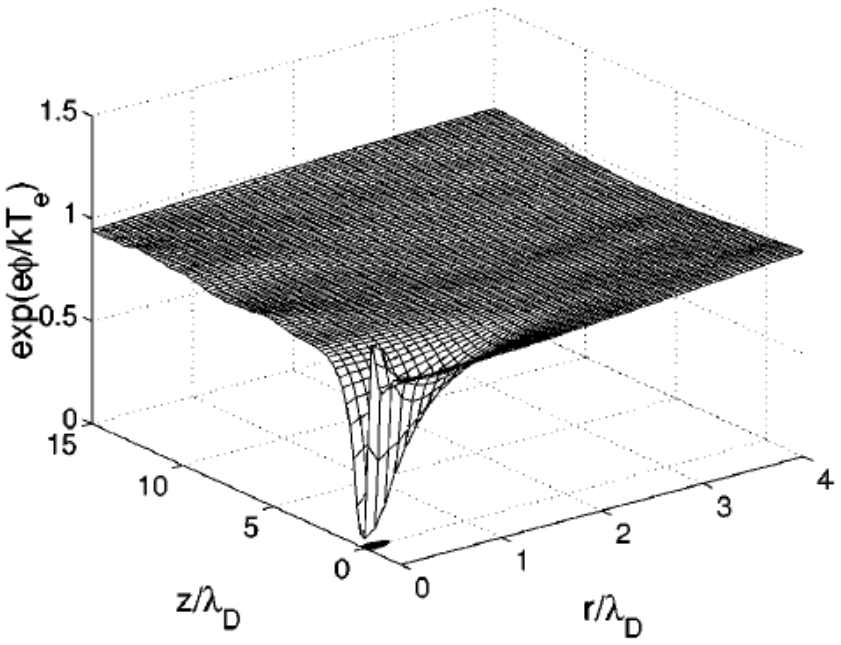

(b)

Figure 4.15 The 3D representation of the Boltzmann factor, governed by the potential round dielectric object (Ion flow *M*=3, x, z normalized by Debye length)
(a) IFE-PIC results; (b) Lapenta's results in reference [29]

From equations in Table 4.5, we can get the equilibrium current density and object potential Φ_s by letting the total current density to be zero. The Debye-Hückel model gives the approximate equilibrium charge on the object at equilibrium potential Φ_s:

$$Q = 4\pi\varepsilon_0 a\Phi_s(1 + a/\lambda_D). \tag{4.15}$$

If the object radius a is small enough compared with the Debye length, this equation can be written as the charge of object in free space

$$Q = 4\pi\varepsilon_0 a\Phi_s. \tag{4.16}$$

Figure 4.16 shows the equilibrium charge on this dielectric object as a function of the Mach number. The equilibrium charge at different Mach number is compared with the results using equation (4.15) and (4.16). The simulation results are more closed to the Debye-Hückel approximation than Lapenta's [29] result which is more closed to the free space model.

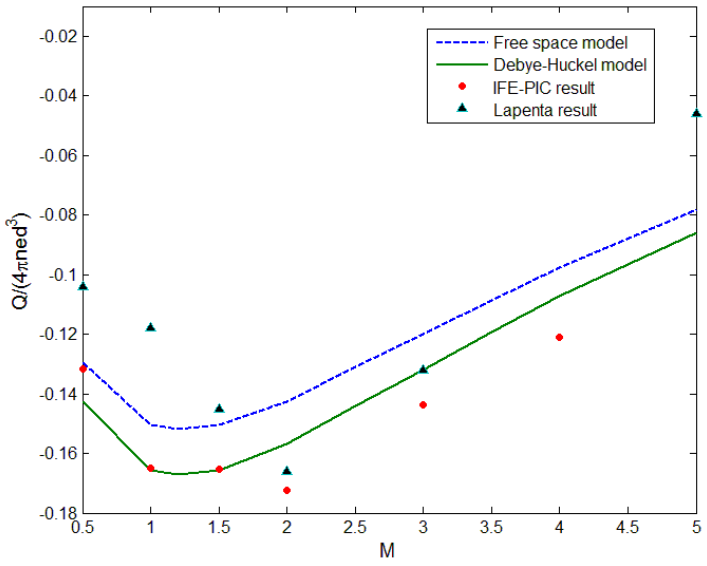

Figure 4.16 Equilibrium charge on dielectric object immersed in plasma with drifting ions flow and stationary electrons

4.5 Modeling Charging of a Cluster of Small Dielectric Spheres

In this section we consider the charging process of dusts in dusty plasma. In such a problem, the inter-dust distance is much smaller than the Debye length and hence the dusts will interact with each other as well as the ambient plasma. As a result, the current collection and charging could be very different from that of a single sphere situation studied in previous sections. As mentioned in Chapter 1, the use of body fitting mesh could be difficult in setting up a simulation with multiple internal boundaries inside the simulation domain. We have studied the single dust charging process in stationary plasma in section 4.3.1. In this section, we will use the IFE-PIC method to simulate the dusts interactions for 2 simulation setting. One considers a cluster of 4 small spheres. The second considers a cluster of 5 small spheres. Both of these cases are compared with a single dust case. This section only considers the stationary plasma case.

The geometry setup of these three cases is shown in Figure 4.17. The single sphere locates in the center of the simulation domain. The radius is taken to be $a/\lambda_D = 0.44$ smaller than the Debye length λ_D. The electric permittivity of the spheres is $\varepsilon/\varepsilon_0=2$. In the four sphere case, those spheres with same radius $a/\lambda_D = 0.44$ are locating symmetrically around the simulation domain center at a same plane and the distance between the centers of neighboring spheres is $4.5a$. For five spheres case, there is one more sphere at the sphere cluster center based on the four sphere case. In these simulations, the plasma condition is the same as Table 4.7 listed in section 4.3.1.

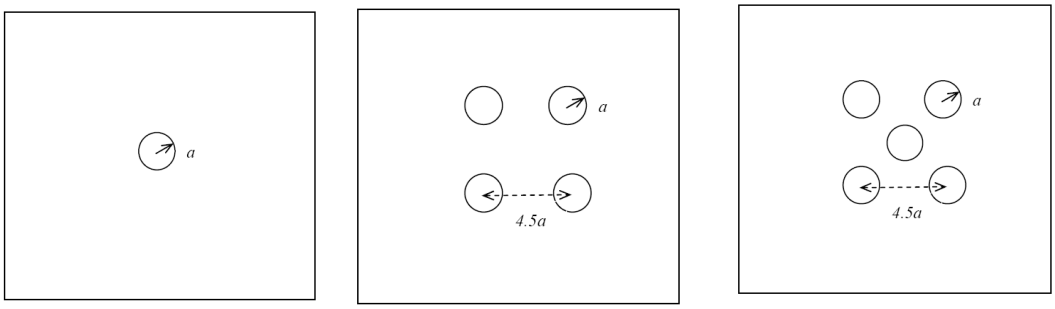

(a) Single sphere (b) Four spheres (c) Five spheres

Figure 4.17 Sketch of multiple sphere cluster

4.5.1 Four Sphere Cluster in Stationary Plasma

In the four sphere cluster simulation, the simulation domain is $12\lambda_D \times 12\lambda_D \times 11\lambda_D$. A uniform mesh is used with mesh size $h/\lambda_D = 0.2$. In order to save the cost of computation, the PIC simulation is carried out with the reflection boundary conditions for particles on x=0, y=0 and z=0 faces. Using the origin point (0, 0, 0) as the symmetric center of the spheres, half sphere is simulated locating at point (1.0, 1.0, 0). The simulation mesh is shown in Figure 4.18.

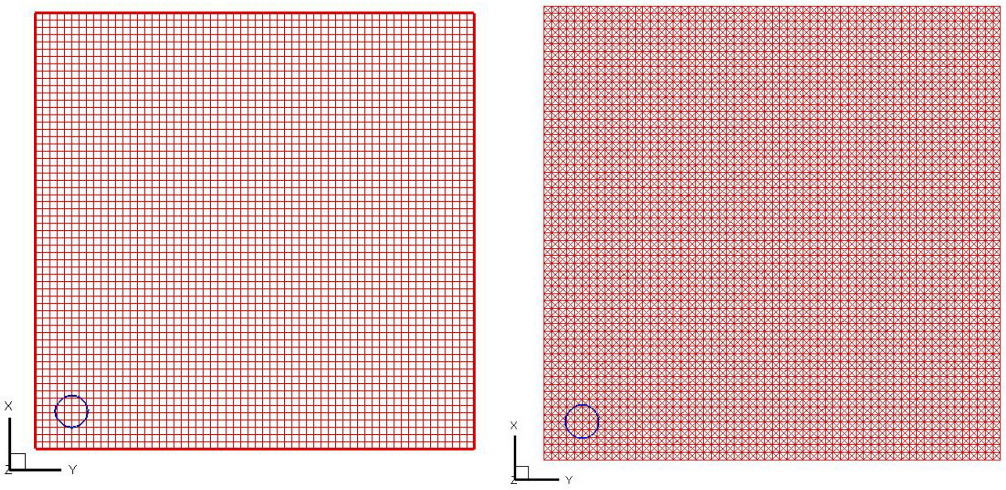

(a) PIC mesh (b) IFE mesh

Figure 4.18 Mesh used in the simulation of four sphere cluster in sationary plasma

The spheres are negatively charged at steady state, and their sheaths interfere with each other. Figure 4.19 shows the potential and charge density profile at steady state. The accumulated charge for each sphere is -8.6255 and the charging history of these spheres is shown in Figure 4.20 where the accumulated charge changing with time is given.

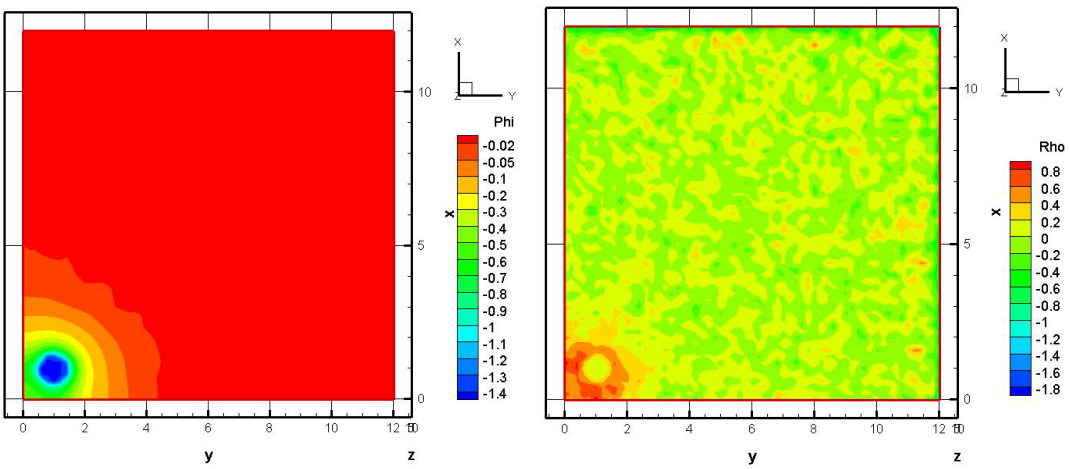

(a) Potential (b) Total charge density

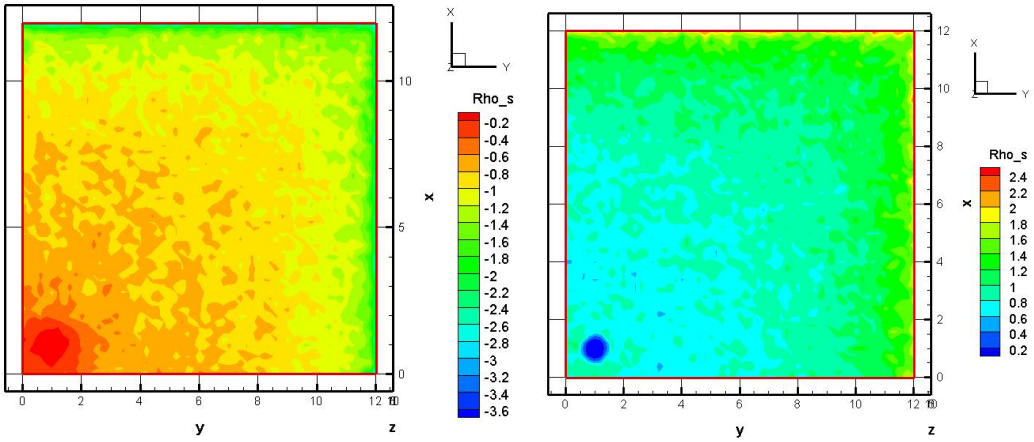

(c) Electron density (d) Ion density

Figure 4.19 Potential and charge density contours of four sphere cluser in stationary plasma

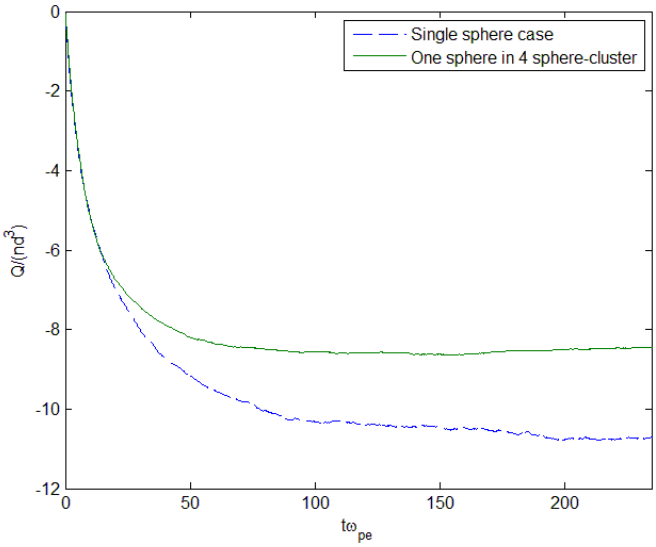

Figure 4.20 Comparison of the charging of one sphere in the 4 sphere-cluster with that of one sphere in the single sphere case

4.5.2 Five Sphere Cluster in Stationary Plasma

In the five sphere simulation, the domain and mesh size are the same as that used in four sphere cluster simulation. However, there is one more sphere locates at the origin point besides the existing four spheres. As the four sphere cluster case, the symmetric boundary conditions are applied on all domain faces. The outer four spheres are simulated with half sphere and the inner single sphere is simulated with one eighth sphere. The simulation mesh is shown in Figure 4.21.

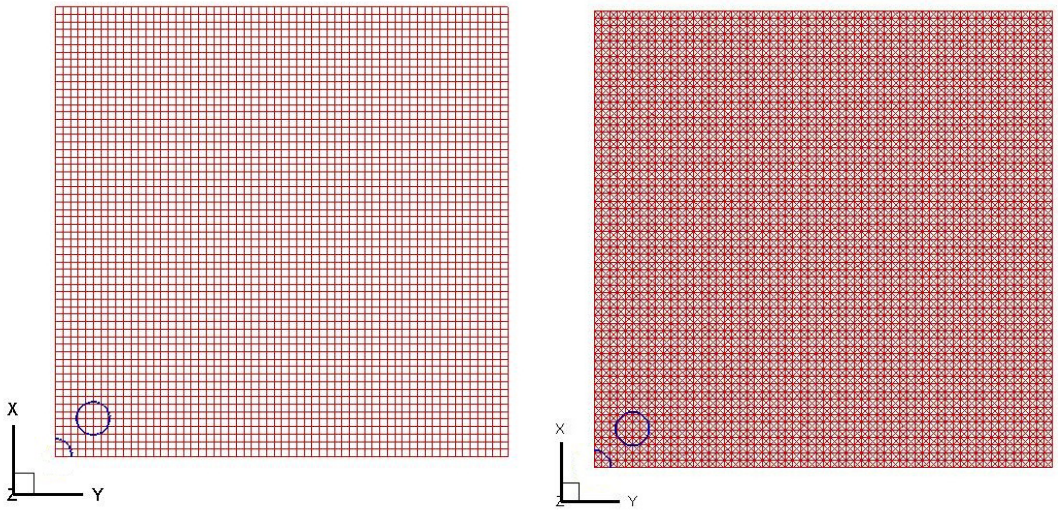

(a) PIC mesh (b) IFE mesh

Figure 4.21 Mesh used in the simulation of five sphere cluster in sationary plasma

The spheres are negatively charged at steady state, and their sheaths interfere with each other. Figure 4.22 shows the potential and charge density profile at steady state. The accumulated charges of inner sphere and outer sphere are separately -3.9620 and -7.7678 which are smaller than the charge of single sphere and four spheres at steady state. Figure 4.23 shows the charging history of these spheres.

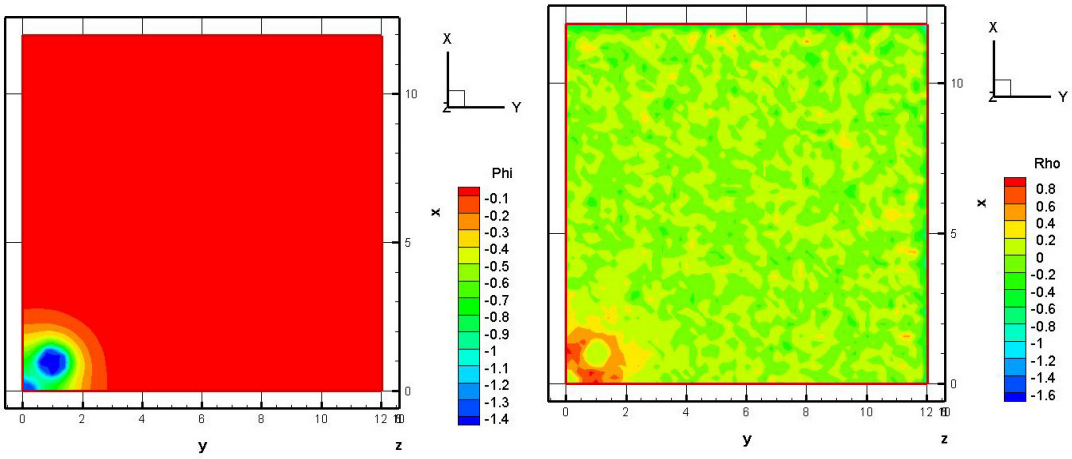

(a) Potential (b) Total charge density

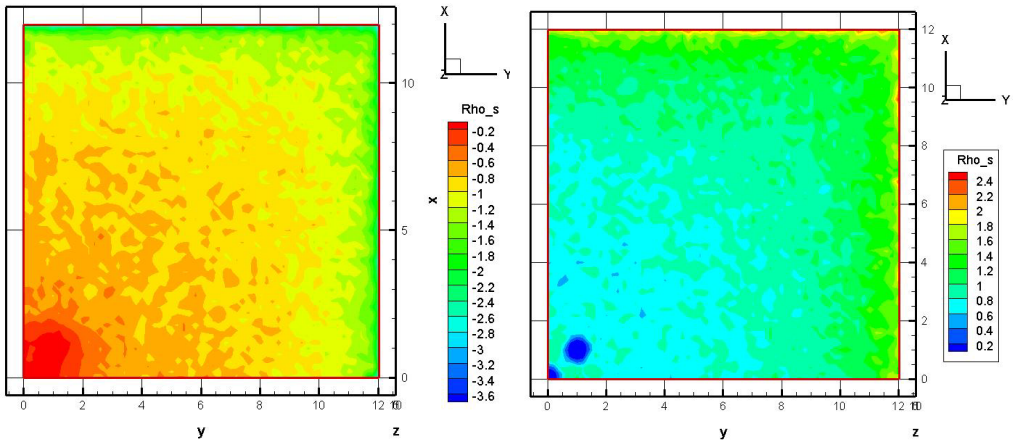

(c) Electron density (d) Ion density

Figure 4.22 Potential and charge density contours of five sphere cluster in stationary plasma

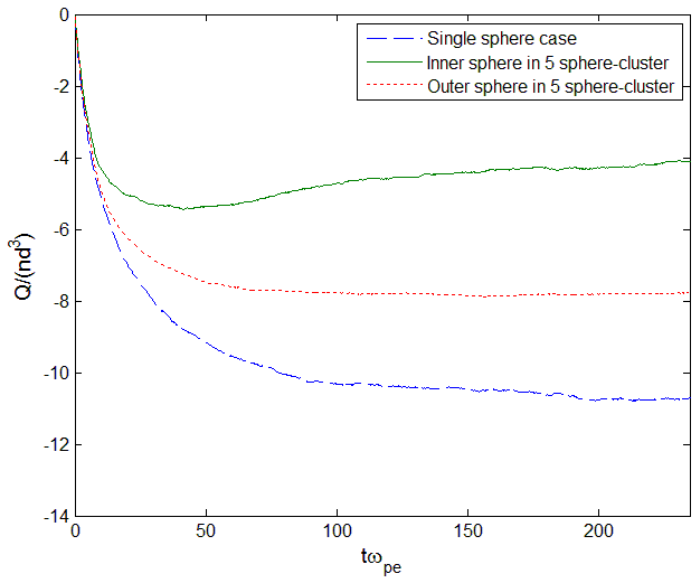

Figure 4.23 Comparison of the charging of one sphere in the 5 sphere-cluster system with that of one sphere in the single sphere case

Comparing the charging history of the single, four and five spheres cases shown in Figure 4.24, less charge is accumulated with the increasing of spheres number, especially for the inner sphere closed in outer sphere cluster simulated in five spheres case. The charge and potential at steady state for each case is listed in Table 4.9. Using the relation of potential and charge, we can get the capacitance for each sphere at steady state as $C = Q/\Phi$ which are also listed in Table 4.9. The capacitance of sphere in free space is $C_0 = 4\pi\varepsilon_0 a$ and the isolated sphere in plasma is $C = 4\pi\varepsilon_0 a\ (1+a/\lambda_D)$ according to Debye-Hückel approximation [92]. They are separately 5.5292 and 7.9621 for sphere with radius a/λ_D=0.44. In section 4.3.1, we see that the single sphere's capacitance is more closed to the Debye-Hückel approximation in stationary plasma. For coupling spheres, the spheres' capacitance is much smaller than this value.

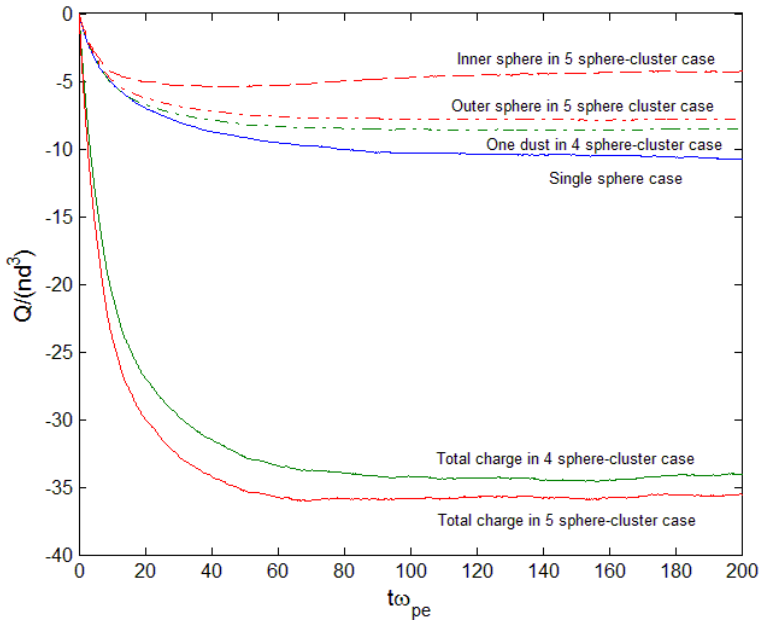

Figure 4.24 Charging history of single, four, five sphere cluster in stationary plasma

Table 4.9 Accumulated charge and potential at steady state in single, four, five sphere cluster cases

Spheres type	Charge ($Q/(nd^3)$)	Potential ($e\Phi/kT_e$)	Capacitance (Q/Φ)
Single sphere case	-10.917	-1.20	9.0975
One dust in four sphere cluster case	-8.6255	-1.47	5.8677
Inner dust in five sphere cluster case	-3.9620	-1.37	2.8920
Outer dust in five sphere cluster case	-7.7678	-1.47	5.2842
Total charge in four sphere cluster case	-34.5052	-	-
Total charge in five sphere cluster case	-35.0332	-	-

4.6 Conclusion

In this chapter, we developed the three-dimensional IFE-PIC model to solve the potential and electrostatic field of objects and space in a plasma environment. Some cases are given to simulate conductive and dielectric spherical objects in stationary and flowing plasma. The homogeneous and non-homogeneous interface conditions are applied in these cases. By comparing with analytical solutions such as OML theory and the Debye-Hückel approximation, the results show that this model can simulate the object charging process well and be used in object-plasma interaction problems. At last, the problem about multiple dusts in dusty plasma is studied by simulating the four and five dusts cluster in stationary plasma. The capacitance of each dust in a dusts cluster shows a smaller value compared with that for single dust.

Chapter 5

Modeling Secondary Electron Emission Experiments

5.1 Introduction

Secondary electron emission is an important charging mechanism in space. This chapter models a vacuum chamber experiment of the secondary electron emission. A standard method to measure the yield of secondary electron is by experiment setup similar to that shown in Fig.1.5. In such a setup, the target surface is irritated by electron beam emitted from an electron gun. The secondary electrons emitted are collected by a collector shell. The secondary electron yield is determined by measuring the current emitted from the electron gun and that collected by the collector. Such an experimental setup produces accurate measurements when all beam electrons hit the target surface and all secondary electrons emitted from the target are collected by the collector. This is usually the case for high energy electron beam emission when the trajectories of the electrons are not affected by the chamber facility. However, for low energy beam emission, not all beam electrons may hit the target surface and not all secondary electrons emitted may be collected by the collector, as their trajectories may be influenced by the small electric field inside the chamber. When this happens, the facility could introduce a significant facility error into the simulation. This modeling study is performed to support the secondary electron emission experiment performed at ONERA.

The goal of this experiment is to measure secondary electron emission under low energy electron impingement. The purpose of the modeling is to study the facility error in the experiment through modeling and experimental data comparison.

The experiments in this chapter were performed by ONERA (Office National d'Etudes et Recherches Aérospatiales), the French national aerospace research center.

5.2 Experiment Facility and Simulation Motivation

This experiment facility is shown in Figure 5.1. The main parts of the facility include chamber, inner sphere shell, electron gun and target plate, as shown in Figure 5.1 and 5.2. The primary electron beam is injected from the electron gun which is fixed at the top of chamber. There are three holes on the inner sphere shell. The electron gun enters the domain of the chamber through the top hole on the inner shell. The other two holes on the inner shell are used to set up the parts of the facility. The sketch of dimension and relative position is shown in Figure 5.2 and Figure 5.3.

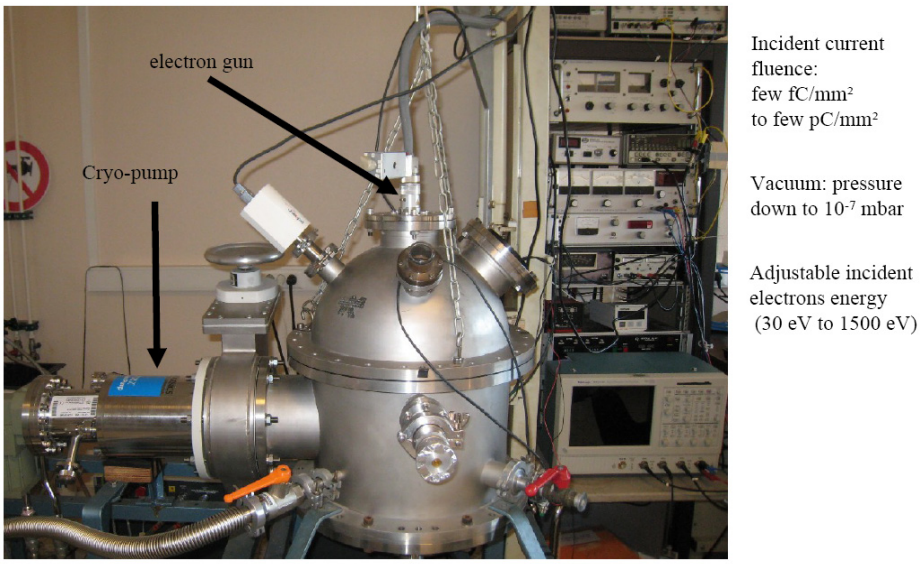

(a) Overview of experiments facility

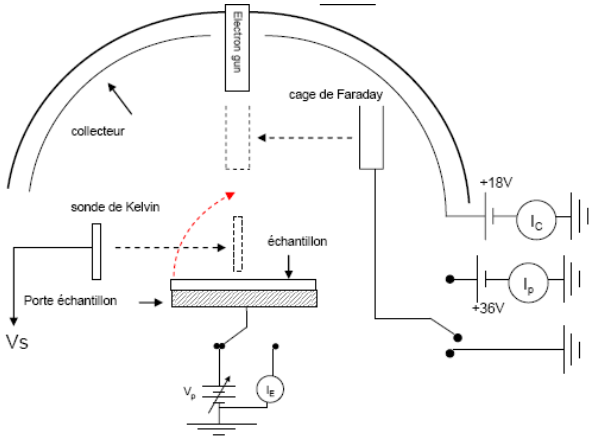

(b) Sketch of facility structure

Figure 5.1 Experiment facility setup

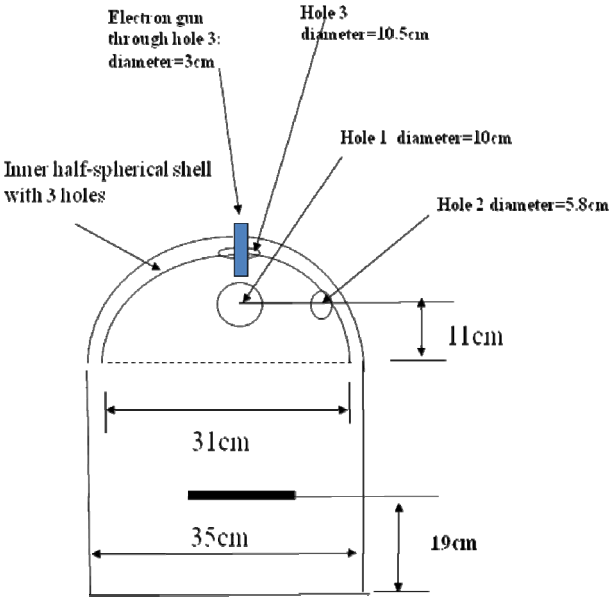

Figure 5.2 Geometry of facility setup sketch

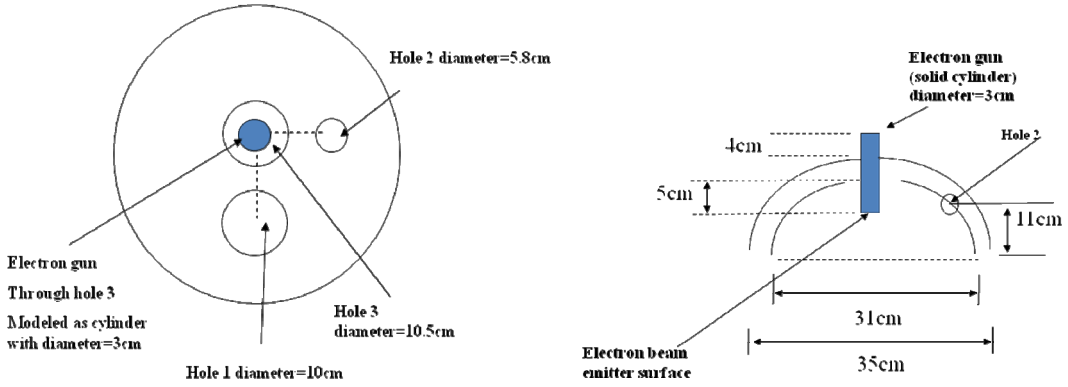

(a) Top View (b) Side View

Figure 5.3 Position of the holes on inner shell

The potential of the chamber and electron gun is fixed to be zero while the inner shell potential is an arbitrary value. It is usually a positive potential to collect electron in the chamber. The target plate size is 5cm×10cm with conductive material. A fixed potential with arbitrary value is applied to this plate.

A primary electron beam is emitted into the chamber as a drifting Maxwellian distribution with temperature 0.1eV. The drifting energy is in a range of 5eV to 1000eV. Charges are lost once electrons hit the chamber wall or target plate. After hitting the target plate, the primary electrons from the electron gun will induce secondary electrons from the plate. The inner shell records the current density of the electrons collected by it.

This experiment assumes all of the primary electrons injected from the electron gun hit the target plate and then the secondary electrons emitted from the target plate are all collected by the inner spherical shell. The secondary electron yield is obtained by comparing the amount of primary electrons and secondary electrons which are separately exhibited by the electron gun current and inner shell current. However, this current collected on inner shell can not exactly present the amount of the emitted secondary electrons. For example, parts of the emitted secondary electrons are collected by the electron gun before reaching the inner shell, there are still some secondary electrons move through the holes on the inner shell and are collected by the outer shell. Thus, the assumption used to measure the secondary electron yield is not precise. Meanwhile, if the energy of primary electron beam is low, not all primary electrons are collected by the target plate. This also causes measurement error in the experiments. Here, numerical simulation is helpful to be introduced. It can predict the proportion of secondary electrons collected by inner spherical shell to adjust the measurement in experiments. It can also give a criterion to the energy of primary electron beam to show whether all of them hit the target plate. If not, the proportion is also given. Thus, the numerical simulation can assist the experiment to reduce the error and get the secondary electron yield curve.

5.3 Simulation Model

5.3.1 Primary Electron Beam

Neglecting the collisional effects, we consider the primary electron beam as collisionless. The kinematics of electrons is affected by the initial velocity and electrostatic force on them according to Newton's second law and Lorentz's force. The electrostatic field in the domain is solved from the Poisson's equation.

Primary electron beam has emission energy

$$E = \frac{1}{2} m v_d^2 , \tag{5.1}$$

thus the drifting velocity is

$$v_d = \sqrt{\frac{2E}{m}} . \tag{5.2}$$

We can get the beam current from the electron gun

$$I = \frac{Q}{t} = n v_d e A = \pi r^2 v_d e n , \tag{5.3}$$

where Q is the charge emitted in time t, n is the charge number density, A is the emission area and r is the radius of the electron gun exit. Assuming j is the current density, the charge number density is

$$n = \frac{I}{\pi r^2 v_d e} = \frac{j}{v_d e} . \tag{5.4}$$

5.3.2 Secondary Electron Yield Function

When impacting a surface, the electrons are reflected or absorbed by the material (Whipple, 1981, [4]). If absorbed, they may induce secondary electrons. The secondary electrons are emitted with a characteristic energy spectrum which is assumed to be a Maxwellian energy distribution with a mean energy of 2eV [2].

The parameter describing the secondary electrons is the yield which is defined as the number of secondary electrons produced by incident electrons. The yield value changes with the incident electron energy. It can be expressed as the function [47]

$$\delta_e(E)=1.28\ \delta^{\max}\left(\frac{E}{E^{\max}}\right)^{-0.67}\left(1-\exp\left(-1.614\left(\frac{E}{E^{\max}}\right)^{1.67}\right)\right), \tag{5.5}$$

where E is the primary electron energy, $\delta^{\max}$ and $E^{\max}$ are the maximum yield and the corresponding primary energy. The maximum yield and corresponding primary electron energy for different materials are list in Table 5.1. For Aluminum material in this experiment, the parameters are chosen as $\delta^{\max}$=2, $E^{\max}$=400eV.

Table 5.1 Representative values of maximum yield energy at maximum yield for secondary electron emissions by primary electrons [47]

Material	$\delta^{\max}$	$E^{\max}$ (keV)
Al	2.00	0.40
Mg	0.80	0.24
Cu	1.53	0.40
C	1.06	0.40
Silicon crystal	0.89	0.45

5.3.3 Secondary Electron Current Density

The incident electron current is given by [2]

$$j_e = e\frac{2\pi}{m_e^2}\int_0^{\infty} dE\int_0^{\pi}\sin\theta d\theta f(E), \tag{5.6}$$

where E is the incident electron energy, f (E) is the energy distribution, θ is the

incident angle from the normal direction of the surface to the incident direction. Once the yield function is known, the emitted current density due to secondary electron for a negatively biased surface is given by

$$j_{se} = -e\frac{2\pi}{m_e^2}\int_0^\infty\int_0^\infty\int_0^\pi \sin\theta g(E^*,E)\delta_e(E,\theta)f(E)d\theta dE^* dE\,, \tag{5.7}$$

where $g(E^*, E)$ is the normalized emission spectrum of secondary electrons at energy E^*, $\delta_e(E, \theta)$ is the yield function of primary electrons impacting with energy E at incident angle θ. Since the spectrum $g(E^*, E)$ is approximately independent of E [2], it can be separated from the integral. Then the secondary electron current density is written as

$$j_{se} = -e\frac{2\pi}{m_e^2}\int_0^\infty g(E^*)dE^*\int_0^\infty dE\int_0^\pi \sin\theta d\theta\delta_e(E,\theta)f(E)\,. \tag{5.8}$$

Consider each cell on the surface of the target plate, for an electron hitting the plate with energy E, the secondary current density j_{se} with energy E^* induced by this electron should be

$$j_{se} = \int_0^\infty g(E^*)dE^*\delta_e(E,\theta)j_e\,. \tag{5.9}$$

If the number of primary electrons hitting the plate in this cell is N, the sum of the secondary electron current density can be written as

$$j_{se} = \sum_{i=1}^{N} j_{se,i} = \sum_{i=1}^{N}\delta_e(E_i,\theta_i)\int_0^\infty g(E^*)dE^* j_{e,i}\,, \tag{5.10}$$

where $j_{e,i}$ is the current density in this cell caused by the i^{th} hitting primary electron, $j_{se,i}$ is the emitted secondary electron current density in this cell caused by the i^{th} primary electron, E_i and θ_i are energy and incident angle of the i^{th} primary electron. The incident electrons with different incident energy and angle will generate secondary electrons separately; the sum of these secondary electron current densities in a given mesh cell is the emission current density in this cell. The initial positions of the secondary electrons are uniformly distributed in this cell.

The integral of $g(E^*)$ over zero to infinity is 1, thus equation (5.10) becomes

$$j_{se} = \sum_{i=1}^{N} j_{se,i} = \sum_{i=1}^{N}\delta_e(E_i,\theta_i)j_{e,i}\,. \tag{5.11}$$

The Maxwellian distribution function for drifting plasma without external electric field is

$$f(v)=\left(\frac{m}{2\pi kT}\right)^{3/2}\exp\left(-\frac{m(v-v_d)^2}{2kT}\right). \tag{5.12}$$

Assuming $v_r = v_d/v_{th}$ and define thermal velocity as $v_{th} = (kT/m)^{1/2}$, the one-side current density is given by

$$j_{se}=en\int_{-\infty}^{\infty}\int_{-\infty}^{\infty}\int_{0}^{\infty} v\,f(v)\,dv_z dv_y dv_x=\frac{1}{2}\sqrt{2}env_{th}\left(\frac{\exp\left(-v_r^2/2\right)}{\sqrt{\pi}}+\frac{v_r}{\sqrt{2}}\left(1+erf\left(\frac{v_r}{\sqrt{2}}\right)\right)\right).$$

For stationary electrons, the drifting velocity $v_d = 0$, we can get

$$j_{se}=\frac{1}{\sqrt{2\pi}}envth\,. \tag{5.13}$$

The emitted secondary electron number density in this cell is

$$n=\frac{\sqrt{2\pi}\,j_{se}}{ev_{th}}=\frac{\sqrt{2\pi}\sum_{i=1}^{N}\delta_e(E_i,\theta_i)j_{e,i}}{ev_{th}}\,. \tag{5.14}$$

5.3.4 Cosine Law Distribution of Secondary Electron Emission

The secondary electrons leaving the surface obey the Lambert's cosine law as follows: [48, 49]

"The molecular flux dn across a plane surface element A, due to all molecules having velocity vectors with directions within a small solid angle dω, whose axis makes an angle θ with the normal to A, is given by the cosine law formula.
Hence,

$$dn=\left(\frac{Nv_a}{4}\right)\frac{1}{\pi}A\cos\theta d\omega\,, \tag{5.15}$$

where N is the number density of molecules and v_a = <v>, the average molecular velocity. The molecules leaving a surface do not necessarily produce Maxwell-Boltzmann velocity distribution, for equilibrium conditions, the overall distribution of molecular flux will obey the cosine law."

In the spherical coordinate system shown in Figure 5.4, the solid angle and flux can be written as $d\omega=\sin\theta d\theta d\phi$

$$dn=\frac{N_0}{\pi}\cos\theta\sin\theta d\theta d\phi, \tag{5.16}$$

where $N_0=NAv_a/4$ is the total particle flux from A.

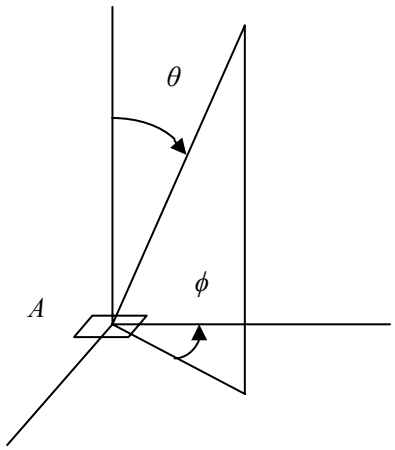

Figure 5.4 The spherical coordinates system

The particle flux inside a small azimuth range $d\phi$ at θ from 0 to $\pi/2$ is

$$dn_\phi=\frac{N_0}{\pi}d\phi\int_0^{\pi/2}\cos\theta\sin\theta d\theta=\frac{N_0}{2\pi}d\phi. \tag{5.17}$$

The particle flux with a particular polar direction range $d\theta$ is

$$dn_\theta=\frac{N_0}{\pi}\cos\theta\sin\theta d\theta\int_0^{2\pi}d\phi=2N_0\cos\theta\sin\theta d\theta. \tag{5.18}$$

The initial emission flux density of secondary electrons obeys these equations which present cosine law with mean energy as 2eV. This can be achieved by the initial velocity distribution.

The azimuthal angle ϕ of the initial velocity is uniformly distributed between 0 and 2π. The polar angle θ of initial velocity can be generated from a single, uniformly distributed random number x in the range $0 \leq x \leq 1$. Then the random angle of departure is determined from this random number as $\theta = \sin^{-1}(x^{1/2})$ [49].

The energy distribution of emitted secondary electron is half Maxwellian distribution with temperature 2eV and the angular distribution obeys the Lambert's cosine law. The energy and velocity distribution of secondary electrons are separately shown in Figure 5.5 and 5.6. The velocity distributions in x and y direction which are stationary Maxwellian distribution, but the velocity in z direction is not half stationary Maxwellian distribution because of the cosine law.

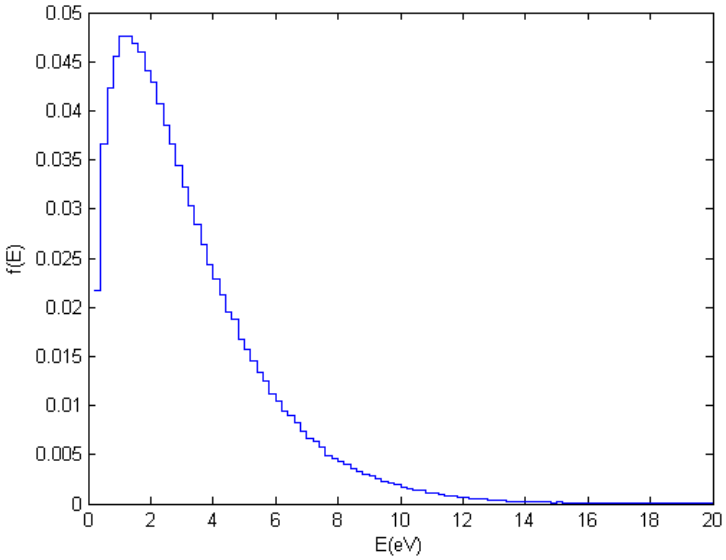

Figure 5.5: Energy distribution of emitted secondary electrons

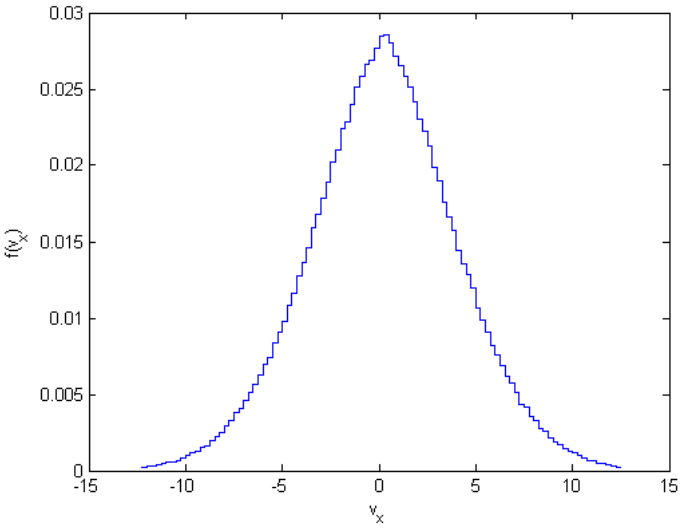

velocity in x direction

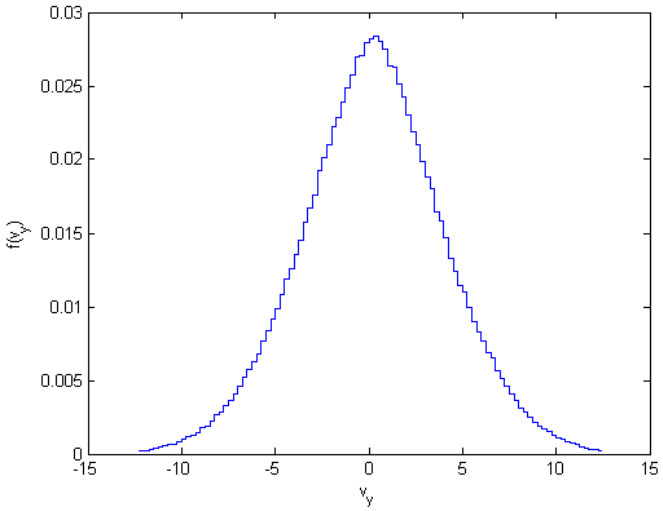

velocity in y direction

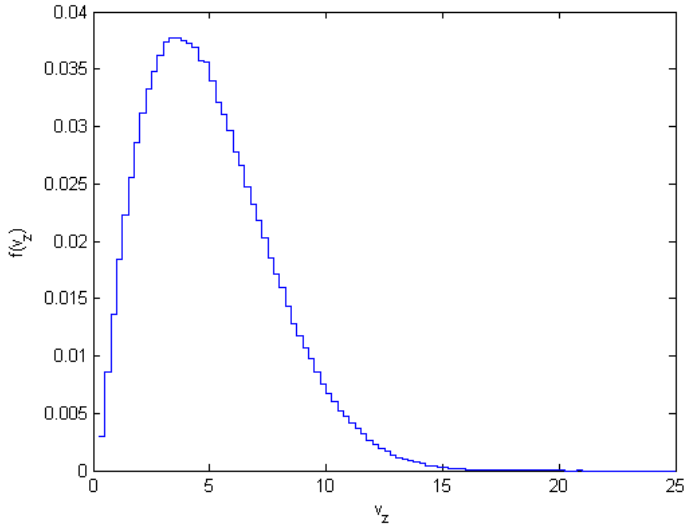

velocity in z direction

Figure 5.6: Velocity distribution of emitted secondary electrons

5.4 Simulation of Experiments for Conductive Targets

5.4.1 Primary Electron Beam hitting Target Plate

The primary electrons are injected from the electron gun with initial velocity normal to the target plate. In this section, we will only consider the case without secondary electrons emission in order to see the effect of the chamber potential to the electrostatic field and particle trajectory, as well as the proportion of primary electrons hitting the target plate.

The simulation is finished in a domain with size 38cm×38cm×45.6cm. The radius of the electron gun is 1.5cm and the primary electron emission area has radius 1.0cm. The potential of chamber and target plate is 0V and the inner sphere shell potential is 36V. The parameters of primary electrons are listed in Table 5.2.

Table 5.2 Primary electron parameters before normalization in secondary electron emission experiment

Emission current I (nA)	10
Temperature T_e (eV)	0.1
Energy E (eV)	5
Drifting velocity v_d (10^5m/s)	13.26
Thermal velocity v_{th} (10^5m/s)	1.326
Number density n (10^8/m^3)	1.5
Debye length λ_D (cm)	19
Frequency ω_{pe} (10^5rad/s)	6.908

Primary electrons are chosen as the reference species, the reference parameters are

$$T_{ref} = 0.1\text{eV},\ \ n_{ref} = 1.5\times10^8 / m^3,\ \ v_{ref} = 1.326\times10^5 m/s,\ \lambda_D = 19\text{cm},$$

we can get the parameters of normalization, as that shown in Table 5.3.

Table 5.3 Primary electron parameters after normalization in secondary electron emission experiment

Temperature $\hat{T}_e$	1
Drifting velocity $\hat{v}_d$	10
Thermal velocity $\hat{v}_{th}$	1
Number density $\hat{n}$	1
Domain size ($L_x/\lambda_D \times L_y/\lambda_D \times L_z/\lambda_D$)	2.0×2.0×2.4
Mesh size h/λ_D	0.02
Inner sphere shell potential $\hat{\Phi}$	360

The fixed potential of the experiment facility generates the asymmetric distribution of potential inside the chamber. This may affect the trajectory of primary electron and secondary electrons, as well as the secondary electron proportion absorbed by the inner sphere shell. When introducing primary electrons to the chamber, we solve the Poisson's equation with space charge. The primary electron beam is considered as Maxwellian distribution with drifting velocity. Time step is 0.0005 which makes the distance electron moves in each time step less than half cell size. Because of the electrostatic field, the electrons will decelerate in z axis direction which is towards the target plate after injection. Some of them will be collected by the target plate, while some will change direction in front of the target plate and move towards the inner sphere shell. Some electrons are absorbed by the chamber wall.

At steady state, the number of simulation particles in the system is stable. The electron number emitted by the electron gun and those absorbed by all parts of the facility are balanced. The potential contours on some cutting slices at steady state are shown in Figure 5.7. Because of the facility potential, the space charge effect on the potential distribution is very small and the potential is asymmetric in the chamber. Figure 5.8 and Figure 5.9 show the space charge density profile on cutting slice at steady state. Most of the primary electrons are collected by target plate, while some reverse direction and move to the inner shell to be absorbed. There is still some charge collected by the chamber wall.

The asymmetric potential and electric field make the asymmetric distribution of the

current density. Figure 5.10 shows the asymmetric current density impingement on the target plate at steady state. The coordinates of the target plate center are x=1 and y=1, which is also the center of the electron gun emission area. The asymmetric current density on target plate makes those mesh cells with larger impingement current density have more secondary electron emitted.

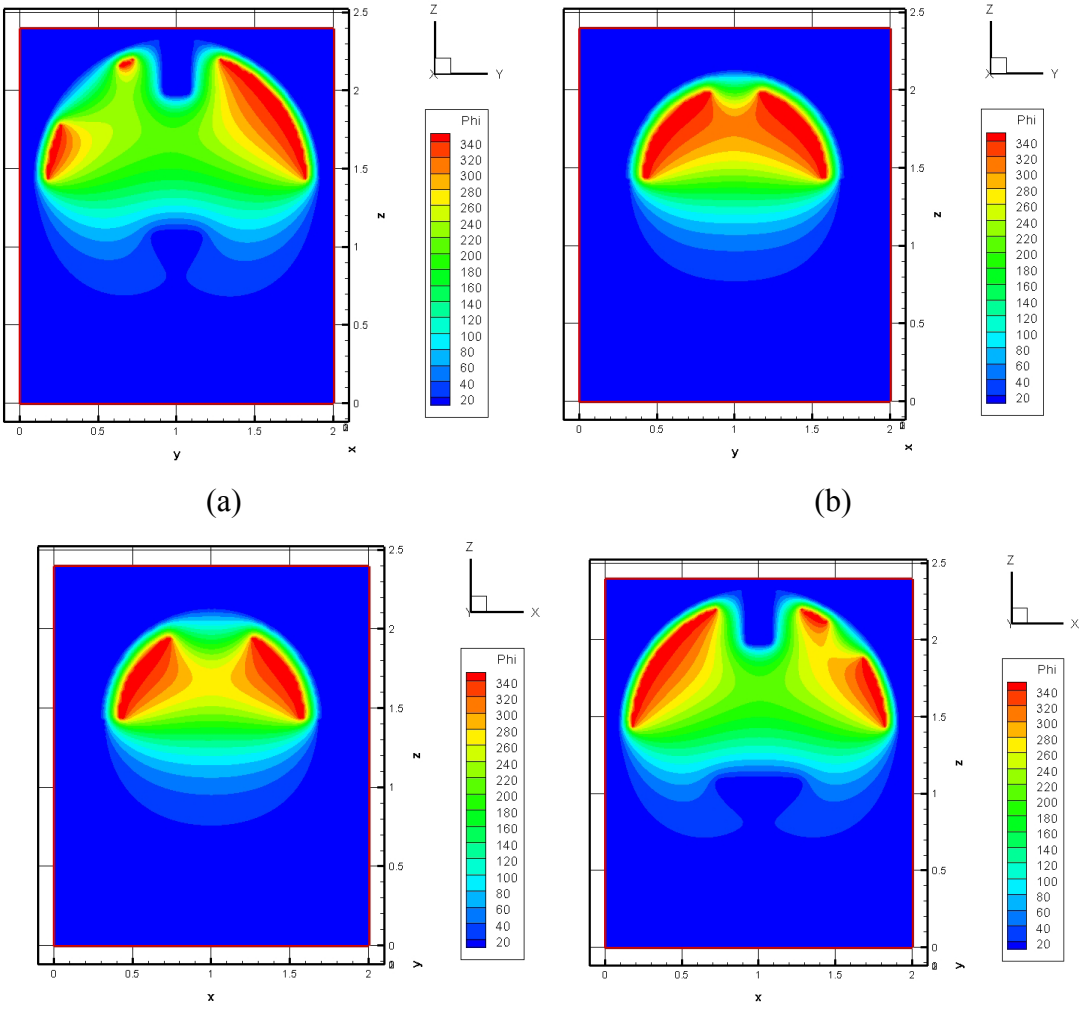

Figure 5.7: Potential contour on cutting slice with primary electrons
(a) Plane x=1.0 through the center of two large holes (hole 1 and hole 3)
(b) Plane x=1.58 through the center of hole 2
(c) Plane y=0.42 through the center of hole 1
(d) Plane y=1.0 through the center of hole 2 and hole 3

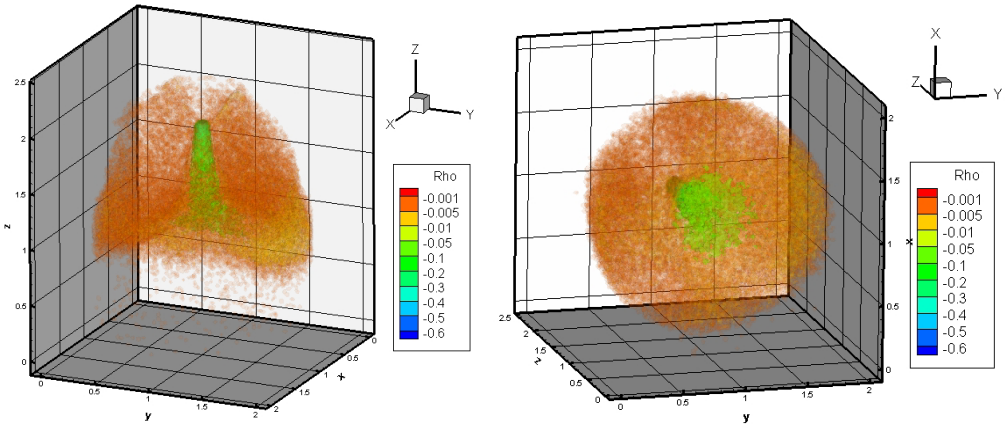

Figure 5.8: Iso-surfaces of the space charge density at steady state

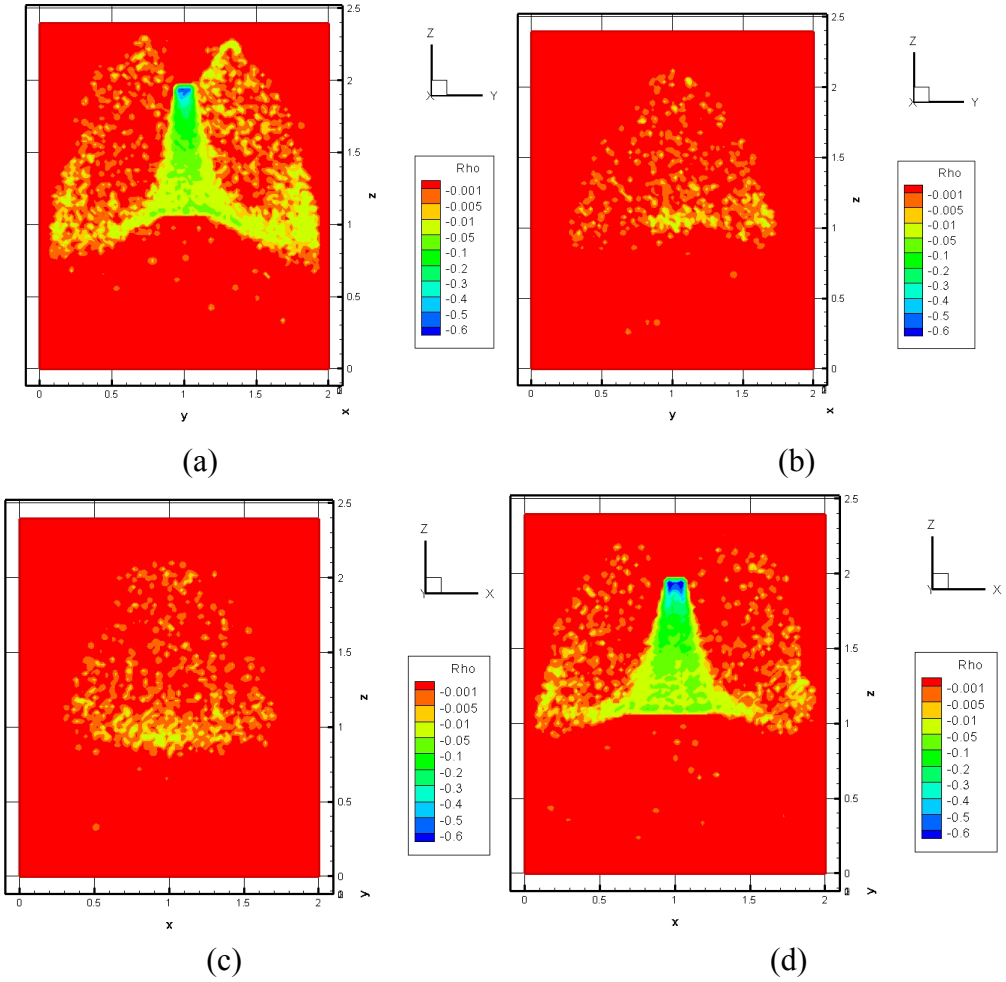

Figure 5.9: Space charge density on cutting slice at steady state
(a) Plane x=1.0 through the center of two large holes (hole 1 and hole 3)
(b) Plane x=1.58 through the center of hole 2
(c) Plane y=0.42 through the center of hole 1
(d) Plane y=1.0 through the center of hole 2 and hole 3

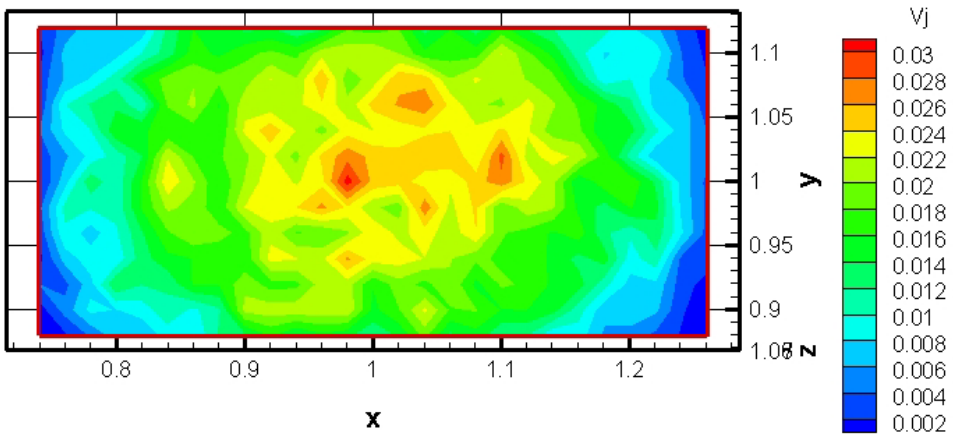

Figure 5.10: Primary electron current density impingement on the target plate at steady state

5.4.2 Secondary Electron Yield at Low Primary Electron Beam Current Density

We are now considering the 10nA current injected from the electron gun whose emission area has radius 1cm. This makes a low beam current density $3.183\times10^{-5}A/m^2$. This primary electron beam makes the target plate emit secondary electrons under the yield function (5.5). The energy distribution of emitted secondary electron is half Maxwellian distribution with temperature 2eV and the angular distribution obeys the Lambert's cosine law.

Different experiments conditions are simulated to investigate the effect of inner sphere shell potential and primary electron beam energy. The increasing of beam energy will cause higher drifting velocity of primary electrons. Some experiment conditions are listed in Table 5.4 with the range of inner shell sphere potential from 5 to 36V and beam energy 5 to 1000eV.

Table 5.4 Experiments conditions

Conditions	1	2	3	4	5	6	7
Inner shell potential (V)	5	9	13.5	18	18	36	36
Beam energy (eV)	5	10	15	20	30	100	1000

The simulation results for the potential contour, primary electrons charge density and secondary electrons charge density for different conditions are shown in Figure 5.11 to Figure 5.14 which are for the combination of inner shell potential and beam energy to be (5V, 5eV), (18V, 30eV), (36V, 100eV), (36V, 1000eV). The effect of space

charge on potential contour is quite small. For conditions with small primary electron beam energy such as 5eV and 30eV, most of the primary electrons are absorbed by target plate. However, there are still some electrons absorbed by the chamber bottom, as shown in Figure 5.11, 5.12. With the increasing of primary electron beam energy such as 100eV and 1000eV, almost all primary electrons are collected by the target plate, shown in Figure 5.13, 5.14. Thus, the case with larger primary electron energy has larger fraction of electrons hitting the target plate. Most of the secondary electrons are collected by the inner shell after emission. There is still a small ratio of them collected by the chamber wall, chamber bottom and electron gun. With the increasing of inner shell potential, the proportion of secondary electrons collected by inner shell also increases. This can be seen from the proportion of primary electrons and secondary electrons collected by facility parts, shown in Table 5.5 and 5.6.

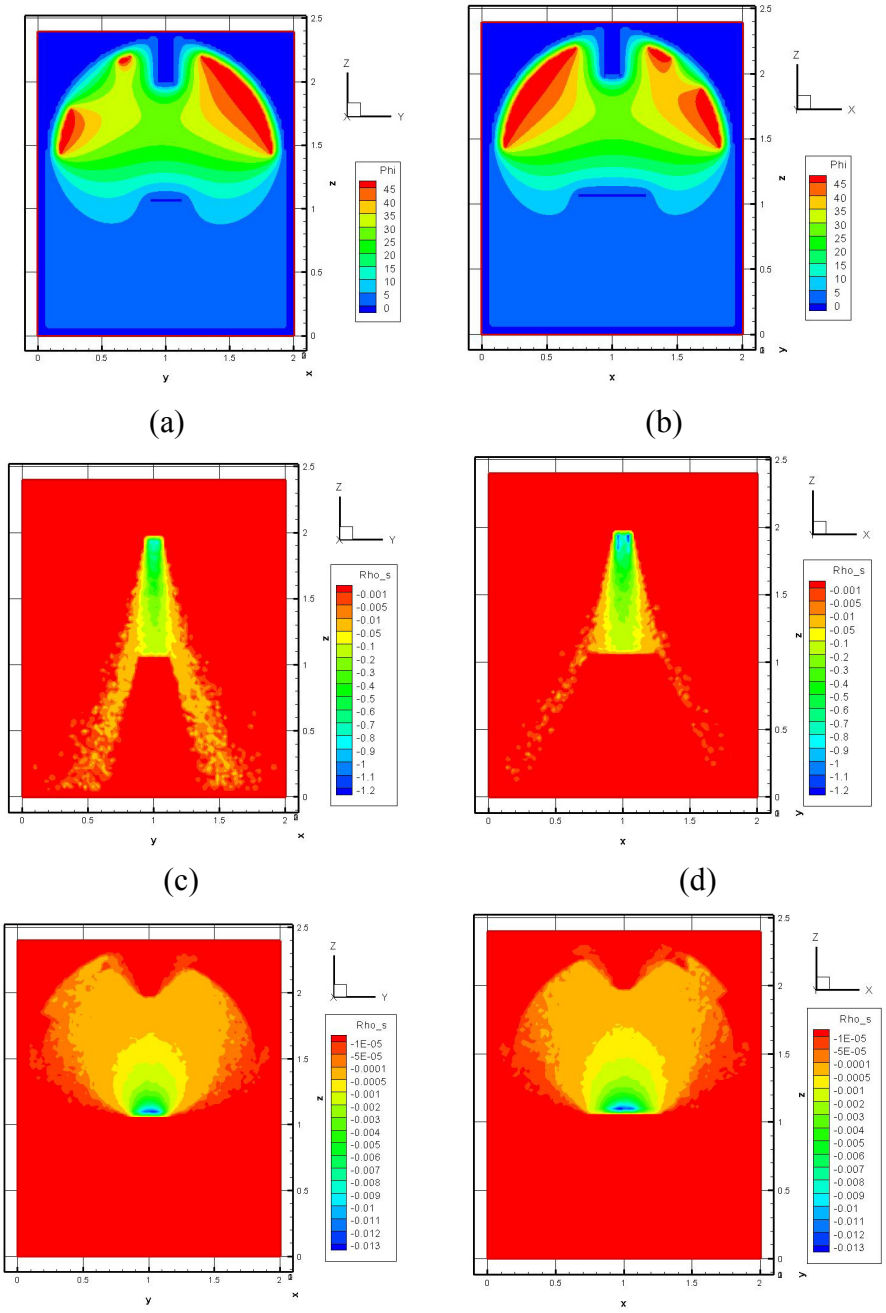

Figure 5.11 Potential and charge density contour at steady state

(Inner shell potential 5V, primary electron beam energy 5eV)

(a) Potential contour of plane x=1.0 through the center of two large holes (hole 1 and hole 3)

(b) Potential contour of plane y=1.0 through the center of hole 2 and hole 3

(c) Charge density contour of primary electrons on plane x=1.0 through the center of two large holes (hole 1, 3)

(d) Charge density contour of primary electrons on plane y=1.0 through the center of hole 2, 3

(e) Charge density contour of secondary electrons on plane x=1.0 through the center of two large holes (hole 1, 3)

(f) Charge density contour of secondary electrons on plane y=1.0 through the center of hole 2, 3

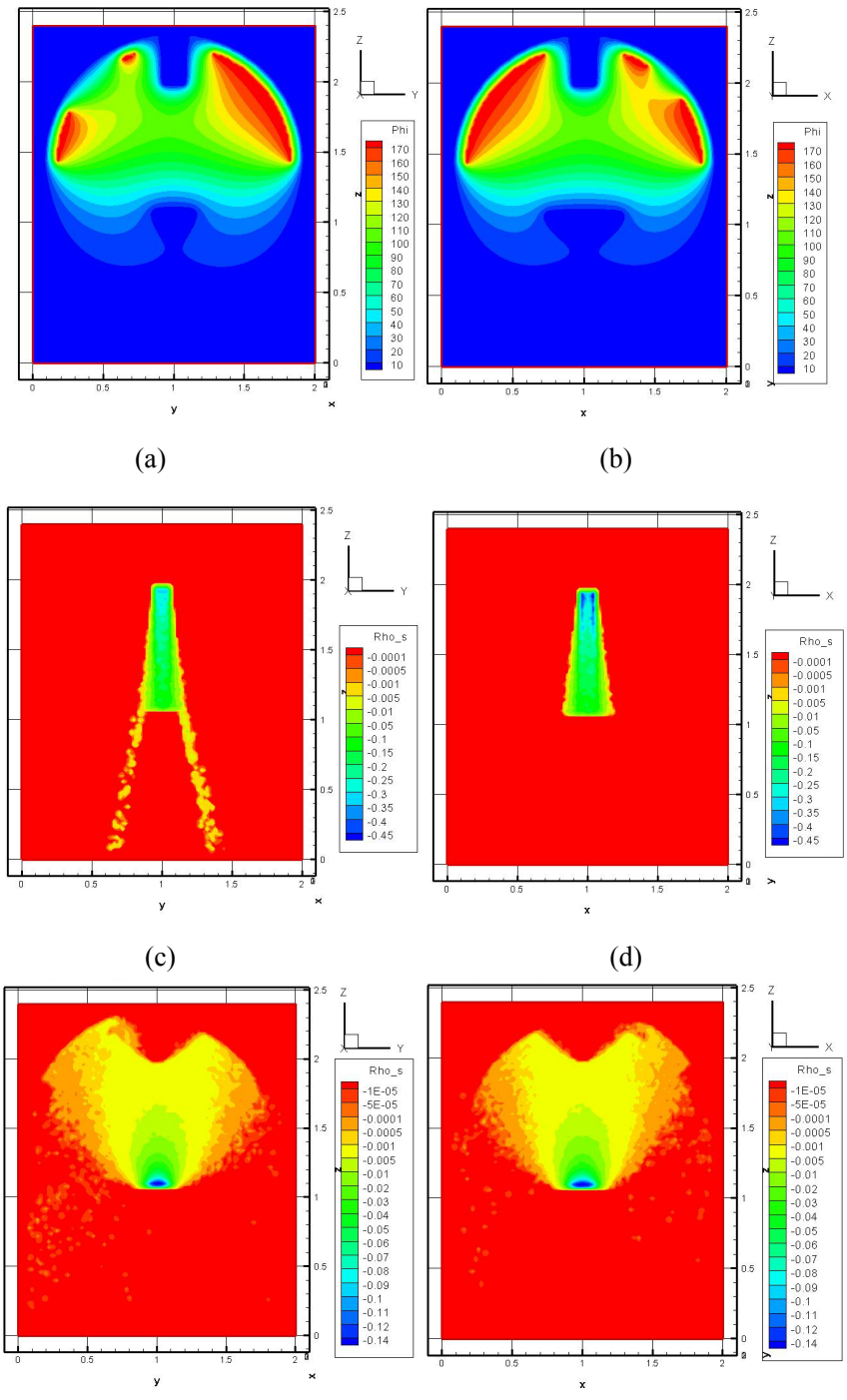

(a) (b)

(c) (d)

(e) (f)

Figure 5.12 Potential and charge density contour at steady state

(Inner shell potential 18V, primary electron beam energy 30eV)

(a) Potential contour of plane x=1.0 through the center of two large holes (hole 1 and hole 3)

(b) Potential contour of plane y=1.0 through the center of hole 2 and hole 3

(c) Charge density contour of primary electrons on plane x=1.0 through the center of large holes 1,3

(d) Charge density contour of primary electrons on plane y=1.0 through the center of hole 2, 3

(e) Charge density contour of secondary electrons on plane x=1.0 through the center of large holes (hole 1 and hole 3)

(f) Charge density contour of secondary electrons on plane y=1.0 through the center of hole 2, 3

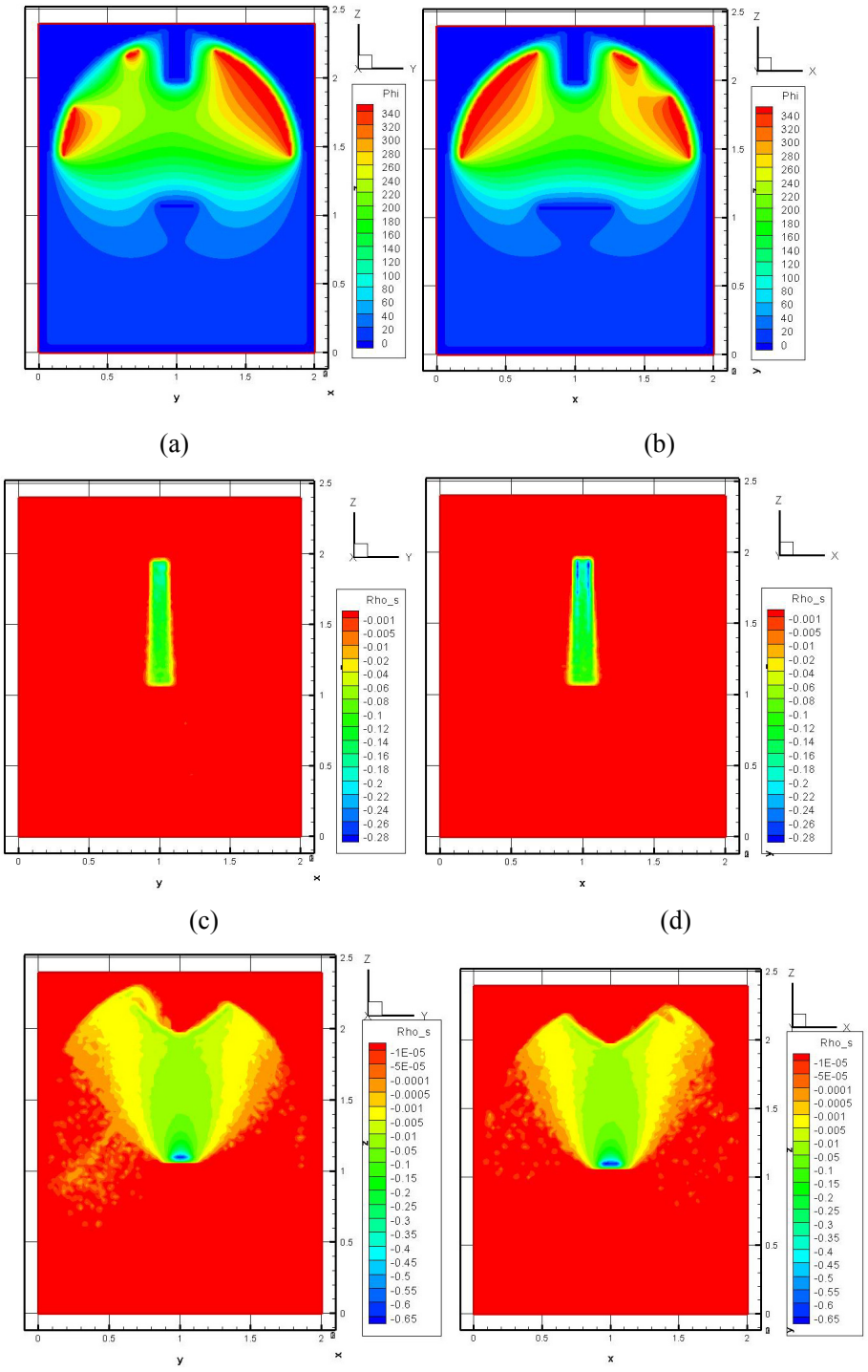

(a) (b)

(c) (d)

(e) (f)

Figure 5.13 Potential and charge density contour at steady state

(Inner shell potential 36V, primary electron beam energy 100eV)

(a) Potential contour of plane x=1.0 through the center of two large holes (hole 1 and hole 3)

(b) Potential contour of plane y=1.0 through the center of hole 2 and hole 3

(c) Charge density contour of primary electrons on plane x=1.0 through the center of large holes 1, 3

(d) Charge density contour of primary electrons on plane y=1.0 through the center of hole 2, 3

(e) Charge density contour of secondary electrons on plane x=1.0 through the center of holes 1,3

(f) Charge density contour of secondary electrons on plane y=1.0 through the center of hole 2, 3

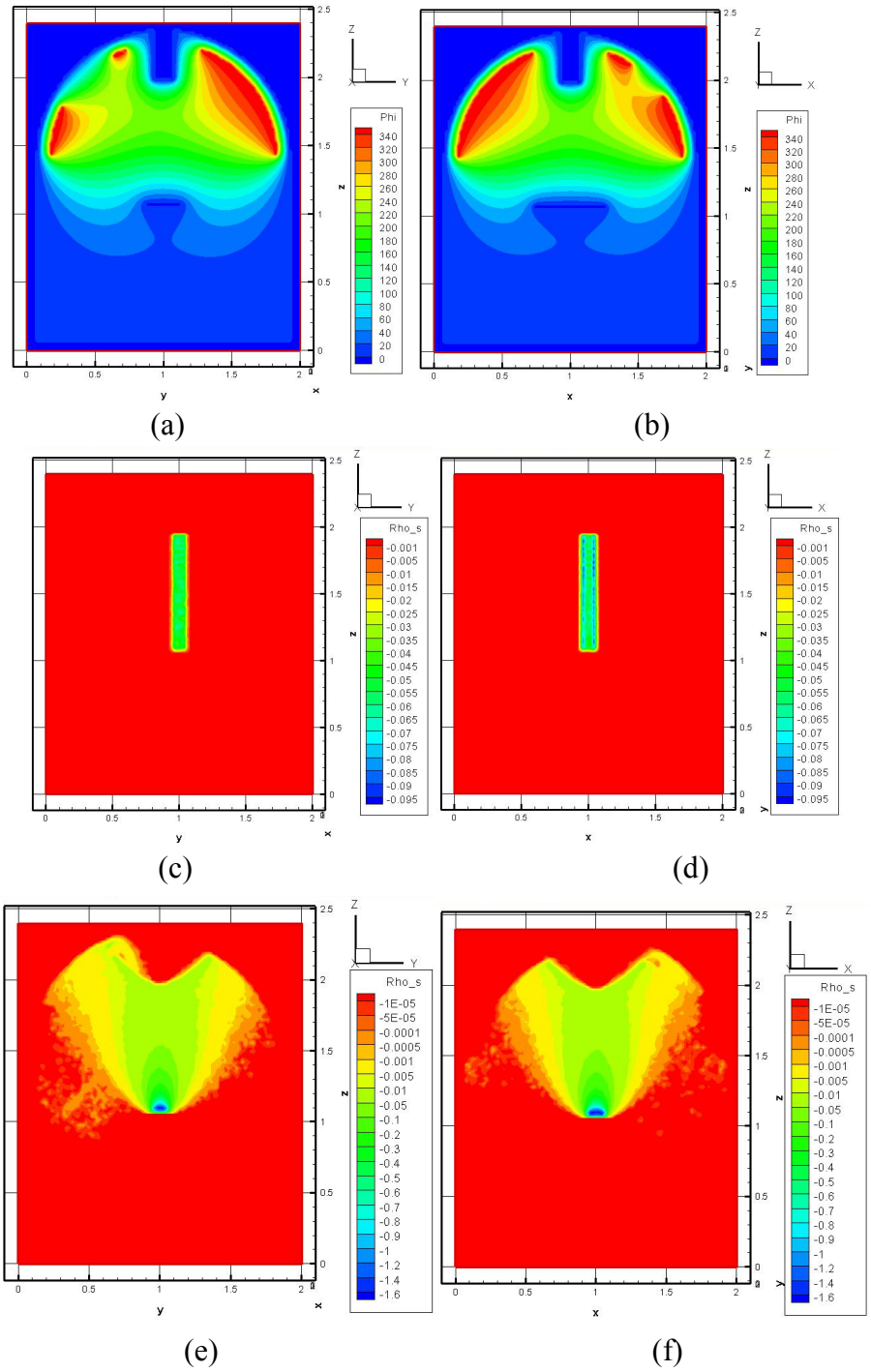

Figure 5.14 Potential and charge density contour at steady state

(Inner shell potential 36V, primary electron beam energy 1000eV)

(a) Potential contour of plane x=1.0 through the center of two large holes (hole 1 and hole 3)

(b) Potential contour of plane y=1.0 through the center of hole 2 and hole 3

(c) Charge density contour of primary electrons on plane x=1.0 through the center of holes 1, 3

(d) Charge density contour of primary electrons on plane y=1.0 through the center of holes 2, 3

(e) Charge density contour of secondary electrons on plane x=1.0 through the center of two large holes 1, 3

(f) Charge density contour of secondary electrons on plane y=1.0 through the center of holes 2, 3

Table 5.5: Proportion of primary electrons collection

Conditions	Target Plate	Inner shell	Chamber Bottom and Wall	Chamber through the holes	Electron Gun	Total absorbed
5V 5eV	77.16%	0	22.84%	0	0	100%
9V 10eV	88.12%	0	11.88%	0	0	100%
13.5V 15eV	93.11%	0	6.89%	0	0	100%
18V 20eV	95.10%	0	4.90%	0	0	100%
18V 30eV	97.89%	0	2.11%	0	0	100%
36V 100eV	100%	0	0	0	0	100%
36V 1000eV	100%	0	0	0	0	100%

Table 5.6: Proportion of secondary electrons collection

Conditions	Target Plate	Inner shell	Chamber Wall	Chamber through the holes	Electron Gun	Total absorbed
5V 5eV	0	88.58%	0.62%	9.95%	0.84%	100%
9V 10eV	0	90.87%	0.17%	7.86%	1.11%	100%
13.5V 15eV	0	91.67%	0.29%	6.96%	1.08%	100%
18V 20eV	0	92.40%	0.36%	6.02%	1.23%	100%
18V 30eV	0	92.50%	0.32%	6.06%	1.12%	100%
36V 100eV	0	94.25%	0.31%	3.65%	1.79%	100%
36V 1000eV	0	94.42%	0.29%	3.39%	1.90%	100%

Then following parameters are defined to express the secondary electron yield curve:

I_s_t: secondary electrons emitted from the target plate,
I_p_g: primary electrons emitted from the electron gun,
I_p_t: primary electrons hitting the target plate,
I_s_s: secondary electrons collected by the inner shell.

With these parameters, the secondary electron yield is

$$Yield = \frac{I_s\_t}{I_p\_t}$$

We also define other two ratios as

$$Ratio\_1 = \frac{I_s\_s}{I_p\_g}$$

$$Ratio\_2 = \frac{I_s\_s}{I_p\_t}$$

With the design of the facility, the "Ratio 2" is the measured yield in experiments. For different conditions listed in Table 5.4, the simulation results of the yield, ratio 1 and ratio 2, as well as the yield function model using equation (5.5), are shown in Table 5.7 and Figure 5.15. The Ratio 1 is less than the Ratio 2 because the primary electrons emitted by the electron gun are not all collected by the target plate. With the increasing of beam energy, this difference is smaller. Thus, the primary electrons hitting the target plate should be used in the experiment to measure the material yield. Some of the secondary electrons are collected by the facility other than the inner shell, thus, the secondary electrons collected by inner shell is less than the amount emitted from the target plate. The Ratio 2 is less than the yield values. The difference is smaller for larger inner shell potential. In order to apply the secondary electrons collected by inner shell to get the emitted secondary electrons amount in the experiment, the measured yield "Ratio 2" in experiment needs to be adjusted based on the difference from the yield result in this simulation. The experiment result is close to the simulation results considering the effects of experiment conditions.

Table 5.7 Secondary electron yield and simulation results

Condition	5V 5eV	9V 10eV	13.5V 15eV	18V 20eV	18V 30eV	36V 100eV	36V 1000eV
Yield	0.0469	0.0892	0.1331	0.1762	0.2753	0.9069	1.3490
Ratio 1	0.0318	0.0719	0.1120	0.1553	0.2526	0.8478	1.3291
Ratio 2	0.0418	0.0813	0.1196	0.1630	0.2561	0.8478	1.3291
Input Model Yield	0.0516	0.1031	0.1544	0.2055	0.3066	0.9548	1.3847

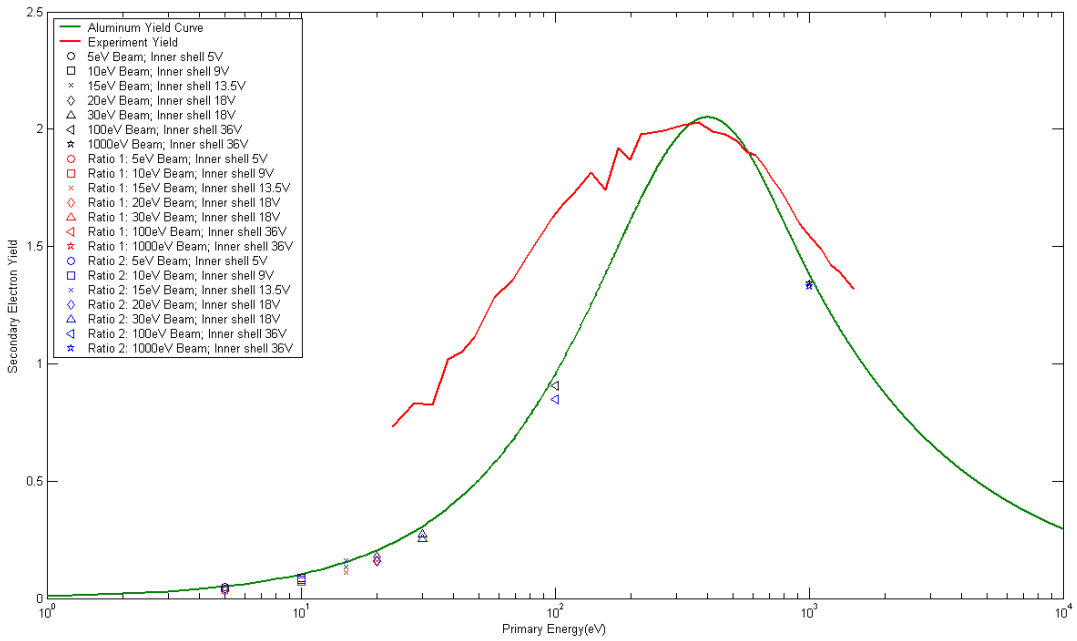

Figure 5.15: Secondary electron yield in simulation and experiment

5.4.3 Secondary Electron Angular Distribution Measurement

In secondary electrons emission, the simulation model obeys the Lambert's cosine law for velocity distribution when the emission source is a small area. In this section, the distribution of secondary electron velocity is examined. The velocity distribution of plane source emission is also compared with Lambert's cosine law.

For a point source secondary electrons emission in free space without experiment facility, we have the electron flux

$$dn = \frac{N_0}{\pi} \cos\theta \sin\theta d\theta d\phi, \tag{5.16}$$

where the solid angle and flux is $d\omega=\sin\theta d\theta d\phi$ and N_0 is the total particle flux. We can get

$$\frac{dn}{d\omega}=\frac{N_0}{\pi}\cos\theta\,. \tag{5.19}$$

Use x axis as the electrons emission surface, y axis as the normal direction, and define the position of the curve point has θ angle from y axis. The length from original point to the curve point is defined as the magnitude of the flux in θ direction. The flux changing with θ at $\phi=\pi/4$ is shown in Figure 5.16 (a). Figure 5.16(b) shows the flux vs. θ plot. The simulation results using the model in section 5.3.4 is closed to the analytical result.

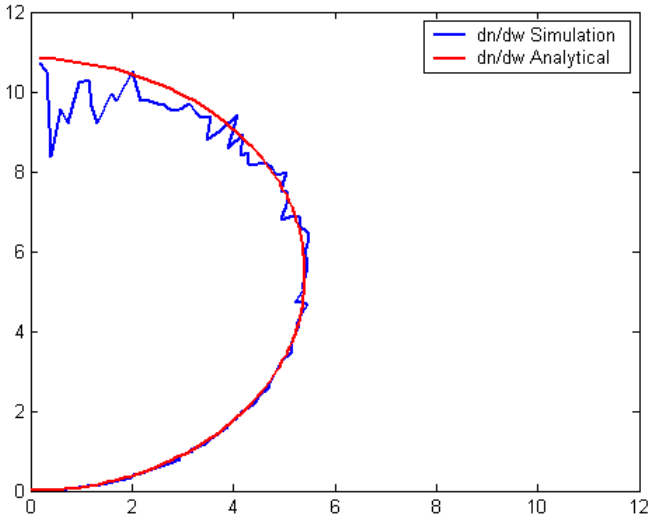

(a)

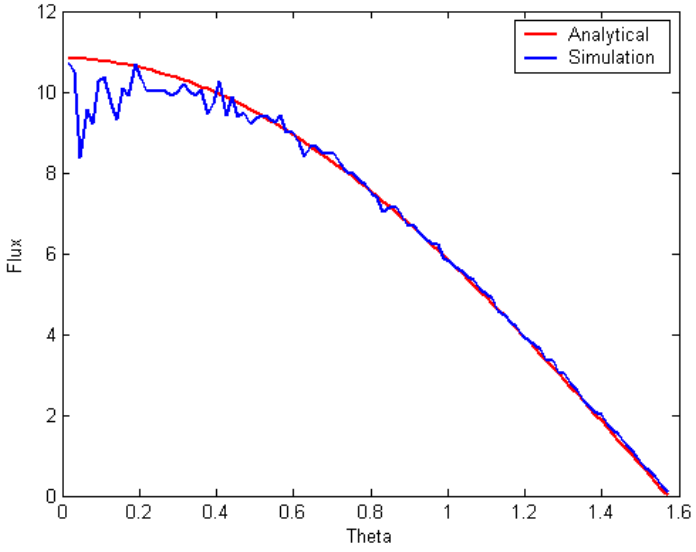

(b)

Figure 5.16 Flux distributions on cosine law

If we consider the ring element for different θ value, for certain θ, we count the flux for ϕ from 0 to 2π and get the total flux in this ring element. Then the flux in this ring element should be

$$dn_\theta = 2N_0 \cos\theta \sin\theta d\theta . \tag{5.18}$$

Using the same definition of the x and y coordinates as that in Figure 5.16(a), we can plot the flux distribution for the ring element with different θ, shown in Figure 5.17 (a). The plot of Figure 5.17(b) is the flux vs. θ plot.

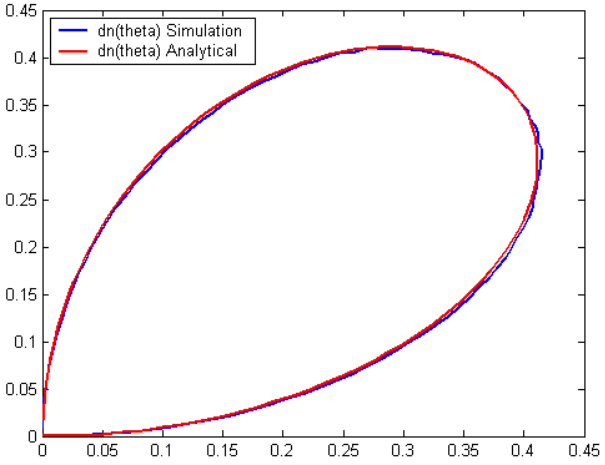

(a)

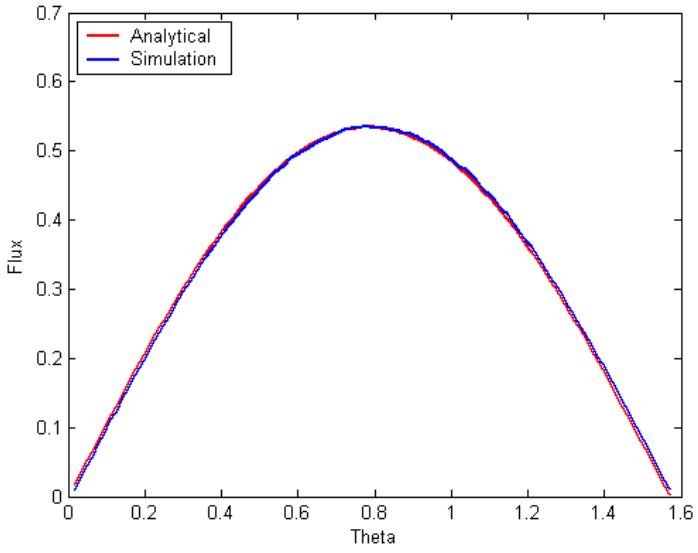

(b)

Figure 5.17 Flux distributions for ring element

If the electrons are emitted from a plane surface, the angular distribution may not obey the cosine law near the emission plate. We simulate the secondary electrons emitted uniformly at the surface of a 5cm×10cm plate and the flux is investigated at the semi-spheres with radius 7cm and 14cm which has the same center of the plate. For the semi-sphere with 7cm radius, the flux changing with θ at $\phi = \pi/4$ is plotted in Figure 5.18(a). The flux in ring element changing with θ is shown in Figure 5.18 (b). Same plots for semi-sphere with 14cm radius are shown in Figure 5.19. For electrons with plane emission, the angular distribution doesn't obey cosine law near the plate surface. The distribution is approaching the cosine law far away from plate because with this condition the plane surface is approximately a point source.

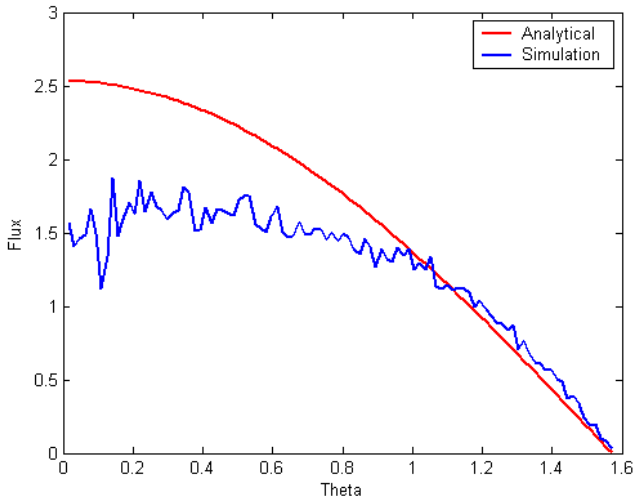

(a)

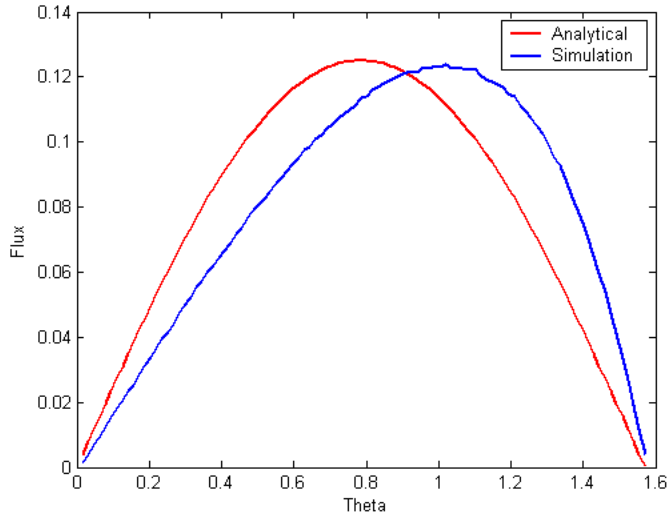

(b)

Figure 5.18 Flux distributions at semi-sphere with radius 7cm

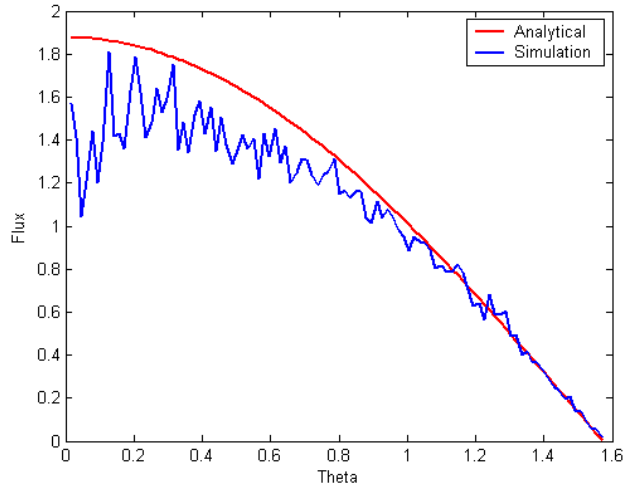

(a)

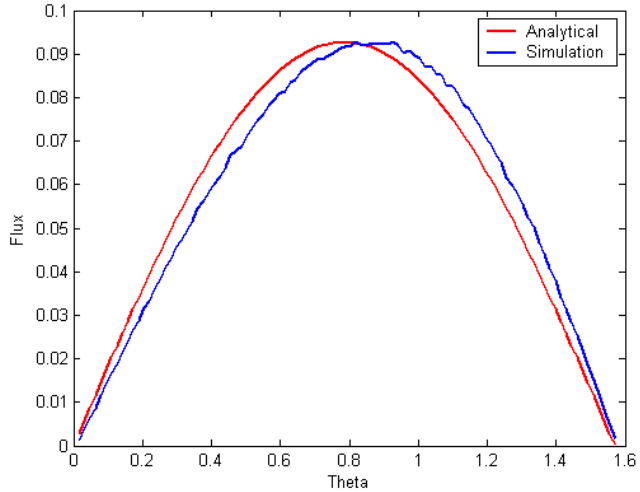

(b)

Figure 5.19 Flux distributions at semi-sphere with radius 14cm

5.4.4 Secondary Electron Yield at High Primary Electron Beam Current Density

In this section, the secondary electrons emission with high current density of primary electron beam is studied. To avoid the effect of electrostatic field caused by chamber and inner shell potential, the potential of all facility parts including chamber, inner shell and target plates are fixed to be zero. In section 5.4.3, we get the conclusion that the point source secondary electron emission obeys the cosine law and the plate

source emission only obeys the cosine law far away from the plate center. In this section, the radius of electron gun is reduced to be 0.1cm to make a quasi-point impingement on the target plate. This will make the secondary electron emission as point source emission.

There are three cases considered which are differentiated by the primary electron beam current density. The primary electron beam parameters for these three cases are listed in Table 5.8.

Table 5.8 Primary electron beam parameters for different current density cases in secondary electron emission experiments

Current density cases	High	Normal	Low
Current density (A/m^2)	10^{-2}	10^{-3}	3.185×10^{-5}
Energy (eV)	300	300	300
Drifting velocity v_d (10^7m/s)	1.027	1.027	1.027
Thermal velocity v_{th} (10^5m/s)	1.326	1.326	1.326
Number density n ($10^7/m^3$)	608.57	60.857	1.938

For all these cases, the secondary electrons emission is governed by yield function (5.5). The energy is in Maxwellian distribution and the angular distribution obeys cosine law. The secondary electron current is count on a 'virtual' diagnostic ring surface to look at angular distribution of secondary electrons. The center of this virtual ring is the same as the plate center and the radius is 7cm. The measurement range is defined by the angle from the normal direction of the surface from 25° to 90°. The flux on the diagnostic surface is output every 5°. The particles are count through a surface element with a radius 3mm, shown in Figure 5.20. In experiment, a sensor is used to measure the flux at each output position as the facility shown in Figure 5.21.

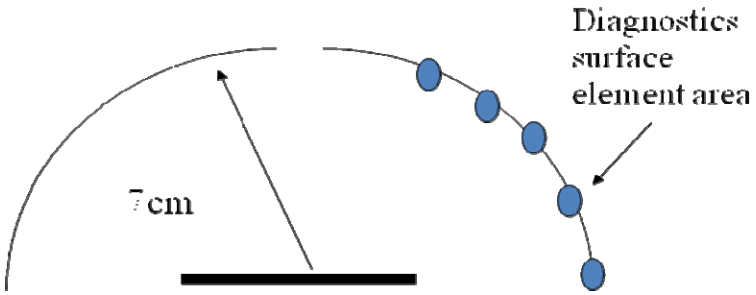

Figure 5.20: The measurement surface of secondary electron flux

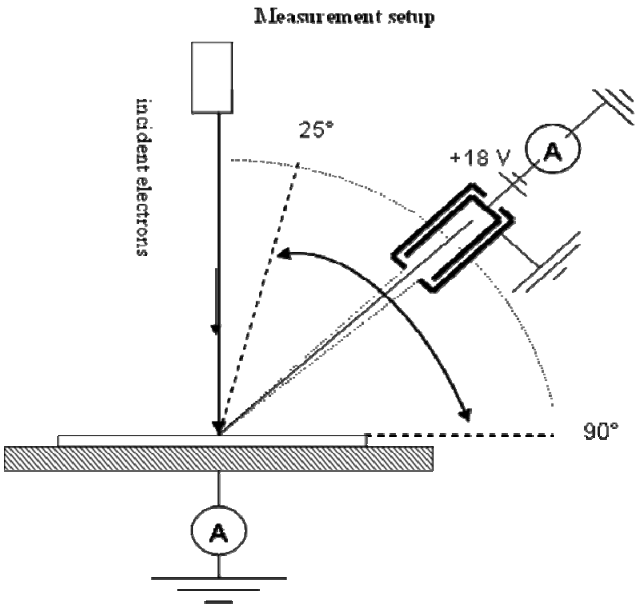

Figure 5.21: Measurement setup in experiment

For "low" primary beam current density which is $3.185\times10^{-5}A/m^2$, the primary electron beam is emitted in a radius of 0.1cm. When hitting the target plate, the primary electrons induce the secondary electrons emission like a source point. Using the same coordinate definition as Figure 5.16(a), consider x axis as the electrons emission surface, y axis as the normal direction, and the position of the curve point has θ angle from y axis. The length from original point to the curve point is defined as the magnitude of the flux in θ direction. We can get the angular distribution of secondary electrons which obeys the cosine law, shown in Figure 5.22.

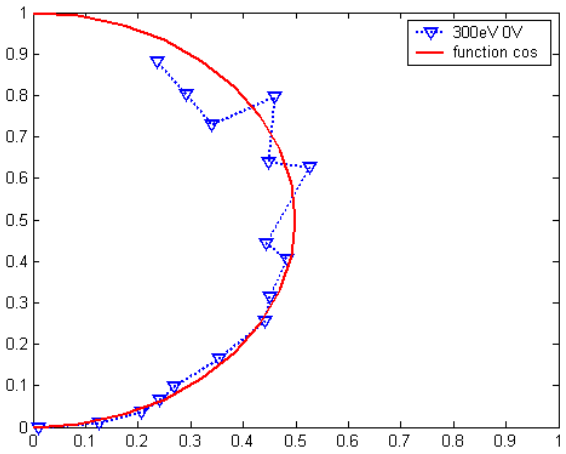

Figure 5.22: Angular distribution of secondary electrons for low primary beam density (Primary beam energy 300eV density $3.185\times10^{-5}A/m^2$, target plate potential 0V, normalized by N_0/π)

Figure 5.23 shows the potential and charge density profiles for primary electrons and secondary electrons. The potential distribution in the domain is caused by the space charge. Figure 5.24 shows the potential and charge density in z direction along the center of plate (x=1.0 and y=1.0). The maximum charge density absolute value is at the plate surface and the maximum potential absolute value is at a small distance above the plate surface. The trajectory of primary electrons is almost a straight line to approach the plate surface and the secondary electrons are emanative from the emission source. This will make the charge density have a maximum value on the plate surface.

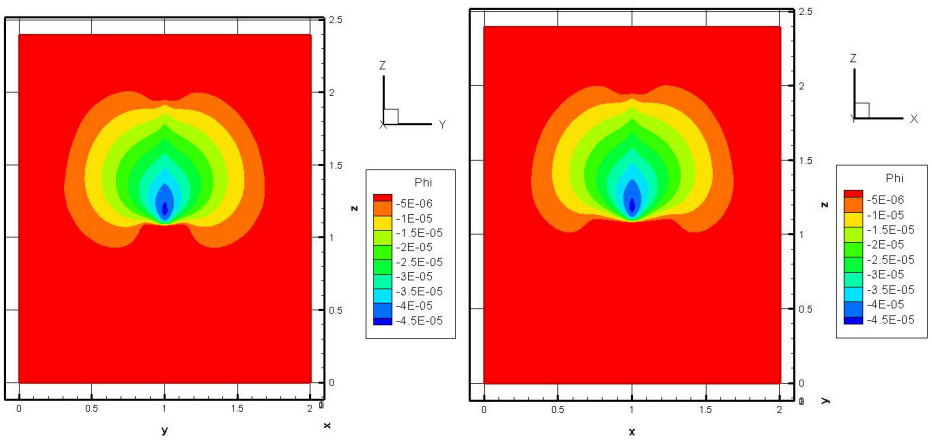

(a) (b)

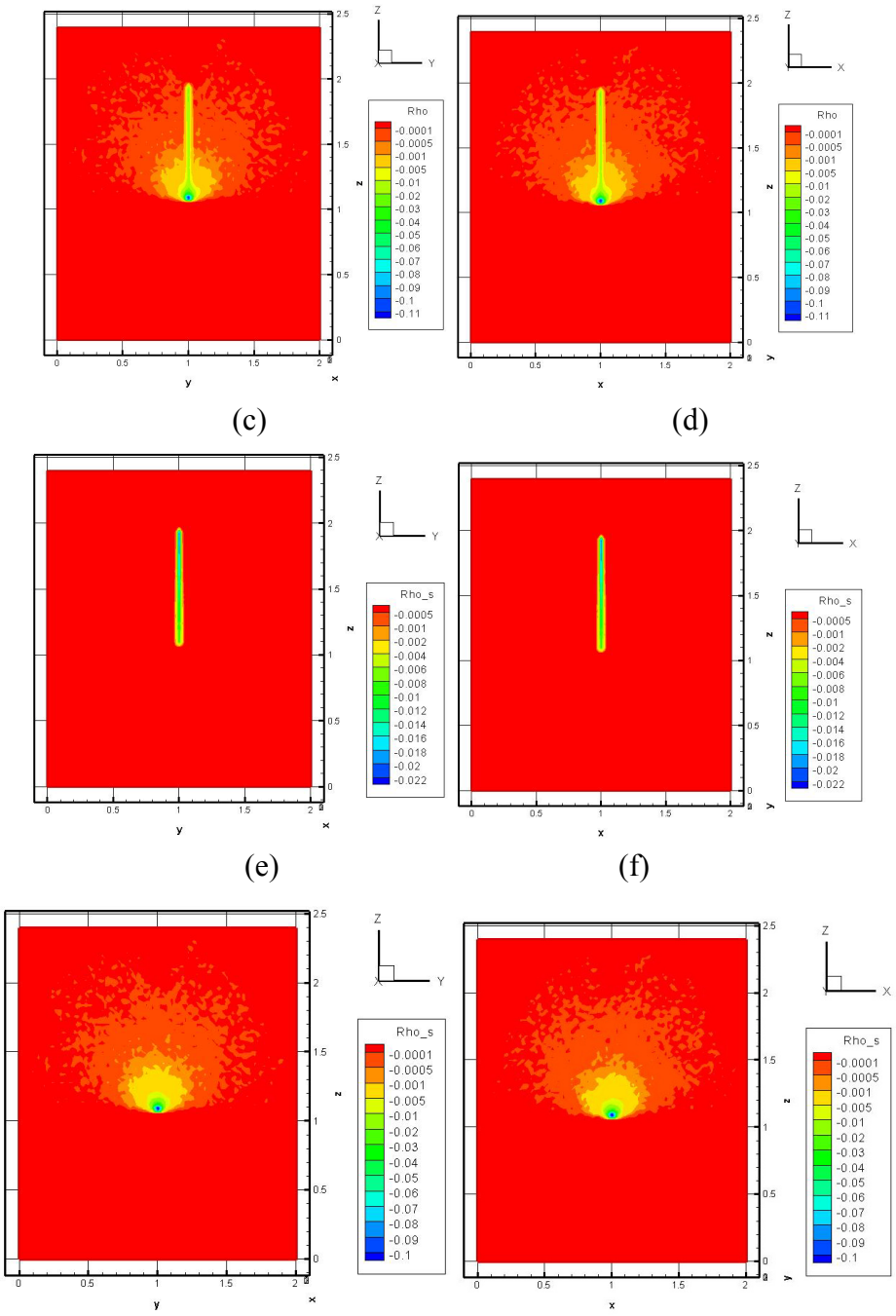

Figure 5.23 Potential and charge density contour for low primary beam density

(Primary beam energy 300eV density $3.185\times10^{-5}A/m^2$, target plate potential 0V)

(a) Potential contour of plane x=1.0 through the center of holes 1, 3; (b) Potential contour of plane y=1.0 through the center of holes 2, 3; (c) Total charge density contour on plane x=1.0 through the center of two large holes 1, 3; (d) Total charge density contour on plane y=1.0 through the center of hole 2 and hole 3; (e) Charge density contour of primary electrons on plane x=1.0 through the center of holes 1, 3; (f) Charge density contour of primary electrons on plane y=1.0 through the center of holes 2, 3; (g) Charge density contour of secondary electrons on plane x=1.0 through the center of holes 1, 3; (h) Charge density contour of secondary electrons on plane y=1.0 through the center of hole 2, 3

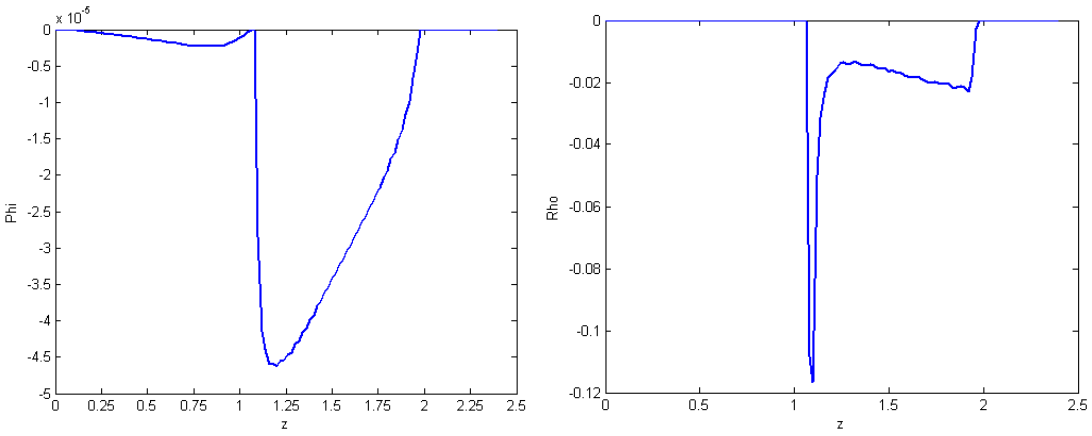

Potential Charge density

Figure 5.24 Potential and Charge density in z direction along the center of the plate
(Primary beam energy 300eV density 3.185×10^{-5}A/m^2, target plate potential 0V,
the plate surface is at z=1.08 and the electron gun exit is at z=1.98)

For "normal" primary beam current density which is 10^{-3}A/m^2, the primary electron beam is emitted in a radius of 0.1cm. Using the same coordinate definition as Figure 5.22, the angular distribution of secondary electrons which obeys the cosine law is shown in Figure 5.25 (a). Here the curve is fit to a function with form like

$$flux = A(\cos\theta)^n$$

where A and n are constants. For the simulation results, the fitting function is

$$flux = 6.44708\times10^{-5}(\cos\theta)^{0.95}$$

The curve in Figure 5.25(a) is normalized with 6.44708×10^{-5} to make the flux value at θ =0 to be unit value. Figure 5.25 (b) shows the fitting flux curve with the same definition in experiment. It is also consistent with the cosine law. These results verify the cosine law of velocity distribution in secondary electrons emission, as well as the consistent of the simulation and experiment results.

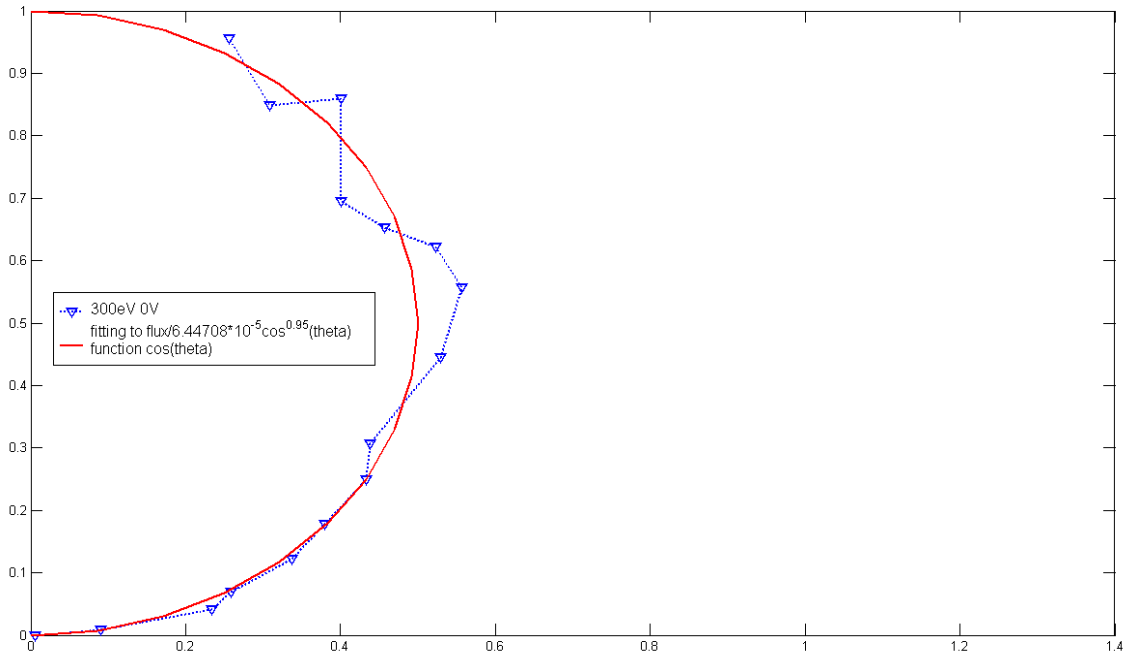

(a)

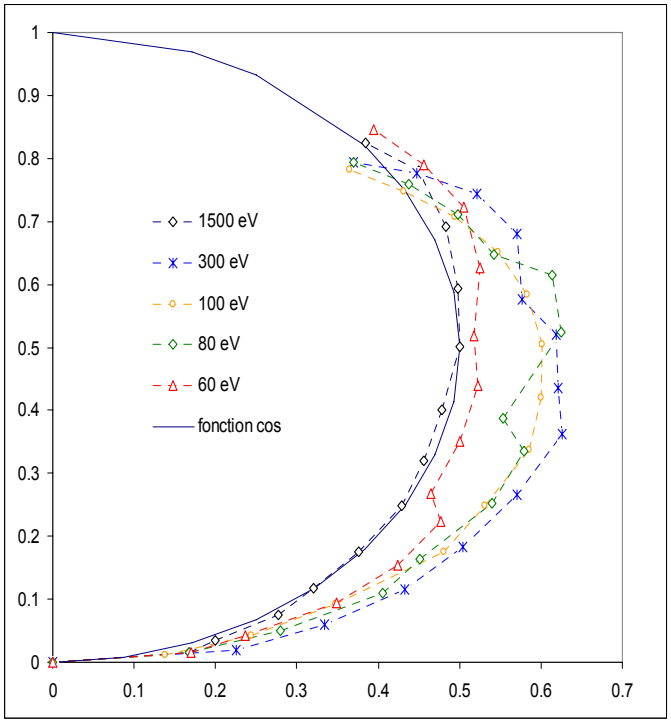

(b)

Figure 5.25: Angular distribution of secondary electrons
for 'normal' primary beam density
(Primary beam energy 300eV density 10^{-3}A/m^2, target plate potential 0V)
(a) Simulation result; (b) Experiment result

For "high" primary beam current density which is $10^{-2}A/m^2$, the primary electron beam is emitted in a radius of 0.1cm and the beam energy is 300eV. Three cases are considered with different target plate potential, 0V, +6V and -6V.

For the case with target plate potential 0V, the potential and charge density at steady state is shown in Figure 5.26. Compared with Figure 5.23, the secondary electron density and potential magnitude is larger when the primary electron beam current density increases.

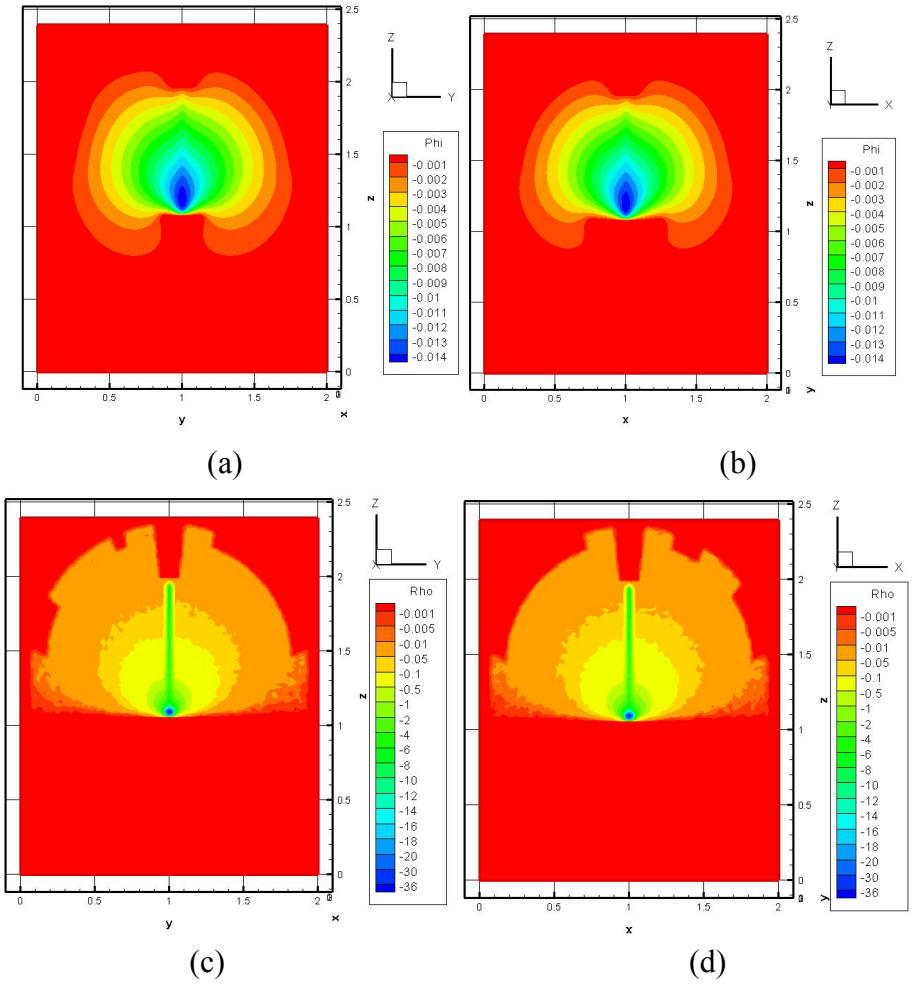

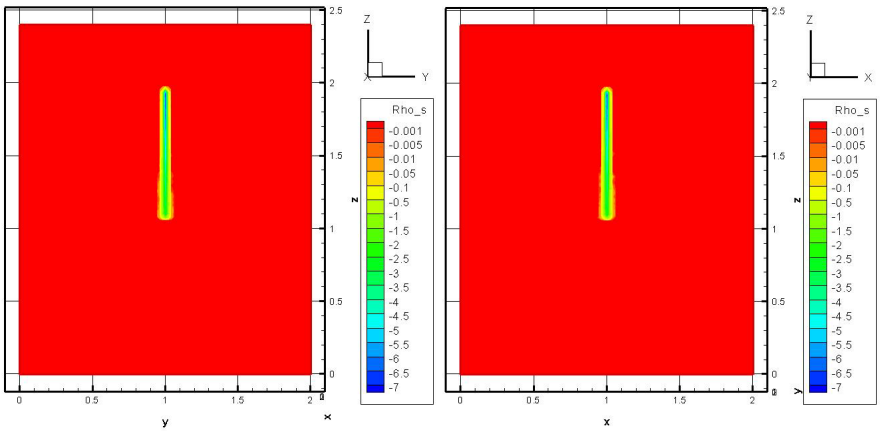

(e) (f)

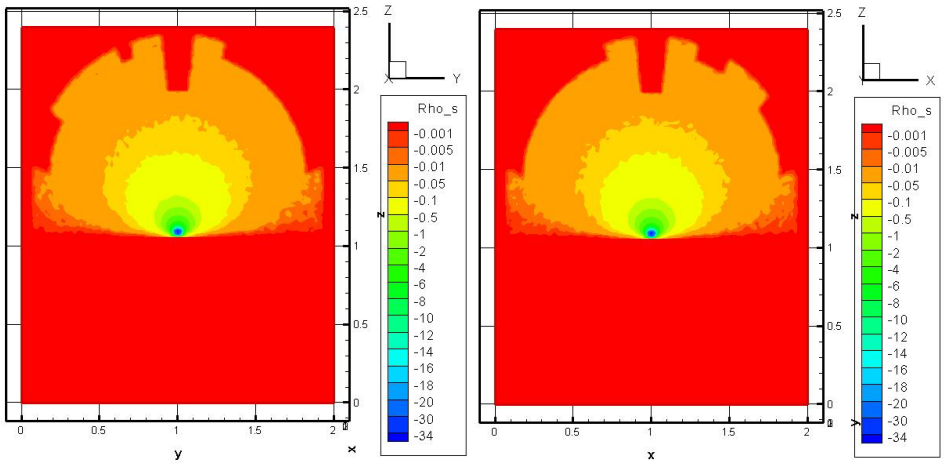

(g) (h)

Figure 5.26 Potential and charge density contour for high primary beam density

(Primary beam energy 300eV density10^{-2}A/m^2, target plate potential 0V)

(a) Potential contour of plane x=1.0 through the center of two large holes 1, 3; (b) Potential contour of plane y=1.0 through the center of hole 2, 3; (c) Total charge density contour on plane x=1.0 through the center of two large holes 1, 3; (d) Total charge density contour on plane y=1.0 through the center of holes 2, 3; (e) Charge density contour of primary electrons on plane x=1.0 through the center of large holes 1, 3; (f) Charge density contour of primary electrons on plane y=1.0 through the center of holes 2, 3; (g) Charge density contour of secondary electrons on plane x=1.0 through the center of large holes 1, 3; (h) Charge density contour of secondary electrons on plane y=1.0 through the center of holes 2, 3.

For the case with target plate potential -6V (-60 after normalization), the potential and charge density at steady state is shown in Figure 5.27. Compared with Figure 5.26, the target plate affects the potential profile in the chamber seriously and further affects the movement of the electrons. The secondary electron emission obeys the cosine law. However, the distribution at certain distance to the plate center doesn't show the cosine law because of the target plate potential effect. This can be observed from the secondary electron charge density contour. The potential and charge density in z direction along the center of plate (x=1.0 and y=1.0) is shown in Figure 5.28. The

region near the plate has low potential and charge density.

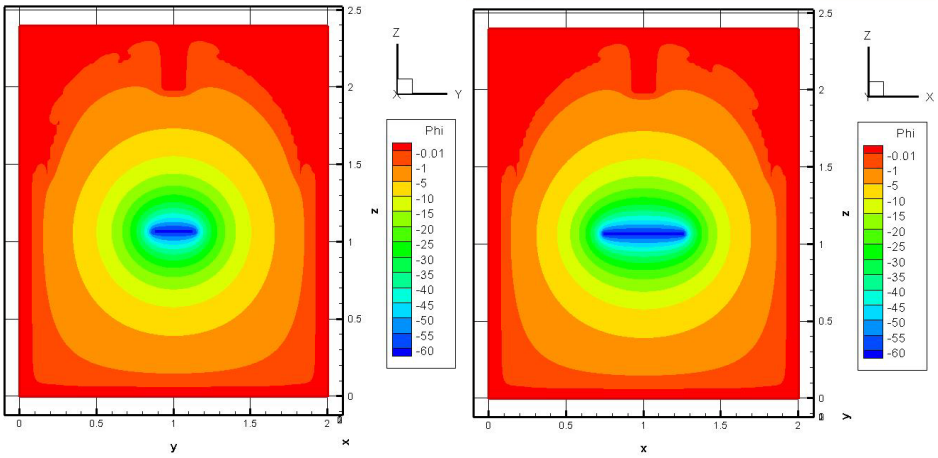

(a) (b)

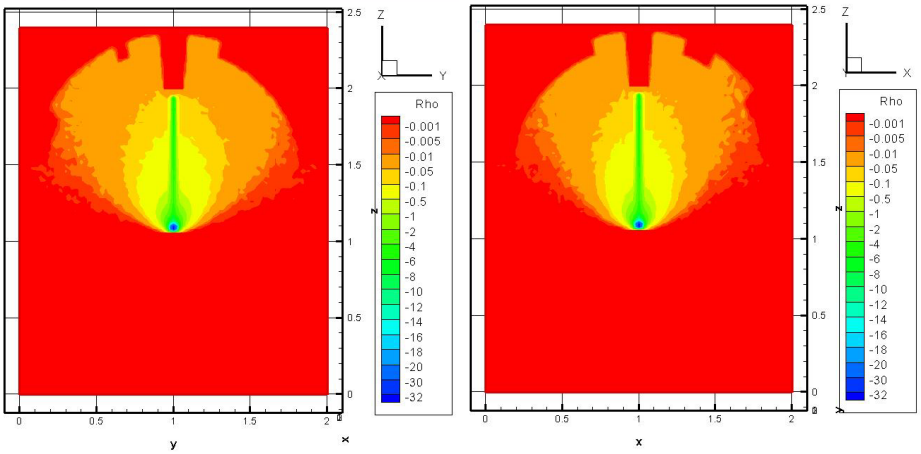

(c) (d)

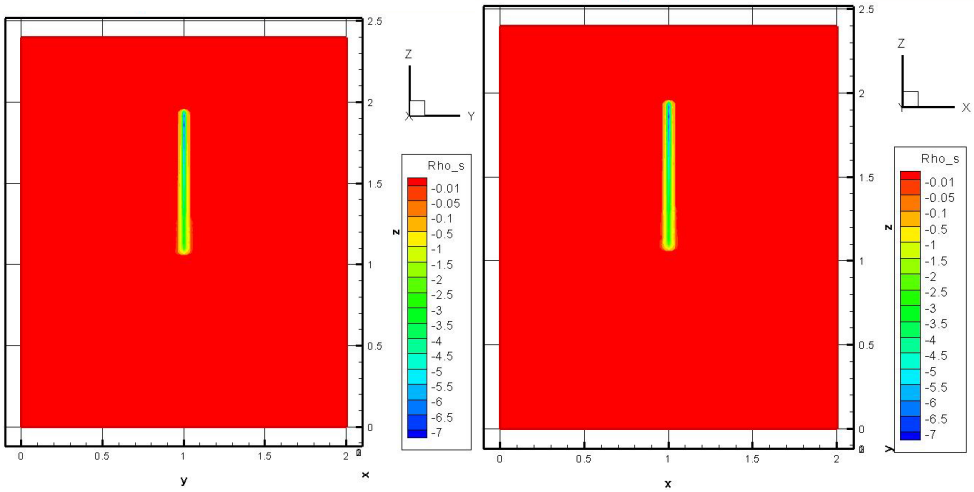

(e) (f)

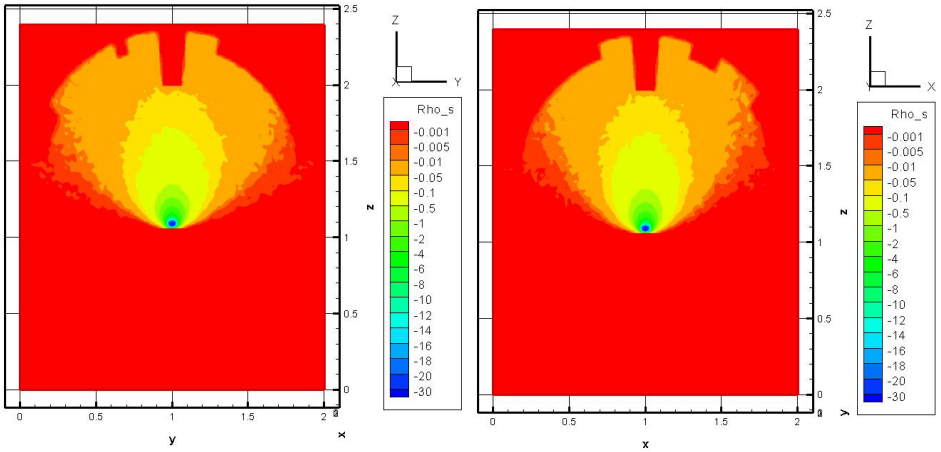

(g) (h)

Figure 5.27 Potential and charge density contour for high primary beam density
(Primary beam energy 300eV density $10^{-2}A/m^2$, target plate potential -6V)

(a) Potential contour of plane x=1.0 through the center of two large holes 1, 3; (b) Potential contour of plane y=1.0 through the center of holes 2, 3; (c) Total charge density contour on plane x=1.0 through the center of two large holes 1, 3; (d) Total charge density contour on plane y=1.0 through the center of holes 2, 3; (e) Charge density contour of primary electrons on plane x=1.0 through the center of large holes 1, 3; (f) Charge density contour of primary electrons on plane y=1.0 through the center of holes 2, 3; (g) Charge density contour of secondary electrons on plane x=1.0 through the center of large holes 1, 3; (h) Charge density contour of secondary electrons on plane y=1.0 through the center of holes 2, 3

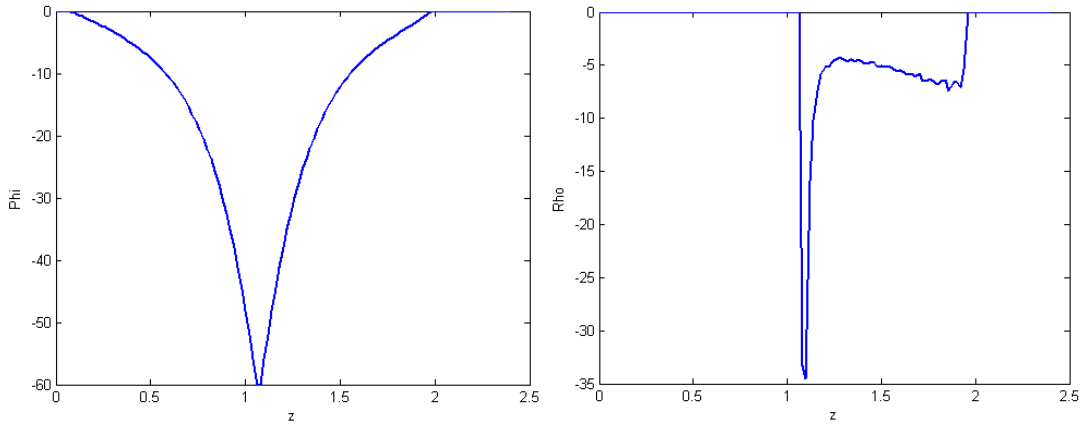

Potential Charge density

Figure 5.28 Potential and Charge density in z direction along the center of the plate
(Primary beam energy 300eV density $10^{-2}A/m^2$, target plate potential -6V,
the plate surface is at z=1.08 and the electron gun exit is at z=1.98)

For the case with target plate potential +6V (+60 after normalization), some emitted secondary electrons are collected by the target plate. About 90% secondary electrons will be collected by target plate. These collected secondary electrons also induce the new secondary electrons from the target plate. The secondary electrons trajectories present different types after emission. Some are moving towards the inner shell and absorbed. Some are moving upwards but reverse the direction and then collected by the target plate. Some are moving upwards then reverse direction and move below the target plate and collected by the lower side of the plate. Then new secondary electrons will be emitted from the lower side of the plate.

The potential and charge density at steady state is shown in Figure 5.29. Compared with Figure 5.27, because some secondary electrons are absorbed by plate and new secondary electron emission, there are some secondary electrons under the plate. The potential and charge density in z direction along the center of plate (x=1.0 and y=1.0) is shown in Figure 5.30.

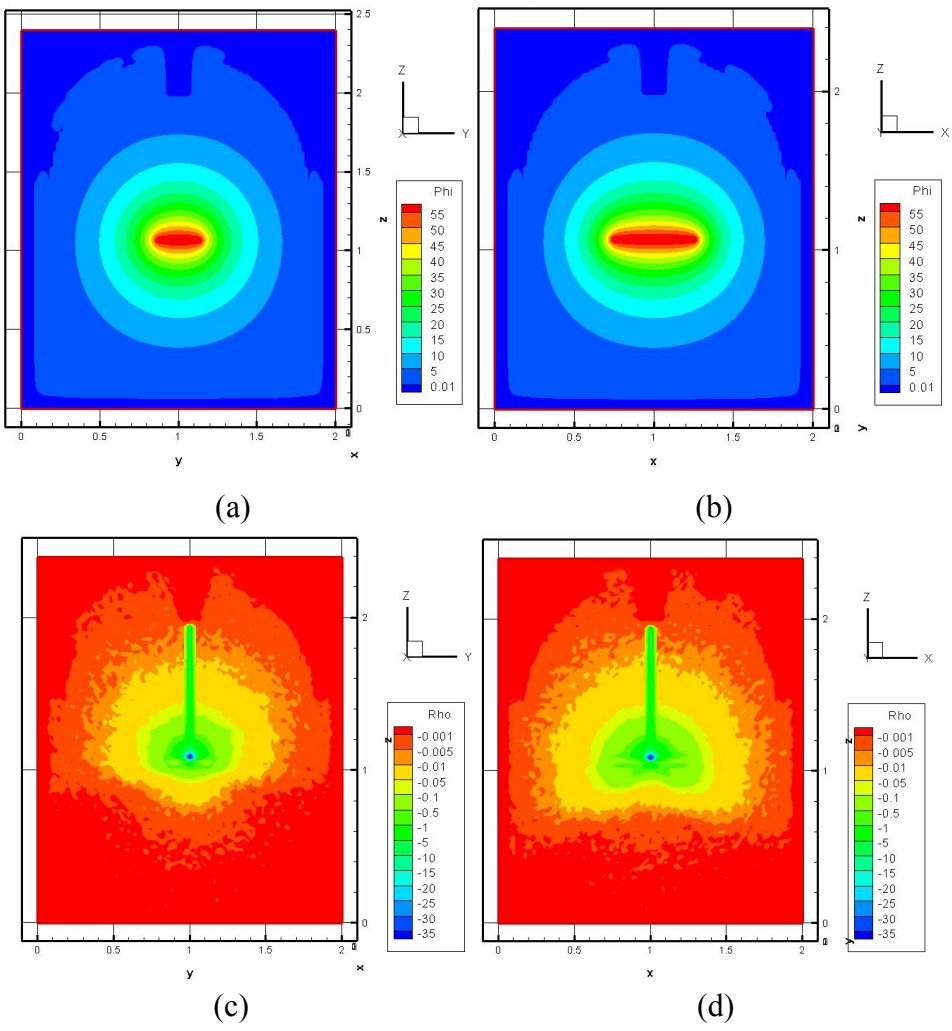

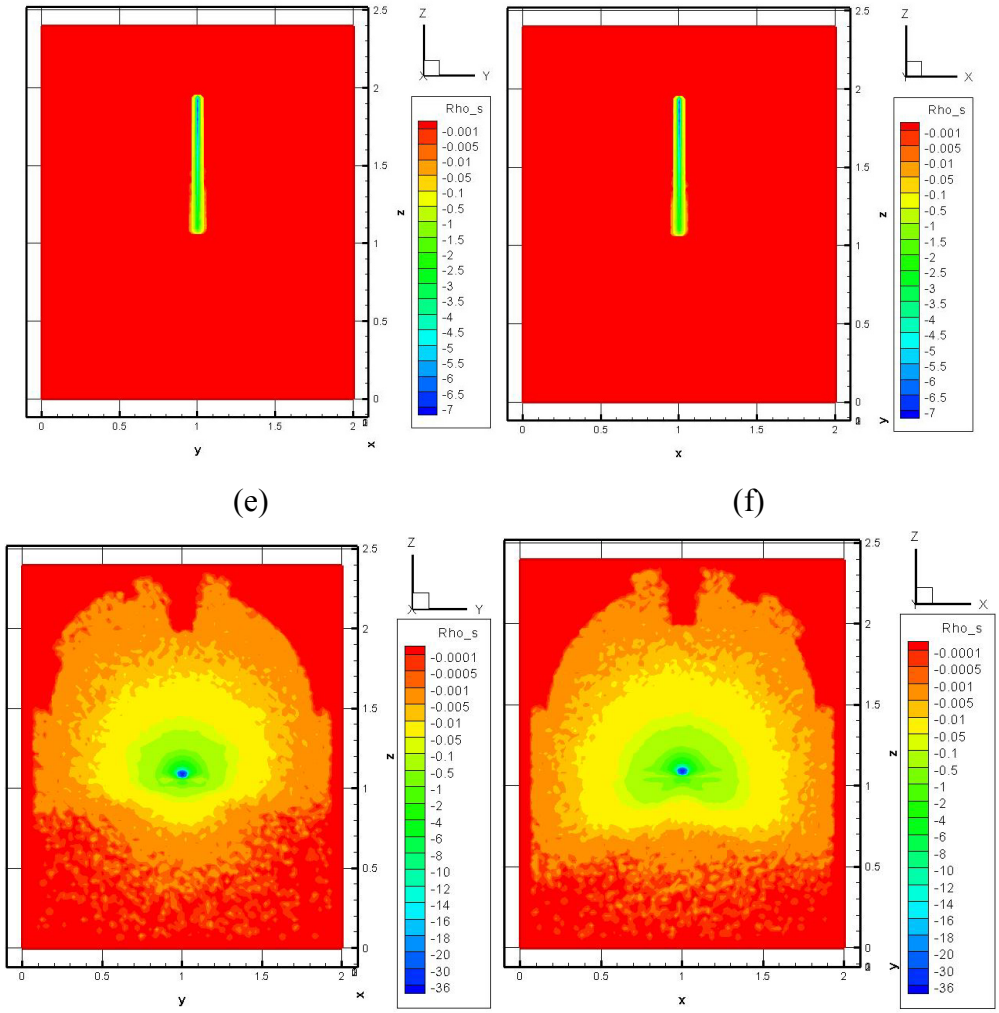

(e) (f)

(g) (h)

Figure 5.29 Potential and charge density contour for high primary beam density

(Primary beam energy 300eV density 10^{-2}A/m^2, target plate potential +6V)

(a) Potential contour of plane x=1.0 through the center of two large holes 1, 3; (b) Potential contour of plane y=1.0 through the center of holes 2, 3; (c) Total charge density contour on plane x=1.0 through the center of two large holes 1, 3; (d) Total charge density contour on plane y=1.0 through the center of holes 2, 3; (e) Charge density contour of primary electrons on plane x=1.0 through the center of large holes 1, 3; (f) Charge density contour of primary electrons on plane y=1.0 through the center of holes 2, 3; (g) Charge density contour of secondary electrons on plane x=1.0 through the center of large holes 1, 3; (h) Charge density contour of secondary electrons on plane y=1.0 through the center of holes 2, 3

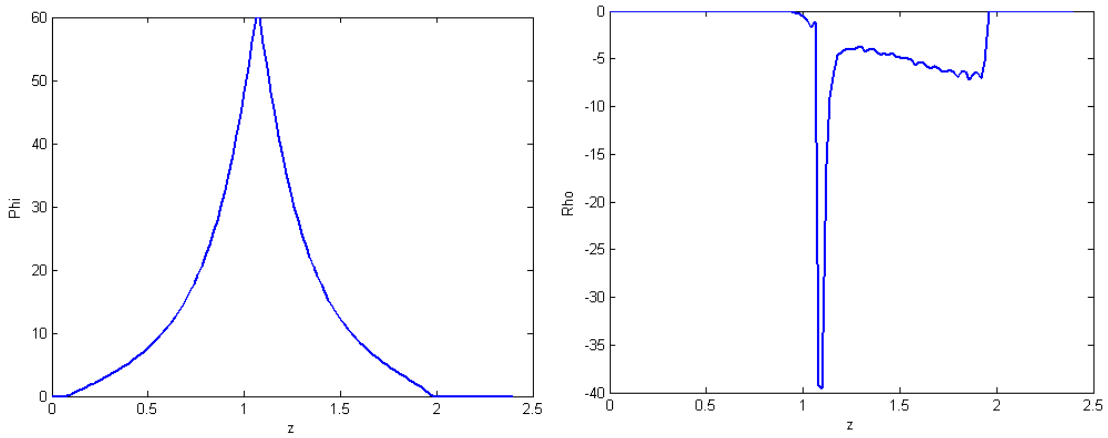

Potential Charge density

Figure 5.30 Potential and Charge density in z direction along the center of the plate
(Primary beam energy 300eV density 10^{-2}A/m^2, target plate potential +6V,
the plate surface is at z=1.08 and the electron gun exit is at z=1.98)

The potential of target plate affects the distribution of secondary electron. The positive potential plate attracts the secondary electrons and the negative potential plate repells the secondary electrons. Their distribution doesn't obey the cosine law any more as that shown in Figure 5.31.

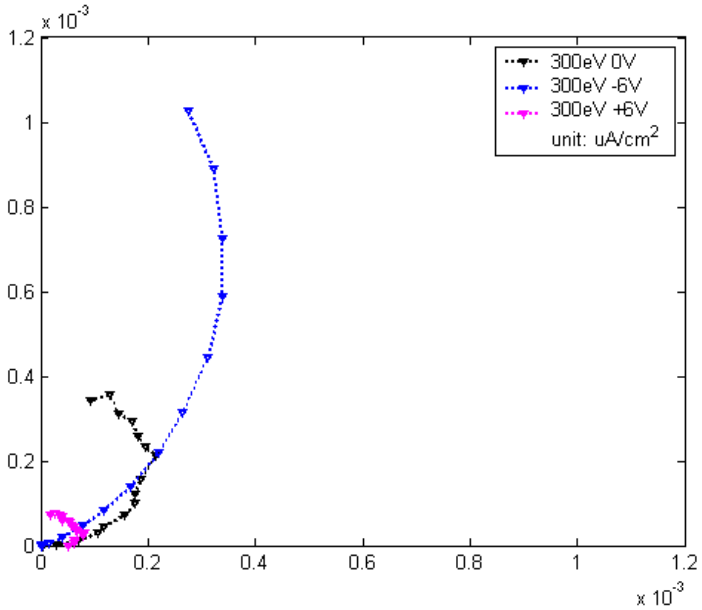

Figure 5.31 Current density for different target plate potential
in high primary current density

5.5 Conclusion

In this chapter, we simulated the secondary electron emission experiments in a vacuum chamber. The IFE-PIC method is validated by comparing with the experiment results. The application only involves boundaries with fixed potentials; hence, the simulation code used is the homogeneous-interface condition IFE-PIC code. This simulation study studied the facility error in the experimental setup and also helped the design of the experiment. It is also verified that the emission of secondary electrons obeys Lambert's cosine law. This can be observed by experiment for single point source emission of secondary electron. For the secondary electrons emitted from a plane, this can't be observed near the source plate. However, the cosine law is approached far away from the source. For primary electron beam with high current density, a point source is generated to emit secondary electron from the target plate. Then the cosine law can be observed in experiment and simulation results. If the plate potential is large and affects the trajectory of emitted secondary electrons, the cosine law is not observed at certain distance from the source although the emission of secondary electron still obeys cosine law.

Chapter 6

Modeling Charging on Lunar Surface

6.1 Introduction

The lunar surface sees a variety of space plasma environment. This chapter studies charging on lunar surface under typical solar wind plasma environment. Specifically we study charging at the lunar polar region. The charging mechanisms considered include the solar wind plasma, the photoelectrons, and secondary electrons. The lunar surface considered includes both a flat surface and non-flat surface model. We also consider a problem involving a simplified spacecraft on lunar surface. This chapter applies the non-homogenous IFE-PIC method to the lunar surface and spacecraft charging problem. We start from the plane lunar surface cases to non-flat surface charging problem. The potential and electric field profiles around the lunar surface are obtained. Then spacecraft is introduced and the potential, plasma density and electric field are investigated to get the circumstance of the lunar surface in the landing area.

6.2 Lunar Surface Charging

The lunar surface and any objects on lunar surface such as dusts or lunar spacecraft are charged due to the impingement of the ambient plasma, emission of the secondary electrons and the photoelectrons under sunlight. The lunar surface potential is

determined by the local current balance condition. The original object of this study is study a lunar surface-spacecraft-dust system such as that shown in Figure 6.1. Modeling of lunar surface charging and dust charging is very challenging problem because the curvature of lunar surface and that of the dust are on very different dimension scales. For dusts packed on surface, it would be difficult and inefficient to generate unstructured mesh to body fit both the surface and the dust. While the goal of lunar surface simulation is to solve both the lunar surface charging and dust charging problems, in this dissertation, we only solve the lunar surface charging problem.

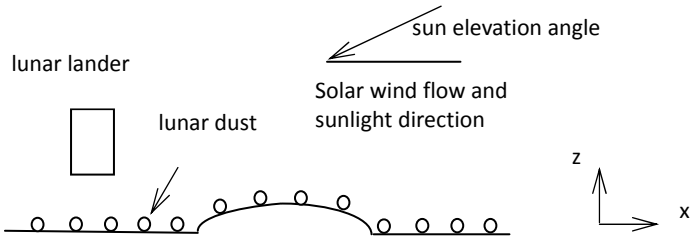

Figure 6.1 Lunar surface setup sketch

The typical average solar wind parameters on the lunar surface at 1AU from the sun are listed in Table 6.1. The plasma flow is mesothermal according to $v_{th,i} \ll v_{sw} \ll v_{th,e}$, where $v_{th,i}$, $v_{th,e}$ are ion and electron thermal velocity.

Table 6.1 Typical solar wind parameters on lunar surface

Solar wind	Number density n_{sw} (cm^{-3})	Flowing velocity v_{sw} (10^7 cm/s)	Thermal velocity v_{th} (10^7 cm/s)	Tempearture T (eV)
Electrons	8.7	4.68	14.5	12
Ions	8.7	4.68	0.31	10

Under normal sunlight incidence, the photocurrent at a distance d (in AU) from the Sun is [54]

$$I_{ph0} = \frac{2.8\times10^9}{d^2}\,\text{electrons/(cm}^2\text{s)}\,, \tag{6.1}$$

which is $I_{ph0} \approx 4.5\mu\text{A/m}^2$ on lunar surface. Hence, for a sun elevation angle α, the number density of the photoelectrons right at the surface is [62]

$$n_{pe0} = \frac{2I_{ph0}\sin(\alpha)}{ev_{t,pe}}, \tag{6.2}$$

where $v_{t,pe}$ is the thermal velocity of photoelectron, α is the sun elevation angle. In this dissertation, we assume that the temperature of the photoelectron is 2.2eV and the energy is stationary Maxwellian distribution. Thus, the number density of photoelectron emission at lunar surface is [7] $n_{pe0} \approx 64\sin\alpha/\text{cm}^3$. In this dissertation, the photoelectrons are emitted using the Lambert's cosine law which is described in section 5.3.5. The photoelectrons play an important role in the plasma sheath and surface charging for the day side region of the lunar surface because the plasma sheath transitions from the photoelectron sheath to the sheath determined by solar wind plasma when the sun elevation angle α decreases. The Debye length $\lambda_{D,ph}=1.37(\sin(\alpha))^{-1/2}$ of photoelectron becomes larger than the solar wind Debye length $\lambda_{D,sw}$ =8.7m when α <1.4º [7]. The parameters of photoelectrons number density at 90º sun elevation angle are listed in Table 6.2. These parameters are used for normalization in the PIC simulation in this chapter.

Table 6.2 Parameters of photoelectrons at 90º sun elevation angle

Number density n (1/cm^3)	64
Temperature T_e (eV)	2.2
Thermal velocity v_{th} (10^7cm/s)	6.2
Debye length λ_D (m)	1.37

Thus the normalized the parameters for both species are

Electron: $\hat{n}_e = 0.1359$, $\hat{T}_e = 5.45$, $\hat{v}_{th,e} = 2.335$, $\hat{v}_{d,e} = 0.7548$,

Ion: $\hat{n}_i = 0.1359$, $\hat{T}_i = 4.55$, $\hat{v}_{th,i} = 0.04976$, $\hat{v}_{d,i} = 0.7548$.

The solar wind and photoelectrons hitting the lunar surface will induce the secondary electron emission. The secondary electron yield function and current density are given by equation 5.5 and 5.8 in section 5.3.3 of Chapter 5.

$$\delta_e(E) = 1.28\,\delta^{\max}\left(\frac{E}{E^{\max}}\right)^{-0.67}\left(1-\exp\left(-1.614\left(\frac{E}{E^{\max}}\right)^{1.67}\right)\right). \tag{5.5}$$

On lunar surface, the parameters are chosen to be δ^{max}=0.89, E^{max}=450eV. The energy of secondary electron is half Maxwellian distribution with temperature 2eV and the angular distribution obeys the Lambert's cosine law.

In the simulation, we choose the lower boundary in z direction of the domain as the lunar surface and the upper boundary in z direction as the infinity away from the lunar surface. The domain size should be large enough to make sure the plasma undisturbed near the upper boundary and the mesh size should be small enough to make the Debye length can be resolved near the lunar surface. In this simulation, the emission of photoelectrons and secondary electrons will left positive charge on the emission surface. The incident electrons and ions left negative and positive charge on the surface separately. These deposited charges provide the flux jump condition on interface for the IFE solver. The PIC simulation is carried out on a slice of the 3D simulation domain with the periodic boundary condition applied in y axis direction.

6.3 Flat Lunar Surface Charging

Wang et al. [26] used finite difference based PIC method to model the flat lunar surface charging. They simulated the flat lunar surface potential and electric field in day-side terminator region with sun elevation angle between 0^o and 10^o. However, the finite difference based PIC method can only solve the flat lunar surface charging problem. The non-flat lunar surface with complex geometry can't be solved. In this section, we will simulate the flat lunar surface charging process and compare the simulation results with Wang et al.'s results. The non-flat lunar surface charging is performed in next section.

Consider the lunar surface as a flat face and neglect the non-flat area. The day-side terminator region is investigated with sun elevation angle between 0^o and 10^o. The potential profile from the lunar surface to certain height for each case is shown in Figure 6.2 for every 2^o in this range. For different elevation angle, the potential profile shows a monotone increasing when height increase. The lunar surface potential values are negative when elevation angle is less than 10^o and this potential value is increasing with the elevation angle increases. This increase is slower near 10^o. Figure 6.3 shows the lunar surface potential as a function of the sun elevation angle. The simulation results using IFE-PIC method are closed to Wang et al.'s results using finite difference based PIC method (FD-PIC) [26].

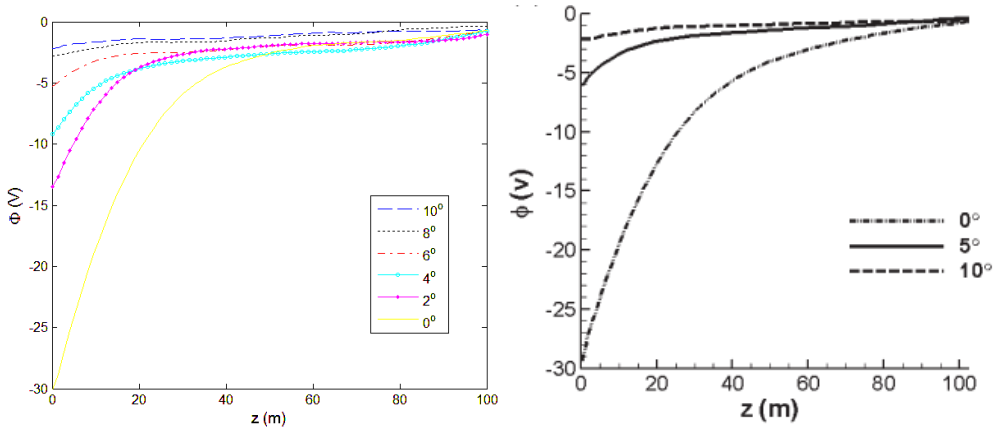

(a) IFE-PIC results (b) FD-PIC results [26]

Figure 6.2 Potential profiles versus distance from lunar surface

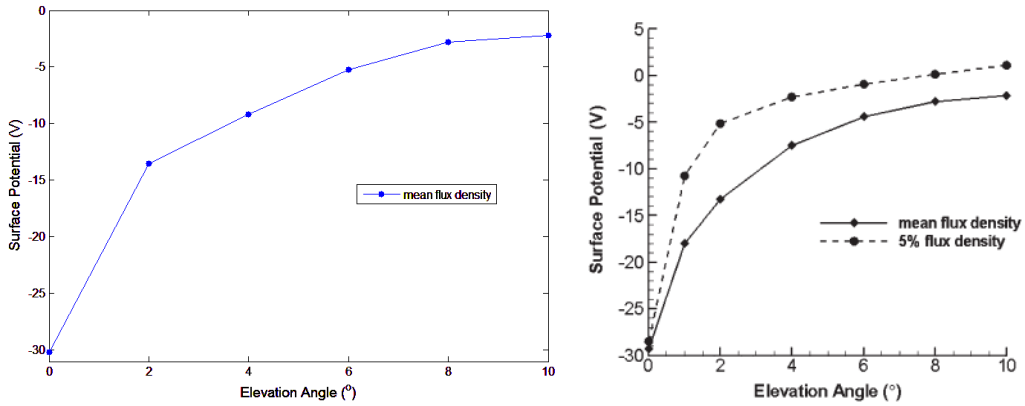

(a) IFE-PIC results (b) FD-PIC results [26]

Figure 6.3 Lunar surface potential versus sun elevation angle
(The IFE-PIC result is for mean flux density solar wind)

We define the electric field from the lunar surface to space has positive direction. The lunar dust normally has negative charge if the lunar potential is negative, and can only be levitated at the negative direction electric field normal to the lunar surface. If the lunar potential is positive, the positively charged dust can only be levitated at the positive electric field. For an exact dust, the levitation is also related to its mass and radius. Wang et al. [26] showed that only the dust with a radius $r_d \leq (3\varepsilon_0\Phi_s E_z/\rho g)^{1/2}$ can satisfy the necessary condition for levitation. However, we should note that this can only happen in the regions with same sign of potential and electric field. Table 6.3 further shows the potential and electric field at the lunar surface. The simulation results are closed to FD-PIC results [26]. The electric field is usually negative when $\alpha < 10^o$, however it switches direction when elevation angle increase near 10^o. The charged dust may not be levitated at sun elevation angle 10^o because of the different sign of lunar surface potential and electric field.

Table 6.3 Potential and electric field at different sun elevation angle for flat surface

	Sun elevation angle	0º	2º	4º	6º	8º	10º
IFE-PIC results	Lunar surface potential (V)	-30.2	-13.5	-9.2	-5.2	-2.8	-2.2
	Electric field (V/m)	-0.82	-0.54	-0.34	-0.19	-0.032	0.085
FD-PIC results	Lunar surface potential (V)	-29.3	-13.2	-7.5	-4.4	-2.8	-2.1
	Electric field (V/m)	-1.15	-0.74	-0.53	-0.27	-0.052	0.054

6.4 Non-flat Lunar Surface Charging

The lunar surface is comprised by many convex and concave regions on the lunar surface. These non-flat regions will affect the local charging environment near the surface. The IFE-PIC method is applied to solve for them around the non-flat lunar surface. The emission of photoelectron on the day-side region under sunlight will cause the positive charge deposited on the lunar surface. Together with the absorbed ambient particles, including electrons, ions, secondary electron and photoelectron, the photoelectrons and secondary electrons emission causes the current collection and charge deposition on lunar surface. The non-homogeneous IFE solver is applied to handle the flux jump condition mentioned in Chapter 2.

In this section, we consider the model of non-flat lunar surface with convex lunar hill. This hill is modeled with a semi sphere convex part on the lunar surface, shown in Figure 6.4.

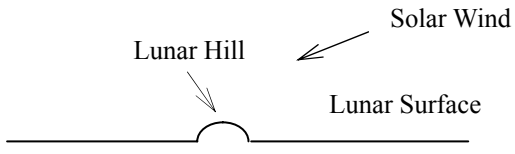

Figure 6.4 Setup of non-flat lunar surface

As the analysis in last section, the lunar dust with negative charge under sun elevation angle 10^o may not be levitated. In this section, we will discuss the effect of non-flat region on lunar surface under this angle. Using the mean solar wind plasma condition, the non-flat lunar surface is simulated with IFE-PIC method. The diameter of the convex semi sphere is 11.86 (16.2m before normalization) and the sun elevation angle is 10^o. The solar wind velocity has two components which are in –z and –x directions.

For convex lunar surface, we are using the simulation domain as 200×2×80. The center of the convex hill with diameter 11.86 (16.2m before normalization) locates at x=98 and z=0, which is x=134.3m and z=0m before normalization. We are using the mesh size h/λ_D=1 and the mesh is shown in Figure 6.5.

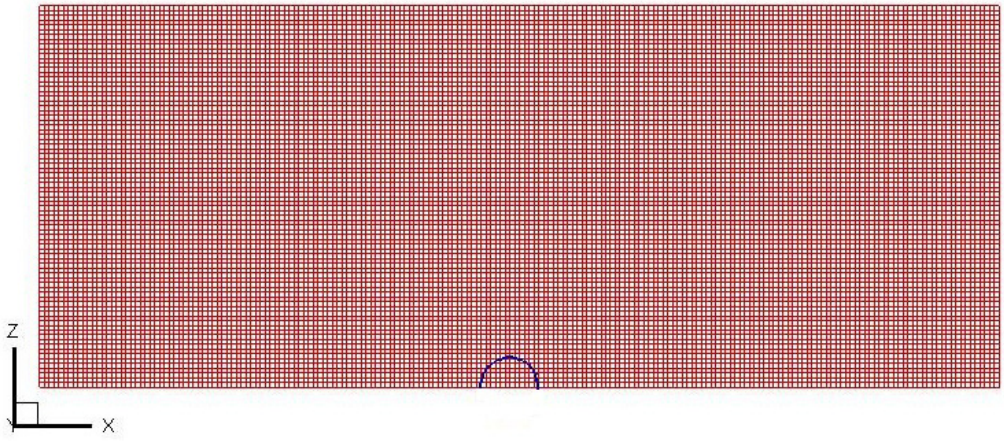

(a) PIC mesh

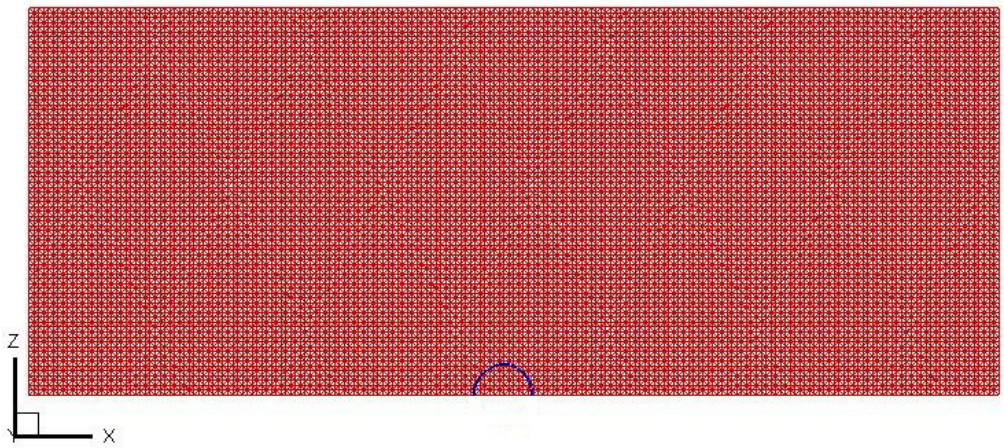

(b) IFE mesh

Figure 6.5 Simulation mesh of the convex lunar surface

The area of the hill facing solar wind emits photoelectron and has positive potential at steady state. The shadow area of the hill becomes a negative potential region. The maximum potential on the hill is about 15V and the minimum potential in the shadow is about -32V. The lunar surface behind the shadow region also has slightly negative

potential which presents the same potential profile as flat surface. Figure 6.6 shows the potential, charge density and electric field normal to the lunar surface. There is a shadow zone with clear edge for ion charge density behind the convex hill because the flowing velocity is much larger than its thermal velocity. However, for electrons with large thermal velocity, the charge density is not zero behind the convex hill. This generates a wake region where the total charge density is positive. The convex hill keeps out the sunlight closely behind the hill, thus photoelectrons can only emitted in the regions out of shadow. The charge density of photoelectrons is largest at the region on the hill facing sunlight. Because the elevation angle is larger on the hill edge which is a curve and this makes a large number density for photoelectron emission. The secondary electrons charge density is quite small compared with photoelectrons and solar wind.

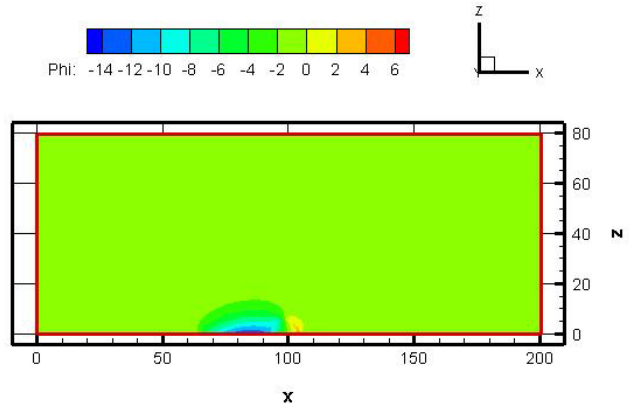

(a)

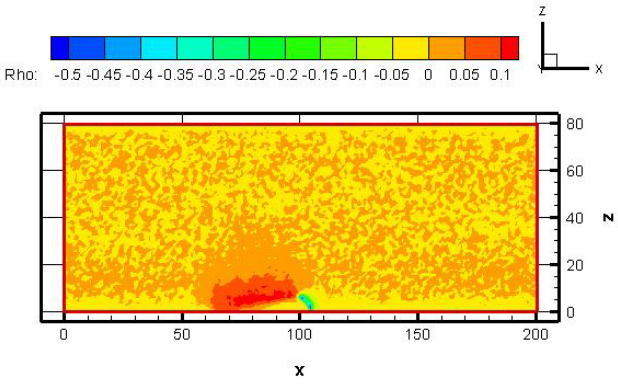

(b)

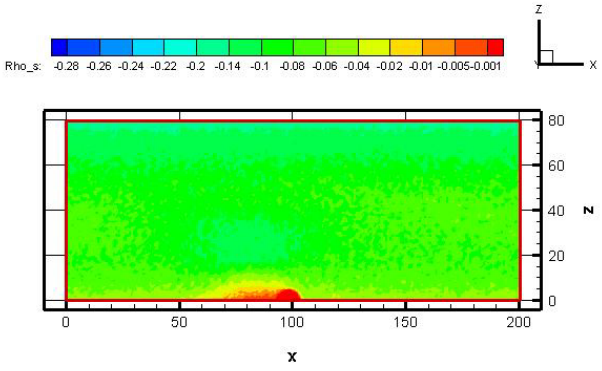
Rho_s: -0.28 -0.26 -0.24 -0.22 -0.2 -0.14 -0.1 -0.08 -0.06 -0.04 -0.02 -0.01 -0.005 -0.001
Z
X
80
60
40
20
0
Z
0
50
100
150
200
X

(c)

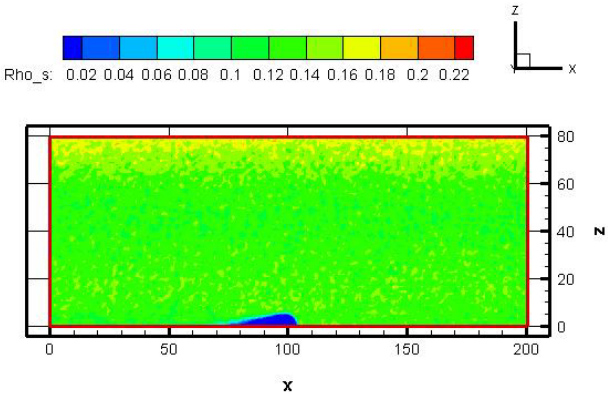
Rho_s: 0.02 0.04 0.06 0.08 0.1 0.12 0.14 0.16 0.18 0.2 0.22
Z
X
80
60
40
20
0
Z
0
50
100
150
200
X

(d)

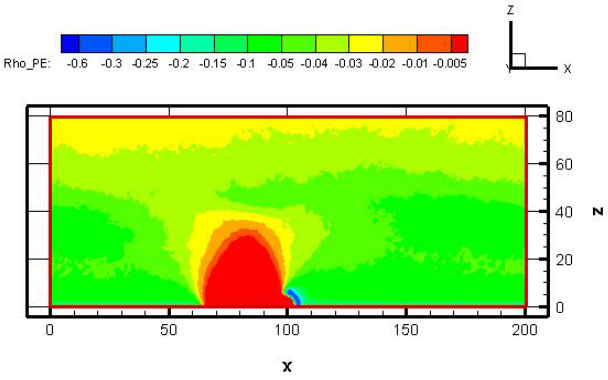
Rho_PE: -0.6 -0.3 -0.25 -0.2 -0.15 -0.1 -0.05 -0.04 -0.03 -0.02 -0.01 -0.005
Z
X
80
60
40
20
0
Z
0
50
100
150
200
X

(e)

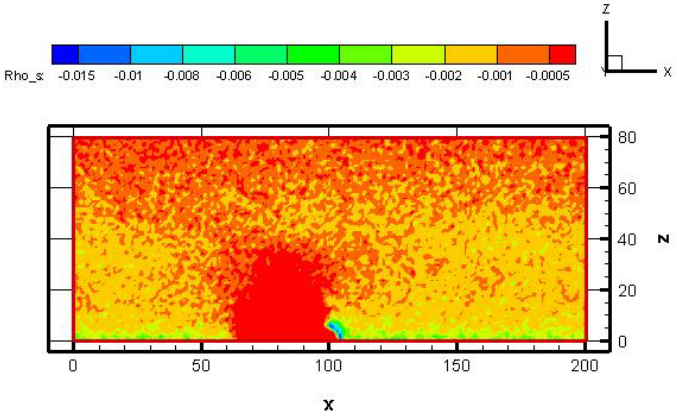
Rho_s: -0.015 -0.01 -0.008 -0.006 -0.005 -0.004 -0.003 -0.002 -0.001 -0.0005
Z
X
80
60
40
20
0
Z
0
50
100
150
200
X

(f)

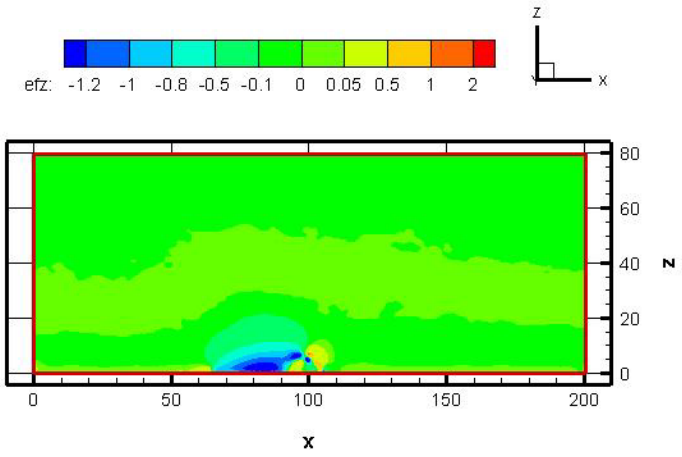

(g)

Figure 6.6 Potential and charge profile of convex lunar surface
(sun elevation angle 10^{o})
(a) potential profile; (b) total charge density profile;
(c) electron density; (d) ion density;
(e) photoelectron density; (f) secondary electron density;
(g) electric field in z direction

Figure 6.7 shows the potential profile on the lunar surface and that versus certain height from the lunar surface. The lunar surface on the hill facing solar wind has positive potential and the shadow region has negative potential. The positive potential of the hill influence the potential profile in front it. For those regions far away behind the shadow or in front of hill with a long distance, the lunar surface potential is negative and the value is closed to the flat surface potential. In the region far away from the hill, the hill's effect to the potential is very small.

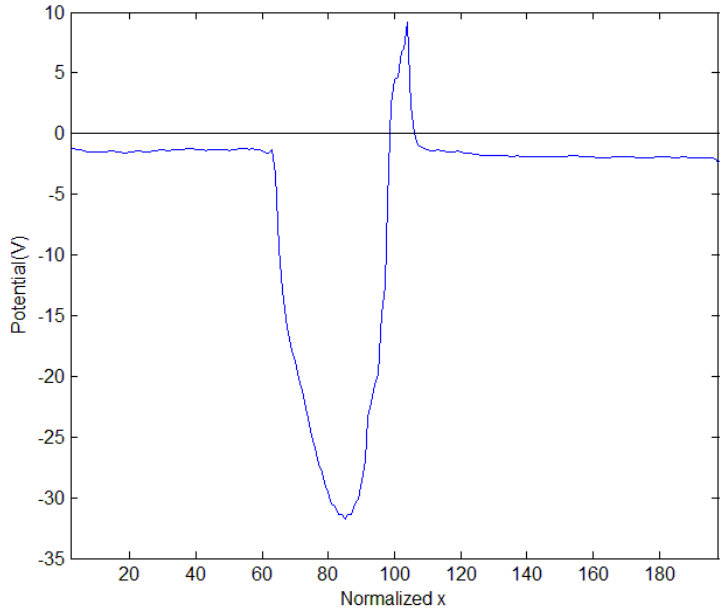

(a)

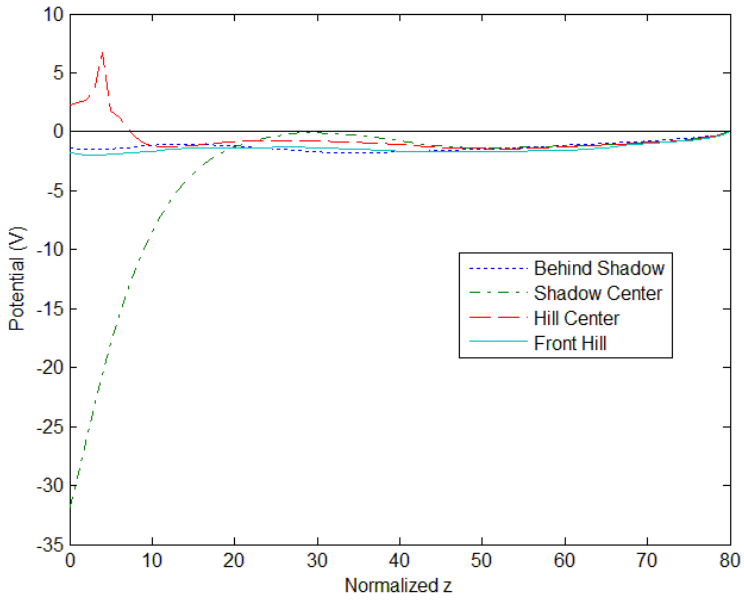

(b)

Figure 6.7 (a) Potential profile on lunar surface;
(b) potential versus distance from the convex lunar surface
(Behind shadow: x=30; shadow center: x=85; hill center: x=102; front hill: x=130)

The electric field component in z direction E_z which is normal to the lunar surface shows a nonmonotonic profile with height increasing. Figure 6.8 (a) shows E_z versus distance from the convex lunar surface at different lunar surface locations. Figure 6.8

(b) shows E_z on the lunar surface. The E_z becomes negative in the shadow area. It is positive at other locations far away from the shadow area and this is the same as that for flat surface. Unlike the flat surface under 10^o sun elevation angle, the charged dust may be levitated in the shadow and hill regions because of the same sign of electric field and lunar surface potential, as that shown in Table 6.4.

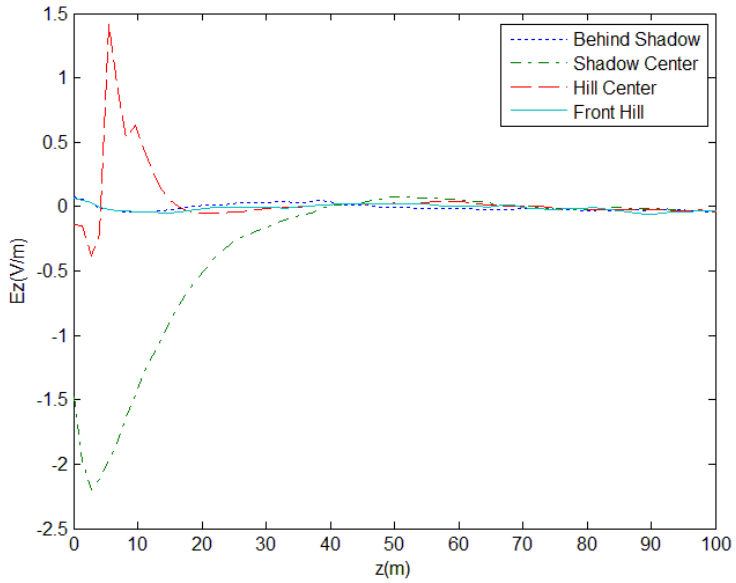

(a)

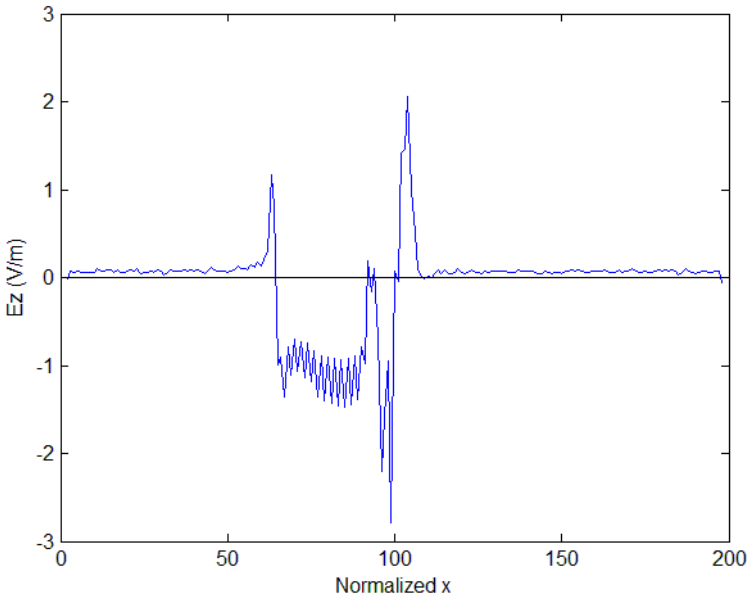

(b)

Figure 6.8 (a) Electric field normal to lunar surface versus distance from the convex lunar surface
(b) Electric field in z direction on lunar surface
(Behind shadow: x=30; shadow center: x=85; hill center: x=102; front hill: x=130)

Table 6.4 Lunar surface potential and electric field on non-flat surface

Locations	Lunar surface potential (V)	Electric field (V/m)
Behind shadow (x=30)	-1.3501	0.0731
Shadow center (x=85)	-31.7764	-1.4776
Hill center (x=102)	6.7380	1.4146
Front hill (x=130)	-1.5319	0.0658

6.5 Charging of Lunar Lander on Lunar Surface

The convex regions on lunar surface affect the potential and electric field profile on lunar surface. Similarly, a lander on lunar surface can also affect the local charging environment. In this section, we include a simplified lander on lunar surface in the simulation. In this simulation, the lunar lander is considered as dielectric material and will also be charged in the plasma environment. It is simplified as a box shape with length×width×height 3×2×6 Debye length which is 4.11m×2.74m×8.22m before normalization. We assume that the lander body is located at 2 dimensionless height (2.74m before normalization) above the convex lunar surface (the lander legs are not modeled). We only consider one sun elevation angle. The sunlight elevation angle is 10º for all cases. The lunar lander facing the sunlight also emits photoelectron. We consider several different distances between the lander and the surface convex region. The distance conditions of these cases are listed in Table 6.5.

Table 6.5 Distance from lunar lander to surface convex region

Cases	Long Distance	Medium Distance	Short Distance
Normalized Distance	98	48	10
Hill Center (x,z)	(198,0)	(148,0)	(110,0)
Hill Diameter	11.86	11.86	11.86
Lunar Lander Position (x coordinate)	97 to 100	97 to 100	97 to 100
Lunar Lander Position (z coordinate)	2 to 8	2 to 8	2 to 8

6.5.1 Lunar Lander at a Distance Far Away from the Hill Region

A lunar lander is put on the downwind direction with long distance from its right edge to the convex semi sphere center. The locations of convex hill and lunar lander are listed in Table 6.5. The simulation mesh size is h/λ_D=1 and the mesh is shown in Figure 6.9.

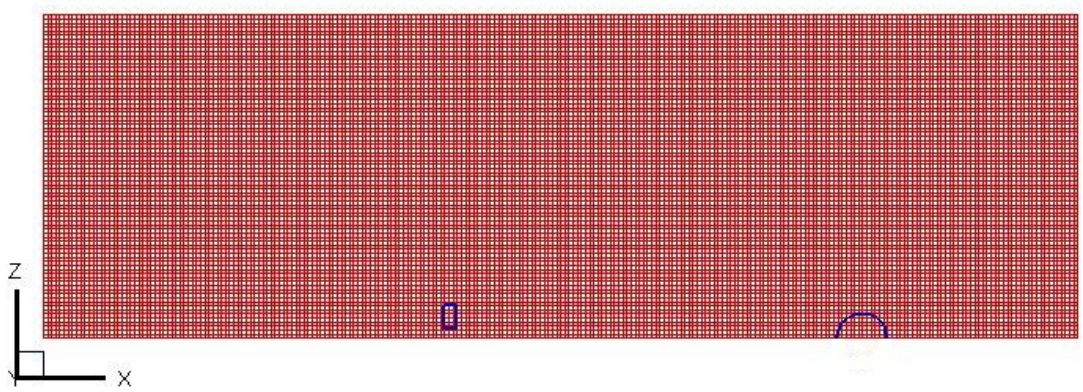

(a) PIC mesh

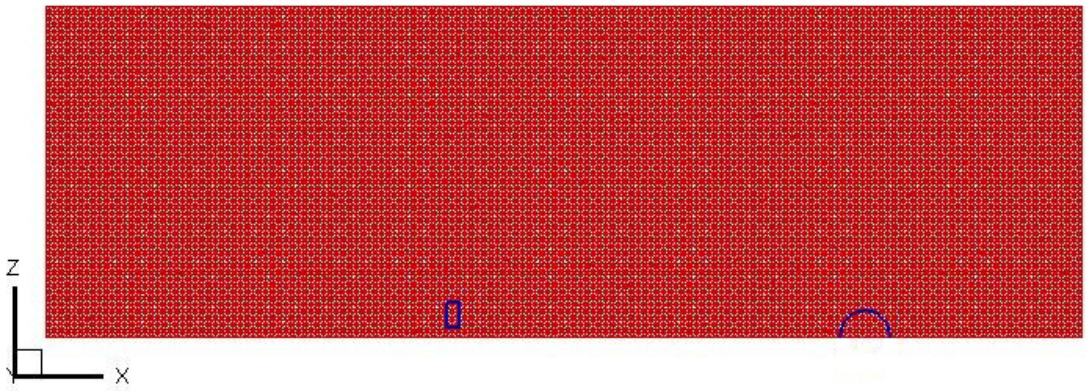

(b) IFE mesh

Figure 6.9 Simulation mesh of the lunar lander
with long distance from lunar convexity

Figure 6.10 shows the potential, total charge density profile and electric field normal to lunar surface for lunar lander on convex lunar surface at steady state with the sun elevation angle 10^o. The convex region facing the solar wind and sunlight has a positive potential with a maximum value about 10V. The lunar lander has positive potential which is about 6V. The shadow area of lunar surface behind the convex hill and lunar lander are negative potential regions and the minimum potential in the shadow is about -26V. The lunar surface behind the shadow region also has slightly

negative potential. However, because of the effect of the positive potential of lunar lander, the area in front of lander has positive potential, the interference of the lunar lander and convex hill is small because of the long distance between them. This is also shown in Figure 6.11 about potential profile on lunar surface (at z=0) along x direction. There are two shadow regions on the lunar surface with negative potential which are separately behind the convex hill and lunar lander. The effect of the hill and lunar lander is small for those regions outside the shadow or far away in front the objects. These regions have negative potential which is the same as flat surface. The potential at some locations of lunar surface are listed in Table 6.6. The sunlight can arrive the region below the lunar lander. Photoelectrons are also emitted in this region, as Figure 6.10 (e) shown.

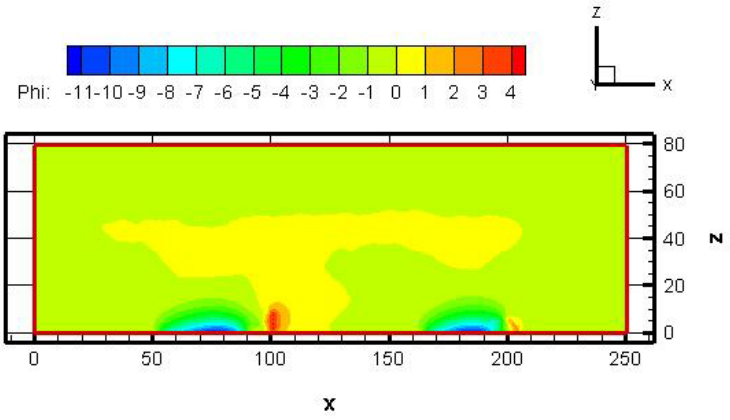

(a)

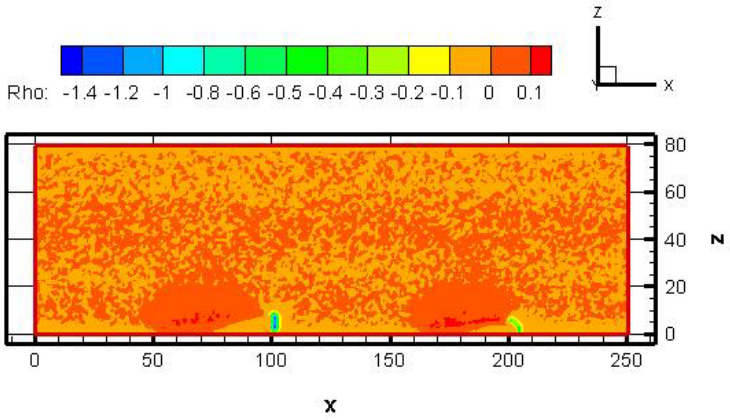

(b)

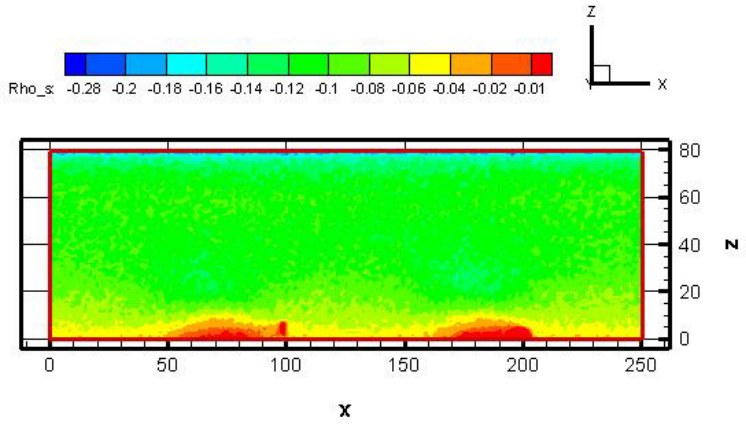
Rho_s: -0.28 -0.2 -0.18 -0.16 -0.14 -0.12 -0.1 -0.08 -0.06 -0.04 -0.02 -0.01
Z
X
80
60
40
20
0
Z
0
50
100
150
200
250
X

(c)

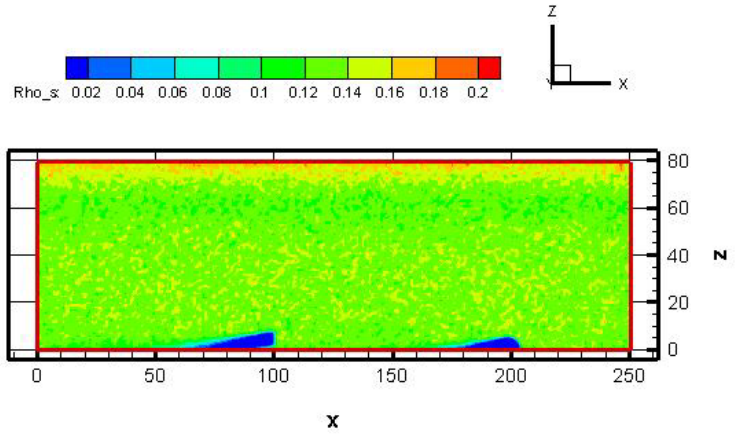
Rho_s: 0.02 0.04 0.06 0.08 0.1 0.12 0.14 0.16 0.18 0.2
Z
X
80
60
40
20
0
Z
0
50
100
150
200
250
X

(d)

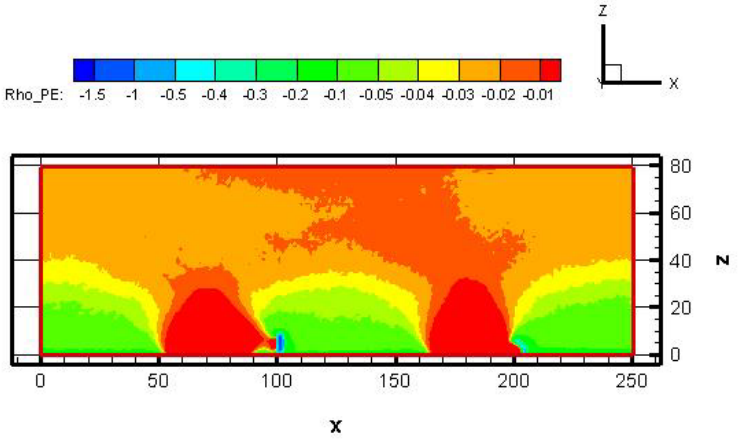
Rho_PE: -1.5 -1 -0.5 -0.4 -0.3 -0.2 -0.1 -0.05 -0.04 -0.03 -0.02 -0.01
Z
X
80
60
40
20
0
Z
0
50
100
150
200
250
X

(e)

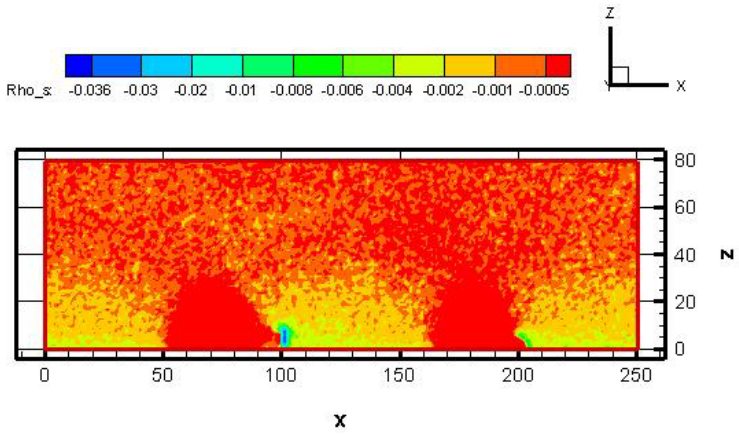

(f)

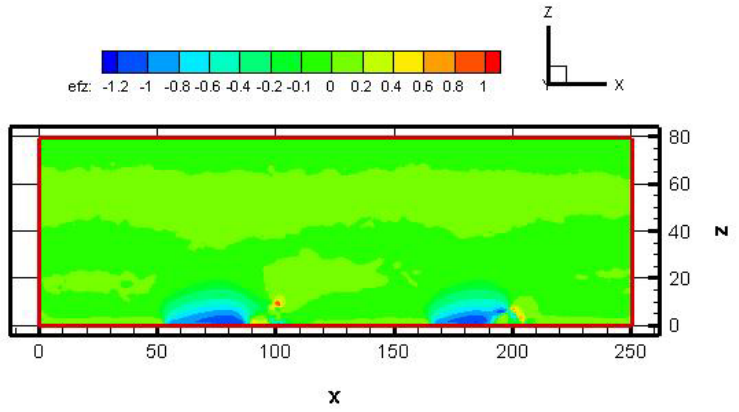

(g)

Figure 6.10 Potential, charge and electric field profile of lunar lander on non-flat lunar surface (distance 100; sun elevation angle 10^{o})
(a) potential profile; (b) total charge density profile; (c) electron density;
(d) ion density; (e) photoelectron density; (f) secondary electron density;
(g) electric field in z direction

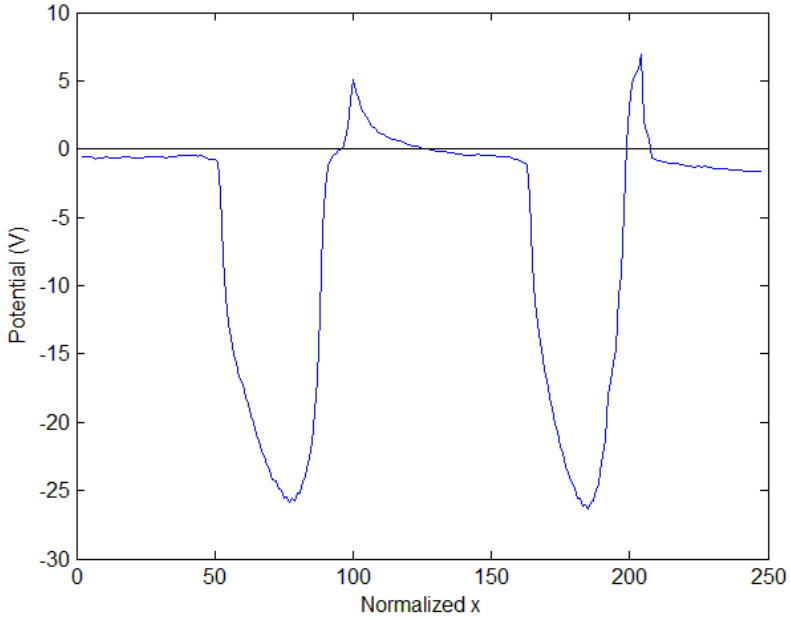

Figure 6.11 Potential profile on lunar surface (at z=0) along x direction
(distance 100; sun elevation angle 10^o ;
shadow center of lunar lander :x=80; behind the lunar lander: x=95;
center of lunar lander: x=99; in front of the lunar lander: x=110;
the shadow center of the convex hill: x=175; behind the convex hill: x=190;
center of convex hill: x=198; in front of the convex hill: x=220)

Table 6.6 Lunar surface potential and electric field on convex surface with lunar lander (distance 100)

Locations	Behind lander shadow	Lander shadow center	Behind lunar lander	Under lunar lander	Behind convex hill shadow	Convex hill shadow center	Front convex hill
Normalized Location x	50	77	95	99	150	180	220
Real location x (m)	68.5	105.5	130.2	135.6	205.5	246.6	301.4
Lunar surface potential (V)	-0.80	-25.84	-0.05	3.53	-0.50	-24.80	-1.21
Electric field in +z direction (V/m)	0.35	-1.20	0.57	0.27	0.08	-0.79	0.05

Figure 6.12 shows E_z on lunar surface (at z=0) along x direction. There are four regions with positive E_z: the two regions behind the shadows, the region under the lunar lander and the region in front of the convex hill. These regions have the same electric field direction compared with the flat lunar surface case. The maximum of the positive electric field value is about 1.52V/m. For other area in the shadow, E_z is

negative and the minimum of the negative value is about -1.4V/m. This information will be useful in future studies of dust levitation.

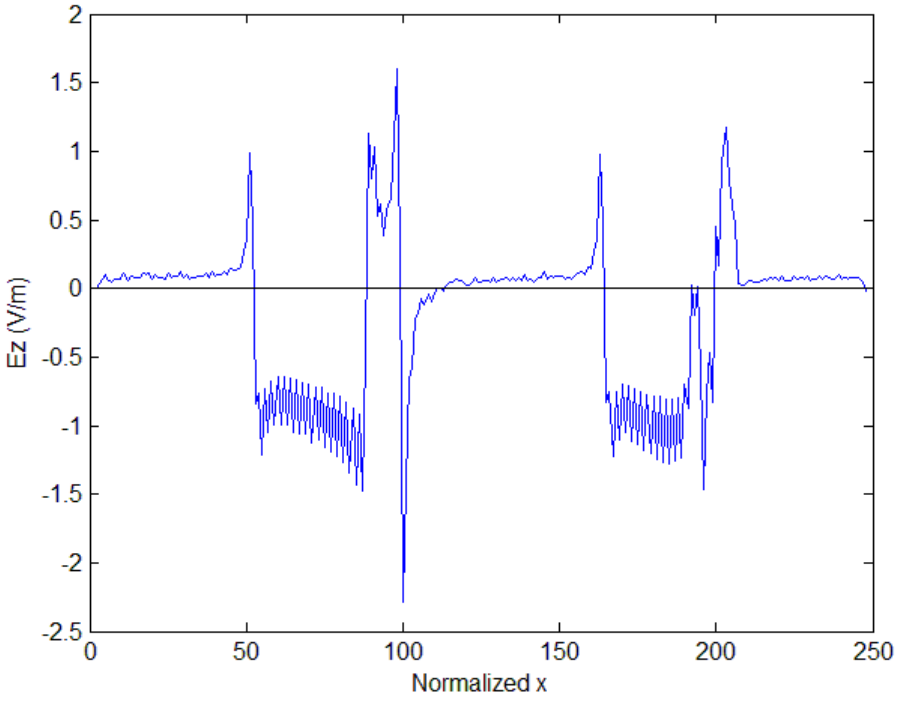

Figure 6.12 Electric field in +z direction on lunar surface (at z=0) along x direction (distance 100; sun elevation angle 10^{o} ;
shadow center of lunar lander :x=80; behind the lunar lander: x=95;
center of lunar lander: x=99; in front of the lunar lander: x=110;
the shadow center of the convex hill: x=175; behind the convex hill: x=190;
center of convex hill: x=198; in front of the convex hill: x=220.
The small oscillations in the Ez profile are due to numerical noise.)

6.5.2 Lunar Lander at a Closer Distance to the Hill Region

Considering different distance between lunar lander and the convex hill on lunar surface, we are investigating the effect of the distance such as 48 and 10 from the right edge of lunar lander to the convex hill center. We call them “medium distance case” and “short distance case” while last case is called “long distance case”. The locations of box lunar lander and the convex hill are listed in Table 6.5 for both medium and short distances case. The simulation mesh size is the same as the long distance case and the mesh is also similar.

The potential and E_z profiles for medium and short distance cases are shown in Figure

6.13. For medium distance case, the distance between the lunar lander and convex hill doesn't affect the potential profile too much compared with long distance case. There are still two shadow regions in potential profile. The maximum potential of the lunar surface convex hill and lunar lander are separately 5.1V and 12.3V. The minimum potential of the shadow is -29.1V.

However, for the short distance case, the shadows of lunar lander and convex hill overlap with each other. The maximum potential of the lunar surface convex hill and lunar lander are separately 6.3V and 12.8V. The minimum potential of the shadow is -32V.

Compared with the long distance case, in which the maximum potential of lunar surface hill and lunar lander is 6V, 10V and the minimum potential in shadow is -26V, the level of the potential is nearly the same for different distance, but the absolute value of the potential is larger for small distance. The electric field E_z is still nonmonotonic with the height increase for all these cases.

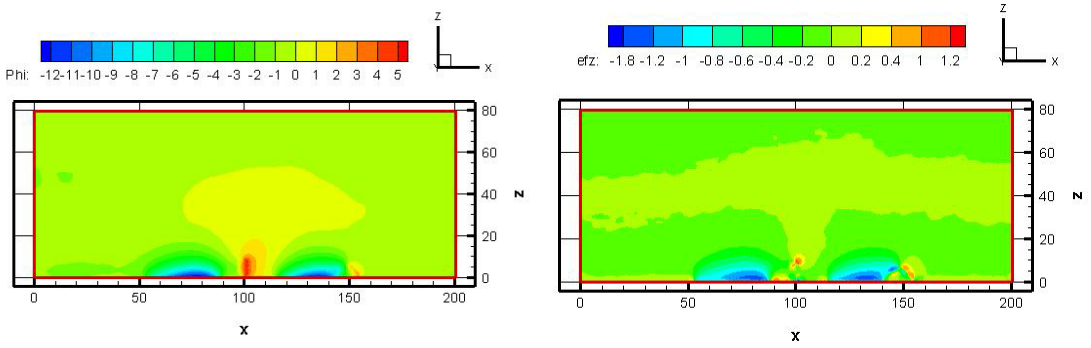

Potential Electric field in +z direction

(a)

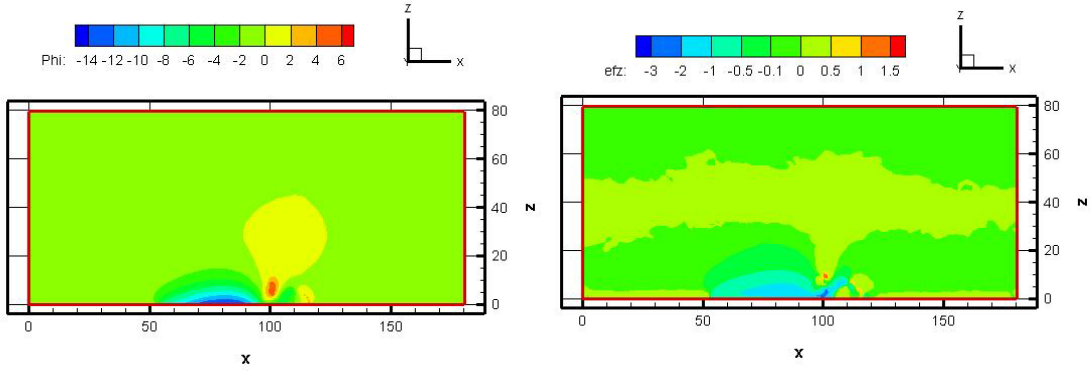

Potential Electric field in +z direction

(b)

Figure 6.13 Potential and electric field profile of lunar lander on convex lunar surface
(a) medium distance 48; sun elevation angle 10^o ;
(b) short distance 10; sun elevation angle 10^o

Figure 6.14 and Figure 6.15 shows the potential and E_z on lunar surface along x direction for medium distance case. They are nearly the same as the long distance case. The potential and E_z on lunar surface along x direction for short distance case are shown in Figure 6.16 and Figure 6.17. Compared with the long distance and medium distance cases, there is no positive region between the lander and convex hill for short distance case because the lunar surface under the lander is in the shadow area of the convex hill. The electric field in z direction is also negative on the lunar surface under the lander. This is different with the other two cases which has positive electric field under lunar lander.

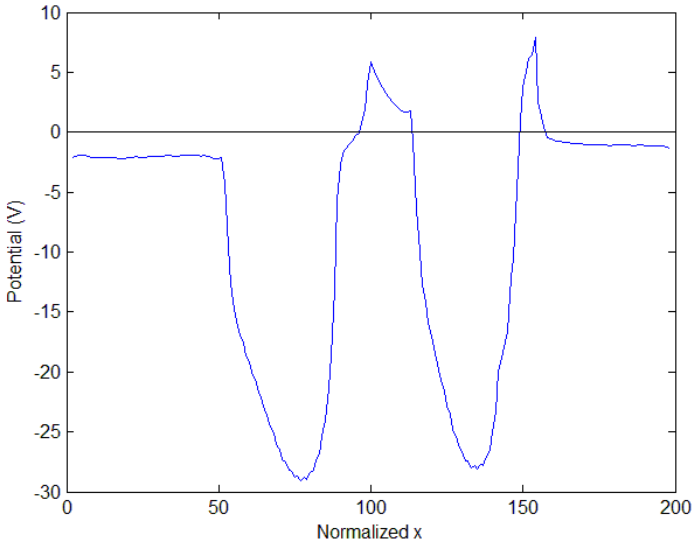

Figure 6.14 Potential on lunar surface along x direction
(Distance 48; sun elevation angle 10^{o})

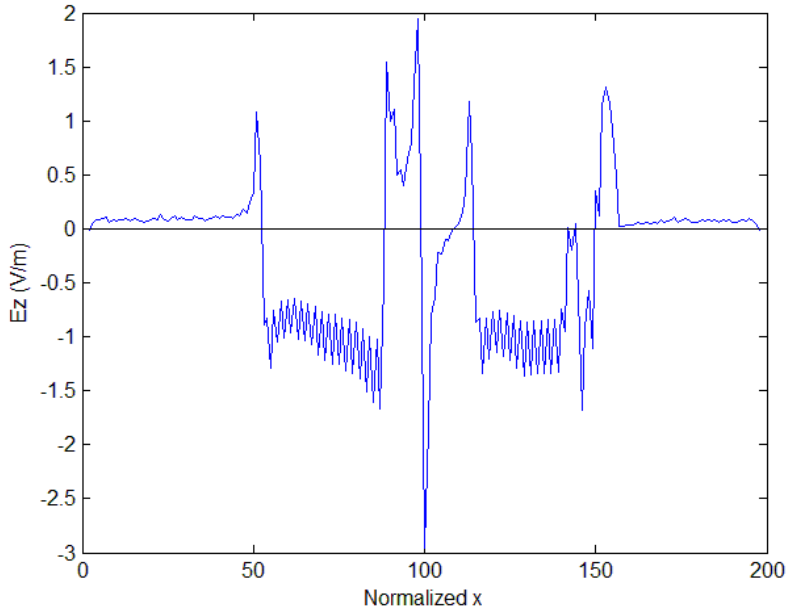

Figure 6.15 Electric field in +z direction on lunar surface along x direction (Distance 48; sun elevation angle 10^{o}.
The small oscillations in the Ez profile are due to numerical noise.)

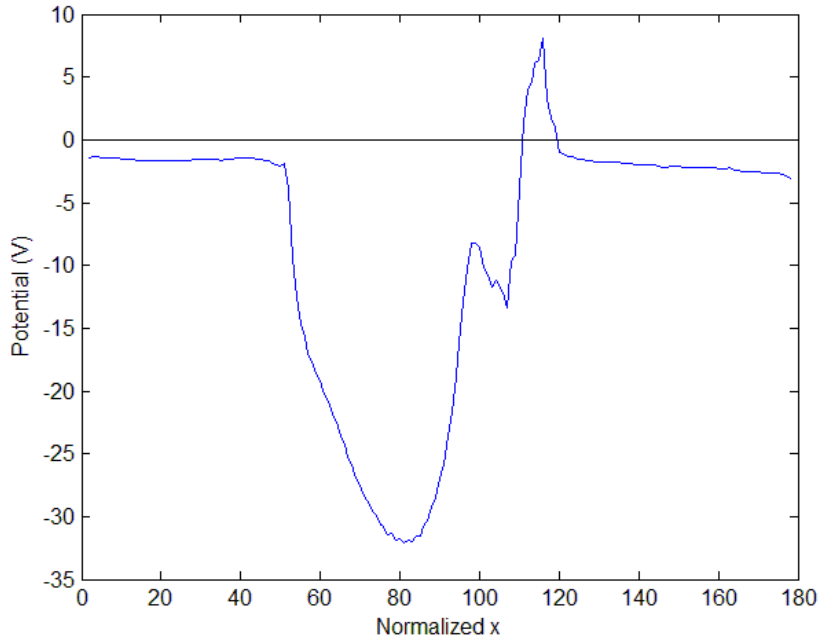

Figure 6.16 Potential on lunar surface (at z=0) along x direction (Distance 10; sun elevation angle 10^{o})

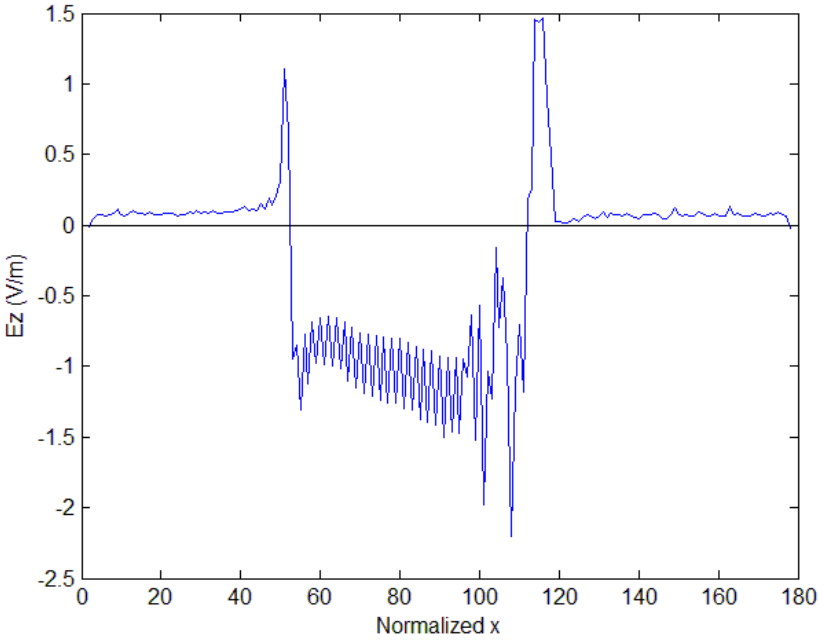

Figure 6.17 Electric field in +z direction on lunar surface (at z=0) along x direction (Distance 10; sun elevation angle 10^{o} .
The small oscillations in the Ez profile are due to numerical noise.)

The potential and electriec field at some lunar surface locations for medium and short distance case are separately listed in Table 6.7 and 6.8. For the medium distance case, the charged dust may be levitated in the two shadow region, as well as the regions under the lunar lander and in front of the lander.

Table 6.7 Lunar surface potential and electric field on convex surface with lunar lander (distance 48)

Locations	Behind lander shadow	Lander shadow center	Behind lunar lander	Under lunar lander	Behind convex hill shadow	Convex hill shadow center	Front convex hill
Normalized Location x	50	77	95	99	110	127	170
Real location x (m)	68.5	105.5	130.2	135.6	150.7	174.0	232.9
Lunar surface potential (V)	-2.22	-29.10	-0.29	4.00	1.79	-24.77	-1.01
Electric field in +z direction (V/m)	0.34	-1.31	0.65	0.28	0.04	-1.29	0.56

Table 6.8 Lunar surface potential and electric field on convex surface with lunar lander (distance 10)

Locations	Behind lander shadow	Lander shadow center	Behind lunar lander	Under lunar lander	Behind convex hill shadow	Front convex hill
Normalized Location x	50	77	95	99	102	130
Real location x (m)	68.5	105.5	130.2	135.6	139.7	178.1
Lunar surface potential (V)	-2.07	-31.39	-16.24	-8.23	-10.72	-1.74
Electric field in +z direction (V/m)	0.31	-1.26	-1.47	-1.52	-1.03	0.07

6.6 Conclusion

In this chapter, the non-homogeneous IFE-PIC model is applied to simulate the lunar surface charging problem. We considered the flat lunar surface charging and non-flat lunar surface charging separately. For flat lunar surface charging, the potential, charge density and electrostatic field profiles at steady state are given for different solar wind elevation angles. The non-flat lunar surface is considered. The effect of the spacecraft on the lunar surface charging is then discussed. These results will be useful for further study on dust levitation on lunar surface.

Chapter 7

Conclusions

7.1 Summary

This dissertation studies the object-plasma interaction problem using Particle-In-Cell method involving complex boundary condition. This dissertation develops the IFE solver from previous work to include non-zero flux jump condition for charging calculation. Numerical experiments were performed and the error using this solver has second order convergence in L^2 norm and first order convergence in H^1 norm as expected. Together with the Particle-In-Cell (PIC) model, this new non-homogeneous IFE-PIC solver can solve the potential and electrostatic field in the simulation system including the object and space. This provides a simulation tool to investigate the charging process of the object and its floating potential.

Then this IFE-PIC solver is applied in three applications. First, the charging of spherical objects in plasma is simulated. The single conductive spherical object with different fixed potential is examined in stationary plasma and flowing plasma. The current density vs. potential curve matches well with the analytical solution using OML theory. The non-homogeneous IFE solver is applied to solve the floating potential of a single dielectric spherical object in stationary and flowing plasma. The charge absorbed by the object is deposited on the object surface and the object potential changes with deposited charge amount. The deposited charge provides the non-zero flux jump condition for non-homogeneous IFE solver. The charging process of multiple spheres is also studied by simulating four and five sphere-cluster in stationary plasma. The capacitance of each sphere in the multi-sphere cluster shows a smaller value compared with that for single dust.

The second application is a study on the secondary electron emission process in

vacuum chamber to assist the secondary electron yield measurement in the experiments. This simulation work provides an adjustment and design method for the experimental results and assists to reduce the error and obtain the secondary electron yield curve. The Lambert's cosine law emission distribution of particles from a small plane is verified and the results match well with the experimental results. The effect of primary electron current density is studied. For high current density primary electron beams, the secondary electron emission area is a point source on the target plate. The cosine law can be observed in experiment and simulation results. If the plate potential is large and affects the trajectory of emitted secondary electrons, the cosine law is not observed at a certain distance from the source although the emission of secondary electrons still obeys the cosine law.

The third application studies charging on lunar surface. The code is first applied to simulate charging on a flat lunar surface with sun elevation angle from 0º to 10º, the potential is negative and increase to zero at infinity far away from the surface. The surface with smaller α has larger potential absolute value. The electrostatic field normal to lunar surface E_z directs to the lunar surface at small α, however, at α near 10º case, E_z reverse direction although potential is still negative. The code is then applied to study charging on a non-flat lunar surface. For convex lunar surface where a lunar hill is simulated, the potential of the hill facing the solar wind is positive for the α=10º case. However, the potential becomes negative at the area behind the convex hill. If a lunar lander is located near the convex hill, the potential and electric field profiles are changed. As the lunar dust levitation condition sensitively depends on the surface charging potential and the local plasma environment, these results will be useful for future studies of lunar dust levitation.

7.2 Future Work

7.2.1 Immersed Finite Element Particle-In-Cell

We have developed the Immersed Finite Element method for solving non-homogeneous boundary value problem with non-zero flux jump condition on interface. This method can solve the three-dimensional second order elliptic problem well with small difference between the discontinuous property coefficients. If the $\varepsilon^-/\varepsilon^+$ ratio in equation (2.1) is small, the regression of solution error has approximately second order convergence for L^2 error and first order convergence for H^1 error. However, for large $\varepsilon^-/\varepsilon^+$ ratio, the solution doesn't have the expected convergence

order. A future work is going on investigating the IFE method with non-zero flux jump condition for large discontinuous coefficients ratio.

The code is applied to study surface charging in rarefied plasma. In the current code, the charges of the absorbed particles are deposited locally on the object surface to provide the non-zero interface jump condition for the IFE field solver. The approach only applies to a dielectric surface. For a conducting surface, the collected charges need to be redistributed to generate an equal potential surface. Hence, the current code cannot be applied to study a conducting surface. Additionally, the handling of the charge deposition of particle just outside the object in an interface cell is not exactly correct. The current code still applies the standard finite-difference based charge deposition for interface cell. This needs to be corrected in future work.

7.2.2 Dust Charging Problem

This dissertation takes the initial step in studying dust charging in dusty plasmas. Instead of dusty plasma, we considered small spheres with a radius smaller than the Debye length and a 4 or 5 sphere cluster. While the single sphere charging shows good agreement with the OML theory, the results show that the charging accumulated by a sphere in the cluster is smaller than that in the single sphere case. This indicates that the commonly used OML model in dust charging may not be accurate for application in dusty plasma. The studies presented here is only the initial step. Further study will be needed to further address this problem.

7.2.3 Secondary Electron Emission Experiment

In this dissertation, we considered the facility effect in secondary electron emission experiments. The work in this dissertation only considered the effects of complex geometry shape and the target plate is conducting plate with fixed potential. The charging of this target plate is not included. In future work, a new experiment which includes the charging of the target plate will be studied.

7.2.4 Lunar Surface Charging Problem

In this simulation of lunar surface charging problem, the lunar surface is modeled either as a flat surface or a non-flat surface modeled by semi-circle. The lunar lander considered is a simplified box structure. Further mode, the lunar dust charging problem has not been considered. Future study will extend this study to more realistic surface landscape and to actually address the charging of dusts sitting on surface.

Bibliography

[1] R. W. Hockney and J. W. Eastwood. Computer Simulation Using Particles. The Institute of Physics, 1999

[2] D. Hastings, H. Garrett, Spacecraft-Environment Interactions, Cambridge University Press, 1996

[3] R. N. DeWitt, D. Duston, A. K. Hyder, The Behaviour of Systems in the Space Environment, Kluwer Academic Publishers, 1993

[4] E. C. Whipple, Potential of Surfaces in Space, Reports on Progress in Phyiscs, Vol. 44, 1197-1250, 1981

[5] G. A. Bird, Molecular Gas Dynamics, Clarendon Press, Oxford, England, 1976

[6] Raed I. Kafafy, PhD Dissertation, Virginia Polytechnic Institute and State University, 2005

[7] J. Wang, X, He, Y. Cao, Modeling electrostatic levitation of dust particles on lunar surface, IEEE transactions on plasma science, Vol. 36, No.5, 2459-2466, Oct. 2008

[8] J.E. Daugherty, R. K. Porteous, M. D. Kilgore, D. B. Graves, Sheath structure around particles in low-pressure discharges, Journal of Applied Physics, Vol. 72, Issue 9, pp 3924-3942, 1992

[9] O. Ishihara, S. V. Vladimirov, Wake potential of a dust grain in a plasma with ion flow, Physics of Plasmas, Vol. 4, Issue 1, 69, 1997

[10] T. Nitter, O. Havnes, and F. Melandso, Levitation and Dynamics of Charged Dust in the Photoelectron Sheath Above Surfaces in Space, J. Geophysical Research, 103(A4), 6605-6620, 1998

[11] E. Choiniere, PhD thesis, University of Michigan, 2004

[12] J. C. McMahon, G. Z. Xu, J. G. Laframboise, The effect of ion drift on the sheath, presheath, and ion-current collection for cylinders in a collisionless plasma, Physics of Plasma, Vol. 12, 2005

[13] J. Wang and D.E. Hastings, Ionospheric plasma flow over large high voltage space platforms I: Ion-plasma time Scale interactions on a plate at zero angle of attack, Phys. Fluids B, 4(6), 1597-1614, 1992a.

[14] J. Wang and D.E. Hastings, Ionospheric plasma flow over large high voltage space platforms II: the formation and structure of the plasma wake, Phys. Fluids B, 4(6), 1615- 1629, 1992b.

[15] H. Garrett and J. Wang, Simulations of solar wind plasma flow round a simple solar sail, Spacecraft Charging Technology Conference, Huntsville, AL, Oct. 2003.

[16] J. E. Allen, R. L. F. Boyd, P. Reynolds, The collection of positive ions by a probe immersed in a plasma, Proceedings of the Physics Society, Vol. 70, No.3, pp 297, 1957

[17] R.V. Kennedy, J. E. Allen, The floating potential of spherical probes and dust grains. Part 1. Radial motion theory, Journal of Plasma Phyiscs, Vol. 67, Part 4, pp. 243-250, 2002

[18] J. E. Allen, B. M. Annaratone , On the orbital motion limited theory for a small body at floating potential in a Maxwellian plasma, Journal of Plasma Physics, Vol. 63, 299-309, 2000

[19] R. V. Kennedy, J. E. Allen, The floating potential of spherical probes and dust grains. II: Orbital motion theory, Journal of Plasma Physics, Vol. 69, part 6, pp. 485-506, 2003

[20] J. W. Eastwood, Computational plasma physics, Plasma Physics: an introductory course, Edited by R. O. Dendy, Cambridge University Press, 1993, pp167-187

[21] J. H. Bramble, J. T. King. A finite element method for interface problems in domain with smooth boundaryies and interfaces, Advances in Computational Mathematics, 6: 109-138, 1996

[22] J. W. Eastwood, W. Arter, N. J. Brealey, R. W. Hockney, Body-fitted electromagnetic PIC software for use on parallel computers, Computer Physics

Communications, 87: 155-178, 1995

[23] Z. Li, T. Lin, X. Wu, New Cartesian grid methods for interface problems using the finite element formulation, Numerische Mathematik, 96 (1): 61-98, 2003

[24] S. Deng, K. Ito, Z. Li, Three-dimensional elliptic solvers for interface problems and applications, Journal of Computational Physics, 184: 215-243, 2003

[25] T. Lin, Y. Lin, R. Rogers, M. L. Ryan, Advances in Computation: Theory and Practice, A rectangular immersed finite element space for interface problems, pp 107-114, Nova Science Publishers, Inc., Commack, NY, 2001

[26] R. Kafafy, T. Lin, Y. Lin, J. Wang, Three dimensional immersed finite element methods for electric field simulation in composite materials, International Journal for Numerical Methods in Engineering, 64: 940-972, 2005

[27] J. Halekas, D. Mitchell, R. Lin, L. Hood, M. Acuna, and A. Binder, Evidence of for Negative Charging of the Lunar Surface in Shadow, Geophysical Research Letters, 29(10), 2002.

[28] M.Horanyi, B. Walch, S. Robertson, and D. Alexander, Electrostatic Charging Properties of Apollo 17 Lunar Dust, Journal of Geophysical Research, 103(E4), 8575-8580, 1998

[29] G. Lapenta, Simulation of charging and shielding of dust particles in drifting plasmas, Physics of Plasmas, Vol. 6, No.5, pp 1442-1447, 1999

[30] A. Sickafoose, J. Colwell, M. Horanyi, and S. Robertson, Experimental Levitation of Dust Grains in a Plasma Sheath, Journal of Geophysical Research, 107(A11) 1408, 2002

[31] M. J. Mandell et al., Nascap2k - spacecraft charging analysis code for the 21st century, In 39th Aerospace Sciences Meeting and Exhibit, AIAA 01.957, Reno, Nevada, January 2001.

[32] M. J. Mandell, I. Katz, J. M. Hilton, D. L. Cooke, and J. Minor, Nascap- 2K spacecraft charging models: Algorithms and applications, in Proc. 7th Spacecraft Charging Technol. Conf., pp. 23-27, 2001.

[33] M. J. Mandell et al. Modeling the charging of geosynchronous and interplanetary space-craft using nascap-2k. Advances in Space Research, 36, 2005.

[34] M. J. Mandell , G. A. Jongeward, and D. L. Cooke, Spacecraft-plasma interaction codes: NASCAP/GEO, NASCAP/LEO, POLAR, DynaPAC, and EPSAT, Fifth Annual Workshop on Space Operations Applications and Research, Houston, Texas, July 9-11, pp 672-679, 1991.

[35] M. J. Mandell, and I. Katz, High voltage plasma interactions calculations using NASCAP/LEO, AIAA Paper AIAA-90-0725, 1990.

[36] M. J. Mandell, D. L. Cook, V. A. Davis, G Jongeward, B. M. Gardner, R. A. Hilmer, K.P. Ray, S. T. Lai, L. H. Krause, Modeling the charging of geosychronous and inter-planetary spacecraft using Nascap-2k, Advnaces in space research, 36, 2511-2515, 2005.

[37] J. Forest, L. Eliasson, and A. Hilgers, A New spacecraft plasma simulation software, PicUp3D/Spis, 7th Spacecraft Charging and Technology Conference, p.515.520, ESA/SP-476, ESAESTEC, Noordwijk, The Netherlands, 23.27 April 2001.

[38] A. Hilgers, J. Forest, and J. F. Roussel. (2002, Dec). SPIS, the spacecraft plasma interaction system. [Online]. Available:http://dev.spis.org/projects/spine/home/spis.

[39] A. Hilgers, B. Thiebault, J.-F. Roussel, J. Forest, and E. Engwall, Tests and validation of a new spacecraft plasma interaction software, SPIS, in Proc. 9th Spacecraft Charging Technol. Conf., Tsukuba, Japan, 2005.

[40] J.F. Roussel, F. Rogier, D. Volpert, G. Rousseau, J. Forest, and A. Hilgers, Spacecraft plasma interaction software (SPIS): Numerical solvers.Methods and architecture, in Proc. 9th Spacecraft Charging Technol. Conf., 2005, Tsukuba, Japan.

[41] P. Lee, Dust Levitation on Asteroids, Icarus, 124, 181-194, 1996

[42] O. Berg, A lunar terminator configuration, Earth and planetary science letters, 39, 377-381, 1978.

[43] S. Hosoda, T. Muranaka, H. Ueda, K. Koga, T. Goka, H. Kuninaka, S. Hatta, J. Kim, N. Kurahara, M. Cho, Laboratory experiments for code validation of multi-utility spacecraft charging analysis tool (MUSCAT), Proc. 10th Spacecraft Charging Technology Conference, Biarritz, France, June 2007.

[44] T. Muranaka, S. Hosoda, S. Hatta, J. Kim, K. Ikeda, M. Cho, H. Ueda, K. Koga, T. Goka, Final version of Multi-Utility Spacecraft Charging Analysis Tool (MUSCAT), Proc. 10th Spacecraft Charging Technology Conference, Biarritz, France, June 2007.

[45] P. K. Shukla, A. A. Mamun, Introduction to Dusty Plasma Physics, 2002

[46] C. R. Buhler, C. I. Calle, J.S. Clements, J.G. Mantovani, M.L. Ritz, Test Method for In Situ Electrostatic Characterization of Lunar Dust, IEEE Aerospace Conference, pp 1-19, 2007

[47] Y. Lin, D. C. Joy, A New Examination of Secondary Electron Yield Data, Surface and Interface Analysis, 2005;37: 895-900

[48] J.M. Lafferty. Foundations of vacuum science and technology. New York: Wiley, 1998.

[49] J. Greenwood, The Correct and Incorrect Generation of a Cosine Distribution of Scattered Particles for Monte-Carlo Modelling of Vacuum Systems, Vaccum, 67, 2002, 217-222

[50] J. D. Jackson, Classical electrodynamics, 3rd edition, New York: Wiley, 1999

[51] Xiaoming He, PhD Dissertation, Virginia Polytechnic Institute and State University, 2009

[52] C. J. Roy, Review of code and solution verification procedures for computational simulation, Journal of Computational Physics, 205 (2005), 131-156

[53] J.McCoy and D. Criswell, 'Evidence for a high altitude distribution of lunar dust', in Proc. 5th Lunar Sci. Conf., Geochim. Cosmochim. Acta, 1974, vol.3, pp2991-3005. Suppl.5.

[54] R.F. Willis, M. Anderegg, B. Feuerbacher, B. Fitton, Photoemission and Secondary Electron Emission from Lunar Surface Material. In: R. Gard, Photon and Particle Interaction with Surfaces in Space. Reidel, Dordrecht, pp. 369-387.

[55] R.J.L. Grard, J.K.E. Tunaley, Photoelectron Sheath Near a Planetary Probe in Interplanetary Space. J. Geophysical Research. 76, 2498-2505, 1971

[56] M. Cho, D. E. Hastings, Dielectric charging processes and arcing rates of high voltage solar arrays, Journal of Spacecraft and Rockets, Vol. 28, p.698, 1991.

[57] M. Cho, Arcing on high voltage solar arrays in low earth orbit: theory and computer simulation, PhD dissertation, 1992.

[58] S. J. Beard, A program for the direct solution of Poisson's equation in complex geometries, Computer physics communications, 36, 25-57, 1985.

[59] R. W. Hockney, POT4- a FACR algorithm arbitrary regions, computers fast ellipse solvers and application, Advance publications Ltd, London, pp. 141-169, 1978.

[60] Hyunju Jeong, PhD Dissertation, Virginia Polytechnic Institute and State University, 2008

[61] J.Gaier, 'The effects of lunar dust on EVA systems during the Apollo missions', NASA, John H. Glenn Res. Center, Cleveland, OH, NASA TM-2005-213610, 2005

[62] J. E. Colwell, A. A.S. Gulbis, M. Horanyi, S. Robertson, Dust transport in photoelectron layers and the formation of dust ponds on Eros, Icarus, Vol. 175, No. 1, pp 159-169, 2005

[63] T. J. Stubbs, R. R. Vondrak, W. M. Farrell, A dynamic fountain model for lunar dust, Advances in Space Research, Vol. 37, No. 1, 59-66, 2006

[64] W. M. Farrell, T. J. Stubbs, R. R. Vondrak, G. T. Delory, J. S. Halekas, Complex electric fields near the lunar terminator: the near-surface wake and accelerated dust, Geophysical research letter, Vol. 34, no. 14 , 2007

[65] R. Manka, Plasma and Potential at the Lunar Surface, in Photon and Particle Interactions with Surfaces in Space, R. Grard, Ed. Dordrecht, The Netherlands: Reidel, 1973, pp. 347-361

[66] R. L. Guernsey, J. H. M. Fu, Potential Distribution surrounding a photo-emitting plate in a dilute plasma, J. Geophysical Research, 75, 3193-3199, 1970

[67] B. Feuerbacher, M. Anderegg, B. Fitton, L. D. Laude, R. F. Willis, R. J. L. Grard, Photoemission from Lunar Surface Fines and the Lunar Photoelectron Sheath, Proc. Lunar Sci. Conf., IIIrd, 2655-2663, 1972

[68] R. J. L. Grard, Properties of the satellite Photoelectron Sheath Derived from Photoemission Laboratory Measurements, J. Geophys. Res., 78, 2885-2906, 1973

[69] T. E. Sheridan, J. Goree, Y. T. Chiu, R. L. Rairden, J. A. Kiessling, Observation of Dust Shedding from Material Bodies in a Plasma, J. Geohphys. Res., 97, 2935-2942, 1992

[70] T. Nitter, T. K. Aslaksen, F. Melandso, O. Havnes, Levitation and Dynamics of a Collection of Dust Particles in a Fully Ionized Plasma Sheath, IEEE Trans. Plasma Sci., 22, 159-172, 1994

[71] Jianming Jin, The Finite Element Method in Electromagnetics, 2nd Edition

[72] J. Rennilson and D. Criswell, 'Surveyor observations of lunar horizon glow', Moon, vol.10, no.2, pp.121-142, Jon. 1973

[73] C. K. Birdsall, A. B. Langdon, Plasma Physics Via Computer Simulation, Series in Plasma Physics, The Institute of Physics, 1991.

[74] D.Criswell and B. De, Intense localized pothoelectric charging in the lunar sunset terminator region 2. Supercharging at the progression of sunset, J. Geophysical Research, 82(7), 1005-1007, 1977

[75] O.Berg, H. Wolf, and J.Rhee, 'Lunar soil movement registered by the Apollo 17 cosmic dust experiment', in Interplanetary Dust and Zodiacal Light, H. Elsasser and H. Fechtig, Eds. New York: Springer-Verlag, 1976, pp.233-237.

[76] H. M. Mott-Smith, I. Langmuir, The theory of collectors in gaseous discharges, Physics Review, 28, 727, 1926

[77] I. Babuska and J. Melenk, The finite element method for elliptic equations with discontinuous coefficients, Computing, 5:207-213, 1970

[78] J. H. Bramble and J. T. King, A finite element method for interface problems in domains with smooth boundaries and interfaces. Advances in Computational Mathematics, 6:109-138, 1996.

[79] J. Wang, P. C. Liewer, S. R. Karmesin, D. Kondrashov, 3-D deformable grid electromagnetic particle-in-cell for parallel computers. In 35th AIAA Aerospace Sciences Meeting and Exhibit, AIAA 97-0365, Reno, Nevada, January 1997

[80] D. W. Hewett, The embedded curved boundary method for orthogonal simulation meshes, Journal of Computational Physics, 138: 585-616, 1997

[81] John Ambrosiano, Scott Brandon, Rainald Lohner, A finit element particle code on an unstructured grid, Conference record 1990 IEEE International Conference on Plasma Science p102, 1990

[82] John Ambrosiano, Scott Brandon, Rainald Lohner, Electromagnetic particle codes on unstructured grids, Lecture Notes in Physics, Springer Berlin, Vol. 395, p66-75, 1991

[83] Scott Brandon, David J. Larson, Niel Madsen, Dale E. Nielsen Jr., Patrick Weidhaas, 3-D electromagnetic Particle-in-Cell calculations using non-orthogonal unstructured grids, Conference record 1994 IEEE International Conference on Plasma Science p183, 1994

[84] C. S. Peskin, Numerical analysis of blood flow in the heart, Journal of Computational Physics, 25:220-252, 1976

[85] S. Osher, J. A. Sethian, Fronts propagating with curvature-dependent speed: Algorithms based on Hamiltonian-jacobi formulations, Journal of Computational Physics, 79:12-49, 1988

[86] M. Sussman, P. Smereka, P. Osher, A level set approach for computing solutions to incompressible two-phase flow, Journal of Computational Physics, 114:146-159, 1994

[87] R. J. LeVeque and Z. Li, The immersed interface method for elliptic equations with discontinuous coefficients and singular sources, SIAM Journal on Numerical Analysis, 31: 1019-1044, 1994

[88] M. Lai, C. S. Peskin. An immersed boundary method with formal second order accuracy and redusced numerical viscosity, Journal of Computational Physics, 160: 705-719, 2000

[89] G. Lapenta, F. Iinoya, J. U. Brackbill, Particle-in-Cell Simulation of Glow Discharges in Complex Geometries, IEEE Transactions on Plasma Science, Vol. 23, No. 4, 1995

[90] C. S. Peskin, D. M. McQueen, A three-dimensional computational method for blood flow in the heart. I. Immersed elastic fibers in a viscous, incompressible fluid, J. Computational Physics, Vol. 81, pp 372-405, 1989

[91] Xiaoming He, Tao Lin and Yanping Lin. Immersed finite element methods for elliptic interface problems with non-homogeneous jump conditions, Int. J. Numer. Anal. Model., 2009

[92] M. E. Markes, P. F. Williams, The effect of plasma shielding on dust particle interaction in low pressure plasmas, Physics of Plasmas, Vol. 10, No. 4, pp 1152-1158, 2003

[93] N. Sakumar, N. Mo¨es, B. Moran, and T. Belytschko. Extended finite element method for three-dimensional crack modelling. International Journal for Numerical Methods in Engineering, 48:1549–1570, 2000.

[94] J. Wang, D. Kondrashov, P. C. Liewer, S. R. Karmesin, Three-dimensional deformable-grid electromagnetic particle-in-cell for parallel computers, J. Plasma Physics, Vol. 61, part 3, pp 367-389, 1999

[95] J. Wang, Y. Cao, R. Kafafy, J. Pierru, V. K. Decyk, Simulations of Ion Thruster

Plume-Spacecraft Interactions on Parallel Supercomputer, IEEE Transactions on Plasma Science, Vol. 34, No. 5, October 2006